

UC Berkeley

UC Berkeley Electronic Theses and Dissertations

Title

High-Resolution μ ECoG: Design, Fabrication, and Applications

Permalink

<https://escholarship.org/uc/item/9qn1t2b6>

Author

Ledochowitsch, Peter

Publication Date

2013

Peer reviewed|Thesis/dissertation

High-Resolution μ ECoG: Design, Fabrication, and Applications

by

Peter Ledochowitsch

A dissertation submitted in partial satisfaction of the
requirements for the degree of
Joint Doctor of Philosophy
with the University of California San Francisco

in

Bioengineering

in the

Graduate Division

of the

University of California, Berkeley

Committee in charge:

Associate Professor Michel M. Maharbiz, Chair
Associate Professor Jose M. Carmena, Co-chair
Professor Robert T. Knight
Professor Christoph E. Schreiner

Fall 2013

High-Resolution μ ECoG: Design, Fabrication, and Applications

Copyright 2013
by
Peter Ledochowitsch

Abstract

High-Resolution μ ECoG: Design, Fabrication, and Applications

by

Peter Ledochowitsch

Joint Doctor of Philosophy

with the University of California San Francisco in Bioengineering

University of California, Berkeley

Associate Professor Michel M. Maharbiz, Chair

Associate Professor Jose M. Carmena, Co-chair

Since the early 1950s, electrocorticography (ECoG), the measurement of electrical potentials on the surface of the brain has become an invaluable tool in neurosurgery for the localization of epileptic foci before resection. The ECoG electrodes used in clinical practice are made in an archaic serial process that involves hand-soldering wires to a stiff, coarse grid of electrodes with a spatial resolution >1 cm, and a tangle of transcranial wires. In this thesis we report a modern microfabrication process based on photolithographic patterning of conductor thin films and of Parylene C, a biocompatible, transparent polymer. We used that process to make very thin and flexible ECoG arrays with electrode densities exceeding those of their clinical counterparts by more than two orders of magnitude, and addressed interconnect and noise performance issues. We constructed devices with multiple interconnected conductor layers, and used transparent conductors for integration of ECoG with optical neural stimulation techniques. Moreover, we developed a microscale ECoG with integrated loop antenna for a fully implantable, wireless system.

To show that such high-resolution devices have practical utility, we conducted acute and chronic *in vivo* studies in rats. We found that sufficiently small ECoG electrodes were able to register superficial multi-unit activity. We computed high-resolution tonotopic maps of the auditory cortex in anesthetized rats, and demonstrated that functional mapping using signal power in the 70 Hz - 170 Hz band (high- γ) is consistent with but much quicker and often more robust than functional mapping using action potentials recorded intracortically with penetrating electrodes. Finally we demonstrated that μ ECoG can serve as a less invasive alternative to penetrating electrodes in a brain-machine interface (BMI) paradigm by training awake behaving rats, chronically implanted with μ ECoG, to perform a 1D center-out task with auditory feedback by differentially modulating the high- γ signal on electrodes separated by as little as 200 μ m.

To $C_{12}H_{22}O_{11} - \pi$
to those who shared their wisdom
and to those who missed my absence

Contents

Contents	ii
List of Figures	iv
List of Tables	xiv
I Introduction	1
1 Electrocorticography: Origins and Progress	2
1.1 Introduction	2
1.2 The ideal neural interface	3
1.3 The neural basis of ECoG	4
1.4 Spectral features of the ECoG signal	7
1.5 Technological advances in ECoG	7
1.6 Applications of ECoG	13
II Engineering	18
2 The Parylene C micro-flex process	19
2.1 Choice of materials	19
2.2 Wafer-level fabrication	21
3 Designs	27
3.1 256 channel μ ECoG with 500 μ m pitch	27
3.2 Design of PCB adapters	33
3.3 Design for simultaneous μ ECoG and Blackrock ‘Utah’ Array recordings	34
3.4 μ ECoGs for acute auditory neuroscience	34
3.5 μ ECoGs for chronic implantation	34
3.6 μ ECoGs with monolithically integrated antenna for wireless power delivery and communication	35
3.7 Optically transparent μ ECoG design	39

3.8	μ ECoG design for optical window in Macaque	40
3.9	Ultraflexible ‘Nanoflex’ cables for ultra small ‘nanoprobes’	40
4	Assembly and packaging	50
4.1	Anisotropic Conductive Film Bonding	50
4.2	Low temperature solder thermocompression (LTST) bonding	51
4.3	Silver epoxy thermocompression (SET) bonding	52
4.4	Conductive sticky polymer thermocompression (CSPT)	53
4.5	Juxtaposition of bonding methods	55
5	Post-fabrication modifications	58
5.1	High-temperature annealing of Parylene C devices in inert atmosphere boosts life-time	58
5.2	Platinum black lowers electrode impedance	59
6	A Transparent μECoG Array	65
6.1	Introduction	65
6.2	Results	68
6.3	Conclusion	71
III μECoG Applications in Neuroscience		72
7	Functional mapping of auditory cortex	73
7.1	Introduction	73
7.2	Methods	75
7.3	Results	78
7.4	Conclusion	90
8	μECoG BMI in rat	91
8.1	Introduction	91
8.2	Chronic impedance monitoring	92
8.3	Brain control of auditory cursor	94
8.4	Conclusion	99
9	Conclusions and future work	100
9.1	The limitations of the Parylene process	100
9.2	Interconnect limitations	102
9.3	A tool for fast, nondestructive functional mapping	102
9.4	μ ECoG - the future of BMI?	103
9.5	Intracellular recordings with extracellular electrodes <i>in vivo</i> ?	105
Bibliography		106

List of Figures

1.1	Rough anatomical cross section of the head and corresponding electrophysiological recording modalities. Reproduced with permission from Schalk and Leuthardt [147], ©IEEE 2011.	4
1.2	SEM of microwire ECoGs. (A) Scanning electron microscopy of PMT microelectrodes. The 40- μm wires are embedded in silastic pillars. Top: typical appearance showing exposed metal wire tip. Impedances (magnitude at 20 Hz) ranged from 200 k Ω to 5 M Ω . Text shows measured impedance for indicated electrode. Middle: the highest impedances occurred when insulation covered the wire tip, minimizing surface area. Bottom: electrodes with torn insulation had more exposed surface area and much smaller impedance. The electrodes are also not centered in the silastic pillar. (B) SEM of Ad-tech microelectrodes. Left: typical appearance of 40- μm wire extruding from the silastic backing. Middle: very short wire unlikely to contact tissue. Right: example of irregular, fractured edge. (C) Sharp and irregular edges were present from both manufacturers (Left/middle: PMT. Right: Ad-tech). Figure and caption reproduced from [161] with permission of Wiley Periodicals, Inc. ©2013 International League Against Epilepsy.	9
1.3	The ‘closed-loop’ BMI concept. Neural signals, recorded with any available modality, are processed by a decoder that maps them onto the behavior of an actuator such as a motor or communication prosthesis. The test subject receives sensory feedback about the actuator’s action, and the subjects brain undergoes plastic changes to learn using the decoder to achieve a goal. Reproduced with permission from [93], ©2000-2013 Ovid Technologies, Inc.	15
2.1	Chemical structure and common trade names of biocompatible polymers commonly found in flexible neural interfaces.	19
2.2	Pinholes in < 2 μm thin Parylene C layer observed with Olympus laser scanning microscope (LEXT). The hole marked in the profile is approximately 1.9 μm deep.	22

2.3	Cable Fabrication in cross-section. Parylene layers are indicated in orange, metal layers are yellow and the silicon carrier wafer is shown in blue. (1) Cleaning silicon carrier wafer (2) Parylene C deposition [5 μm] (3) Platinum-gold-platinum (10 nm Pt / 140 nm Au / 50 nm Pt) e-beam evaporation and lift-off (4) Parylene C deposition [5 μm] (5) Via etch in oxygen plasma (6) Platinum-gold-platinum (10 nm Pt / 140 nm Au / 50 nm Pt) e-beam evaporation and lift-off (7) Parylene C deposition [5 μm] (8) Via etch in oxygen plasma (9) Via etch in oxygen plasma (10) Device release in mild detergent. This figure was modified from [90] with permission ©2013 IEEE.	26
3.1	CAD designs: (1) Three-layer devices (Parylene/metal/Parylene), (2) five-layer device (Parylene/metal/Parylene/metal/Parylene), (3) fan-out PCB layout.	28
3.2	Full system concept: the 256-electrode grid (CAD design) is monolithically integrated with the Parylene cable on wafer level. The Parylene cable fans out into an array of pads, which are ACF-bonded to a PCB outfitted with Omnetics connectors compatible with commercial headstages and amplifiers. Figure and caption were partially modified from [87] with permission; ©IEEE 2011.	29
3.3	Annotated post-fabrication photographs show the released flexible electrode array with Parylene cable ACF-bonded onto the fan-out PCB. Micrographs show the transition region between Parylene cable and ACF bonding pads (bottom left) and a close-up of the electrode pads including plasma-etched vias (top right). Observing the micro-cracks in the ACF bond pads led us to switch from using a single thick Pt layer to a Pt/Au/Pt tri-stack. Figure and caption were partially modified from [87] with permission; ©IEEE 2011.	30
3.4	Characterization of electrode/electrolyte interface by electrochemical impedance spectroscopy: We have characterized the electrode/electrolyte interface by electrochemical impedance spectroscopy (EIS) between 0.1 Hz and 10 kHz using artificial cerebrospinal fluid (aCSF) as electrolyte. (1) Nonlinear fit of Nyquist plot, insert shows equivalent circuit of the modified Randles Cell. (2) Nonlinear fit of the impedance modulus $ Z (f)$, insert shows impedance of a constant phase element (CPE) and total impedance of the modified Randles Cell. (3) Nonlinear fit of the phase $\theta(f)$, insert shows model parameters obtained by non-linear fitting of the EIS data to the modified Randles Cell model using EIS Analyser [16]. Figure and caption were partially modified from [87] with permission; ©IEEE 2011.	31

- 3.5 First *in vivo* experiment: Under anesthesia, a craniotomy was performed on a rat (female, Sprague-Dawley) and the ECoG array was placed subdurally on the primary auditory cortex (A1). (a) Grid placed on primary auditory cortex (A1): Acoustic evoked potentials were observed approx. 30 ms after stimulus onset, at attenuations below 50 dB (c). Note that the legend displays the *attenuation* level in dB. Lower attenuation levels correspond to higher sound pressure levels, which result in larger potential amplitudes and shorter response times. (b) Grid placed off A1 as control: Away from the auditory cortex, no acoustic evoked potentials could be recorded under identical stimulation conditions (d). Figure and caption were partially modified from [87] with permission; ©IEEE 2011. 32
- 3.6 Highly miniaturized 4-layer adapter PCBs: The 64-channel (left) and 96-channel (right) adapter boards are practical for acute and even for chronic implantation in small rodents such as mice and rats. The PCBs feature 3 mil trace-space and 6-mil laser-etched vias. All dimensions are given in mm. We purchased these custom boards with an immersion-gold finish from Beta Layout, Ltd. (<http://www.beta-layout.com>). 33
- 3.7 CAD design of μ ECoG for integration with 96-channel Blackrock ('Utah') Array introduced through plasma-etched perforations between the μ ECoG electrodes. 35
- 3.8 96-channel (left) and 64-channel (right) μ ECoGs with 7 mm cables and positioning flaps for acute *in vivo* studies. Etched perforations between electrodes allow for simultaneous μ ECoG and laminar probe recordings. The electrodes are 40 μ m in diameter; electrode pitch is 200 μ m. 36
- 3.9 96-channel (left) and 64-channel (right) μ ECoGs with 3 mm cables and a mini-mized implantable area (no positioning flaps) to enable minimally invasive craniectomies for chronic implantation and BMI studies. The electrodes are 40 μ m in diameter; electrode pitch is 200 μ m. 37
- 3.10 Wireless μ ECoG with integrated physical common-average reference and square loop antenna (6.5 mm \times 6.5 mm total). The array features 64 electrodes with a pitch of 400 μ m and an electrode diameter of 230 μ m. 38
- 3.11 Testing of the wireless μ ECoG system *in vivo*. (a) Overview (b) Close-up of μ ECoG array with monolithically integrated antenna on rat cortex (c) μ ECoG array with monolithically integrated antenna ACF-bonded to a controlled-impedance adapter board. The ACF-bond is protected with UV-cured epoxy. 39
- 3.12 Transparent μ ECoG: CAD designs (top) and finished devices (bottom) bonded to adapter boards compatible with TDT's ZC64 headstage. The two 7 \times 7 Parylene devices shown have the same arrays geometry as the as the metallic array shown in the upper photograph (CAD design shown in Fig. 3.7) but the ITO array at the bottom of the figure is nearly invisible due to its transparency. This caption and figure has been reproduced from [89] with permission; ©IEEE 2011. 41

3.13	μ ECoG below a silicone cranial window in NPH. Left: CAD design of the 2×96 -channel electrode array (pitch $700 \mu\text{m}$ over S1 and M1, and 1.4 mm in the periphery; $40 \mu\text{m}$ electrode diameter). The large ($400 \mu\text{m} \times 600 \mu\text{m}$) perforations allow viral injections and intracortical insertion of an optical fiber for optogenetic stimulation. Image credit: The two photographs on the right were taken and labeled in part by Dr. T. Hanson and Dr. A. Yazdan, ©Sabes lab, UCSF, 2013.	42
3.14	Cable layout for 32-channel cable (bottom metal layer shown in blue, top metal layer in grey, hatched regions indicate access and cut-out vias). This figure and caption have been modified from [90] with permission; ©IEEE 2013.	45
3.15	Cable layout for 64-channel cable (bottom metal layer shown in blue, top metal layer in grey, hatched regions indicate metal-access and cut-out vias). This figure and caption have been modified from [90] with permission; ©IEEE 2013.	45
3.16	Nanoflex cables: (a) 7 mm long 32 channel Nanoflex cable. (b) Magnified view of the probe bond pad array. (c) Magnified view of high-density traces. This figure and caption have been modified from [90] with permission; ©IEEE 2013.	46
3.17	DBS probe assembly: (a) 64 channel cable introduced into an ultrathin-wall ($250 \mu\text{m}$) semi-rigid PTFE cannula adjacent to a 64 channel silicon nanoprobe. (b) the cannula cable ACF-bonded to the 64 channel nanoprobe. This figure and caption have been modified from [90] with permission; ©IEEE 2013.	47
3.18	Electrochemical impedance spectrum measured across the interface of several cable electrodes (unbonded probe array) immersed in artificial cerebrospinal fluid aCSF. The electrodes show consistently low impedance ($<1\text{M}\Omega$) at 1kHz and are hence suitable for use as μ ECoG probes.	48
3.19	A 64 channel Nanoflex cable with integrated nanoprobe (left) alongside a commercially available 64 channel flexible cable with multi-shank silicon probe [1]. This figure and caption have been modified from [90] with permission; ©IEEE 2013.	49
4.1	Anisotropic conductive film bonding: (a) Top: ACF film is thermo-compressed between complementary pad arrays. Bottom left: Gold-coated polymer microspheres establish a robust electrical connection. Between adjacent pads the micro particles remain surrounded by insulating thermoplastic resin that prevents shorts. Bottom right: ACF resin provides mechanical stability under flexion. (b) 32 channel cable ACF-bonded to adaptor PCB. This caption and figure have been modified from [89] with permission; ©IEEE 2011.	51
4.2	Low temperature solder thermocompression bonding: (a) 32 channel nanoflex cable bonded to an adaptor PCB. (b) Aligning the other end of the cable to a nanoprobe prior to bonding: solder bumps are visible on the nanoprobe bond pad array (arrows).	52
4.3	Silver epoxy thermocompression bonding: contact transfer was used to pattern epoxy on the pads of a 32 channel adapter PCB.	53
4.4	Chemical structure and IUPAC names of PEDOT, PSS and D-Sorbitol [127].	55

4.5	PEDOT:PSS:D-Sorbitol printed on bond pad arrays. Top: 20 layers printed sequentially onto PCB, close-up of red box and optical profilometry results shown on the right. Bottom: 3 layers printed sequentially onto nanoprobe bond pad array, close-up of red box is displayed on the right. The 3D images were taken using an Olympus LEXT laser confocal microscope.	56
4.6	64-channel Nanoprobe CSPT-bonded to Parylene C cable.	57
5.1	Accelerated lifetime testing at 85°C in DPBS. Individual lead impedances at 1 kHz are shown as a function of soak time for two cables (without nanoprobes). (a) Non-annealed cable: representative impedance time course for four channels, which fail catastrophically after 12-60 hours (MTTF = 43 h). (b) Annealed cable: the impedances decreased slightly over time, however no failures occurred within the one-week soak period. This figure and caption have been reproduced from [90] with permission; ©IEEE 2013.	60
5.2	Randles Cell [138] equivalent circuit of the electrode-electrolyte interface.	61
5.3	Screen shot from the fitting interface of EIS Analyser [16]. Left: nonlinear fit of electrochemical impedance spectrum (EIS) before electroplating of platinum black. Right: nonlinear fit of EIS after plating. The yellow box highlights the change in fitting parameters, which are responsible for the 2-3 orders of magnitude decrease in impedance.	63
5.4	Expected noise spectral density and integrated noise power over the bandwidth of interest for ECoG for electrodes before and after surface-modification with platinum black.	63
5.5	Left: Optical micrograph of 64-channel, high-density μ ECoG: The device featured 200 μ m electrode pitch, 40 μ m electrode diameter and 10 μ m minimum feature size (trace/space). Some of the displayed electrodes (gray) consisted of smooth and highly reflective, evaporated platinum. The black electrodes were electrochemically plated with platinum black, a porous form of platinum that increased the effective electrochemically available area and decreases electrode impedance. Perforations in the Parylene, increase the arrays mechanical compliance and allow vascularization through the array [148]. Right: Impedances of plated vs. non-plated electrodes: The dark gray bars show the real part of the impedance for 14 evaporated platinum electrodes. The light gray bars show impedances of the same electrodes after every odd-numbered electrode was direct current (DC) plated with platinum black for 45 s at a current of -0.5 μ A. Note the logarithmic resistance scale: platinum black deposition reduced the electrode impedance by more than two orders of magnitude. This figure and caption have been modified from [88] with permission; ©IEEE 2013.	64

6.1	Integration of μ ECoG with optogenetics. Patterned light, e.g. from a Digital Micromirror Device (DMD), excites transfected or transgenic neural tissue underneath a transparent μ ECoG array. Electrical activity detected by the μ ECoG could be feedback-coupled with the light-source output to control activation states on the cerebral cortex. This figure and caption have been modified from [89] with permission; ©IEEE 2011.	66
6.2	Micrographs and SEM images of the 16-channel and 49-channel devices. (a) Bond pad damage on ITO-only devices. (b) Intact electrodes of a 16-channel ITO device. (c) Electrodes and interconnects of a 49-channel Au-ITO hybrid device. (d) 16-channel hybrid array. The ring-shaped electrodes are made of ITO. The light-yellow lines indicate the overlap of Au and ITO. The lower portion of the connections (orange) consists of Cr/Au. This figure and caption have been reproduced from [89] with permission; ©IEEE 2011.	67
6.3	Transmittance of the 110 nm thin ITO film is shown as a function of wavelength (285 nm to 830 nm). This figure and caption have been modified from [89] with permission; ©IEEE 2011.	68
6.4	ITO and gold electrodes illuminated using a laser scanning microscope. While the gold electrode shows pronounced photoelectric spikes, no such artifact can be seen on the ITO electrodes.	69
6.5	Characterization of the electrode-electrolyte interface by electrochemical impedance spectroscopy. The data were adequately fit by the Randles Cell circuit model, see Fig. 5.2. This figure and caption have been modified from [89] with permission; ©IEEE 2011.	70
6.6	Left: Control for photoelectric artifact: at 150 Hz the channelrhodopsin-2 cannot follow and no high frequency response is observed. Right: at 50 Hz the channelrhodopsin-2 follows the laser pulse train and a high frequency neural response is observed in μ ECoG.	71

- 7.1 Tonotopic organization of multiple fields within the rat auditory cortex. A: an 8×7 -mm grid is superimposed onto a lateral view of the right hemisphere of the rat brain. Numeric values denote distance with respect to bregma (0, 0). Five black ellipses are superimposed onto the temporal cortex to represent the typical position and shape of the 5 cortical auditory fields described in this figure. B: location of 276 separate microelectrode penetrations (orange dots) are shown in reference to the surface vasculature of the right temporal cortex. Yellow arrowhead identifies the rhinal vein. White arrowhead identifies the middle cerebral artery. P and V indicate posterior and ventral, respectively. Scale bar = 1 mm. C: tessellated Voronoi map is constructed such that the polygon color represents the characteristic frequency (CF) associated with neurons located in the middle cortical layers at that position in the map and the polygon area is proportional to the distance separating neighboring penetrations. Filled circles indicate unresponsive sites. Open circles represent sites with sound-driven responses for which a CF could not be defined. D: schematic drawing of the relative position of 5 tonotopically organized auditory cortical fields. Borders between fields were defined by reversals or shifts in the CF gradients. PAF, posterior auditory field; AI, primary auditory cortex; VAF, ventral auditory field; SRAF, suprarhinal auditory field; AAF, anterior auditory field. Figure and caption reproduced with permission from [135], ©2007 the American Physiological Society. 74
- 7.2 Left: micrograph of 64-channel μ ECoG with 32-channel laminar probe (NeuroNexus A1x32-Poly3-10mm-50-177) inserted through one of the etched perforations. Right: layout of the A1x32-Poly3-10mm-50-177 laminar probe. Image credit: NeuroNexus Technologies, Inc. 76
- 7.3 Representative photograph of the surgical setup. A 64-channel Parylene C μ ECoG array (200 μ m electrode pitch, 40 μ m electrode diameter) was placed over auditory cortex and a 32 channel NeuroNexus laminar probe (A1x32-Poly3-10mm-50-177) was inserted into one of the perforations in the μ ECoG array to a depth of approximately 600 μ m using a micromanipulator. Image credit: Kris Bouchard. 77
- 7.4 Evoked response to white noise bursts (average of 60 bursts, 100 ms in length, 900 ms inter-stimulus-interval). Top: White noise burst, Middle: Overlay of 60 time-domain auditory evoked potentials (AEPs), Bottom: Average of 60 frequency-domain AEPs. Note that most of the evoked power lies between the first maximum and the subsequent minimum of the time-domain AEP. 79
- 7.5 Overlay of spectra evoked by auditory stimulation with white noise bursts on 64 channels. Each spectrum is an average response across 60 WN bursts. The black trace corresponds to the mean spectrum bounded by the standard error of that mean (grey region). The predominant measure of neural response in this chapter is the high- γ power averaged between 70 Hz and 170 Hz, which captures the maximum of the mean spectrum. The local maximum between 400 Hz and 600 Hz is also worth noting as it appears quite prominently on some electrodes. 80

7.6	Most of the 64 electrodes show a considerable increase in multi-unit firing rate in response to white noise stimulation (mean plotted in response to 60 WN bursts). Time is shown on the x-axis and firing rate on the y-axis. Stimulus (WN burst) onset is indicated by the first grey line, stimulus end is indicated by the second grey line. The number next to each subplot indicates the trial-averaged peak MUFR. Note that the firing rates detected on adjacent electrodes can be substantially different, which indicated that the electrodes, even though they are spaced by $< 200 \mu\text{m}$, carry independent information.	82
7.7	Overlay of 100 peak-aligned multi-unit waveforms as recorded on a representative μECoG electrode (blue). The red trace shows an average spike-triggered waveform of the 100 traces.	83
7.8	Top two rows: WN-evoked spectrograms on a group of 8 adjacent electrodes; bottom two rows: WN-evoked increase in firing rate on the same group of 8 spatially contiguous electrodes. There is no obvious relationship between the presence or absence of evoked G, HG, or UHG power and the presence (2 bottom rows: 4 plots on the left) or absence of firing rate modulation (2 bottom rows: 4 plots on the right).	84
7.9	Two-dimensional pure tone stimulus set. Each frequency-amplitude pair was repeated 20 times. The tone duration was 50 ms and the inter-stimulus interval (ISI) was 250 ms. Image credit: Kris Bouchard, Chang Lab, UCSF.	85
7.10	Fine-grained electrocorticographic mapping of auditory receptive fields. Tuning curve shape and characteristic frequency vary significantly even over distances as small as $200 \mu\text{m}$. The characteristic frequency is approximately conserved across stimulus amplitudes, color-coded from black (-70 dB) to red (0 dB).	85
7.11	Using high-gamma (HG) power as a metric for neural activity yields the highest number of tuned electrodes and the most robust tuning curves, as compared with using gamma (G) power, ultra-high gamma power (UHG) or multi-unit firing rate (MUFR).	86
7.12	Comparison of μECoG -derived tuning curves (tuning curves on 16 plots in the xy plane are shown) with laminar-probe-derived tuning curves (gray boxes: only tuned channels of laminar probe are shown). The tuning curves derived from surface measurements of HG power are very similar to the tuning curves derived from intracortical spike firing measurements taken in the same xy-vicinity, albeit the intracortical tuning is a little sharper. As expected, the characteristic frequency remains roughly constant along the z-axis of the intracortical laminar probe introduced perpendicularly to the cortical surface.	87

7.13	Saturation of the average's predictive power occurs for a lower number of trials when the HG-portion of the μ ECoG LFP is used to compute the tuning curves Fig. 7.13 (right) as compared to MU signal recorded with penetrating electrodes Fig. 7.13 (left). Note that the coefficient of determination for the same number of averaged trials is much lower for firing rate tuning than it is for HG power tuning. This indicates that when compared point-wise, firing-rate derived tuning curves in single-trial are much noisier than HG-power derived tuning curves in single-trial.	88
7.14	Stitched tonotopic map generated by moving the array to four different auditory areas (A1, VAF, SRAF, AAF) computed from data that was acquired in less than 2 hours total (30 minutes per location). This map is quite reminiscent of the one painstakingly compiled by Polley et al.in [135] (see Fig. 7.1 for comparison). Image credit: Kris Bouchard, Chang Lab, UCSF.	89
8.1	Time course of impedance magnitude and phase, post-implantation, averaged over the 64- μ ECoG electrodes. The error bars reflect the standard error of the mean. Most electrode impedance magnitudes were in the range acceptable for acquisition of surface local field potentials ($< 1M\Omega$ at 1 kHz). This caption and figure have been modified from [88] with permission; ©IEEE 2013.	92
8.2	Experimental paradigm: an awake behaving rat modulates high γ power on two selected electrodes. The difference of the negative logarithm of the gamma power between the two electrodes is mapped onto the pitch of an auditory cursor (a tone that the rat can hear as a form of auditory feedback about the position of the cursor, updated every 200 ms). When the cursor reaches a target tone, the animal obtains a food or a sugar water reward. Modified from Fig. 1 of [80], reprinted by permission from Macmillan Publishers Ltd: Nature [80], ©2012.	95
8.3	Experimental setup in the Carmena lab at UC Berkeley: The awake behaving rat is connected to the Plexxon system via a TDT ZC64 headstage, a series of adapters, a commutator and two pre-amplifiers.	96
8.4	Example of a successful BMI session. Left: Target accuracy starts close to the baseline (chance level) and increases in the first 30 minutes of the session until saturation is reached. Right: The reach time (time-to-target) steadily decreases over the course of the session.) The output electrode separation in this particular session was $200\mu\text{m}$	97
8.5	Average of target accuracy above baseline across all animals and sessions as a function of time in each session. The error bar envelope indicates the standard deviation (sample error) across animals and sessions. On average, accuracy increases to saturation in the first 30 minutes of a session.	98

- 8.6 Target accuracy above chance as a function of distance between the output electrodes: The animals are able to learn controlling to control the auditory cursor even if the output electrodes were adjacent, (i.e. as close to each other as $200 \mu\text{m}$ center-to-center.). However, no statistically significant dependence of the cumulative target accuracy on the electrode separation was observed. The error bars indicate the standard error of the mean across animals and sessions. 99

List of Tables

1.1	Comparison of signals acquired using different neural interfaces. The spatial resolution estimates were derived from Fig. 2 of [153].	3
2.1	Parylene deposition parameters.	22
3.1	Comparison of bulk material properties between Neuronexus and Nanoflex cables. This table has been modified from [90] with permission; ©IEEE 2013.	44
3.2	Comparison of calculated mechanical properties between Neuronexus and Nanoflex cables. This table has been modified from [90] with permission; ©IEEE 2013.	44
5.1	Accelerated lifetime test parameters for non-annealed and annealed cables. This table has been reproduced from [90] with permission; ©IEEE 2013.	60

Acknowledgments

First and foremost, I would like to thank my thesis adviser, Michel M. Maharbiz, who has created a supportive and fun work environment, and never failed to provide me with anything that would further my career, be it funding for research and travel, advice, or letters or recommendation. I always wanted a PhD-adviser I could look up to not only for his academic achievements but also on a human level. I have found such a person in you, Michel. I am also very grateful to my co-adviser, Jose Carmena, who invited me into his lab with open arms and provided much-needed advice. Thank you Bob Knight, it was a privilege to have you, the Berkeley “Godfather of ECoG” in my corner of the ring. Thank you, Christoph Schreiner, for bringing μ ECoG to my attention when I was still a greenhorn graduate student. Thank you, Tim Blanche: I have enjoyed your creativity in our collaborative projects over the years. Thank you Viviana Gradinaru, and Flip Sabes for giving me the opportunity to dabble at the intersection between ECoG and optogenetics. Eddie Chang: thank you for allowing Kris and myself to pursue the auditory μ ECoG work.

For better or worse, I had so many collaborators during my time in Berkeley, that I am bound to miss saying “Thanks” to a few of you, for that I apologize. However, some of you deserve special recognition, for this thesis would not have been possible but for your selfless dedication, advice, help, and support. Thank you Aaron for being so generous with your time and for helping me with all of the chronic implant surgeries! Thank you, Kris & Tom, for not only believing in but being so hugely enthusiastic about the potential of μ ECoG in animal neuroscience, that you placed my devices on innumerable rat cortices. Thank you Rikky & Jan for our fruitful collaboration to cut the wires from μ ECoG that ultimately culminated in the birth of Cortera Neurotechnologies, Inc. Thank you Robert and Asako for helping me to perform my very first *in vivo* experiment that made it into my first paper at Berkeley. I would like to thank all Masters & rotation students that assisted me, and gave me plenty of opportunity to practice and improve my project management and mentorship skills. In particular, I would like to emphasize awesome work done by Romain, Eliza, Raphael, and Camilo. Furthermore, my work would not have been possible without the dedicated staff of the Berkeley Microlab (Marvell Nanolab these days), CITRIS, and Nathan, Ming, and Salah from Nanoshift (who ensured that I could focus part of my time on *in vivo* testing, rather than on fabrication, in the last stage of my PhD), BSAC (whose member fees paid for much of my cleanroom time), CNEP, MuSyC, and the Berkeley-UCSF Graduate Group in Bioengineering. If you and I co-authored on a paper: thank you! If you helped me with advice, supplies or equipment, thank you! If you taught me in class at Berkeley, thank you!

I want to thank my family who stayed behind in the Old World and was understanding of my desire to pursue a career half-way across the world, and who I have missed dearly in the last 5+ years. Thanks to all of my friends at CSC, CHAOS and BHGC - I shared some amazing adventures with you and you made the downs of a graduate students life way more bearable - I will miss you! Last but not least, thank you Jill, for believing in me and supporting me through thick and thin.

Part I

Introduction

Chapter 1

Electrocorticography: Origins and Progress

1.1 Introduction

The question of how electrical activity in a group of neurons ultimately results in perception, consciousness, and personality has intrigued the neuroscience community since ancient times. In spite of an ever-accelerating research effort, many fundamental questions remain unanswered, and we still lack a cohesive theoretical framework in which clinically observable high-level processes can be interpreted mechanistically in terms of underlying neural activity. Developing a comprehensive theory of the brain remains one of the last great frontiers of human discovery; a base of knowledge that would not only enable new diagnostic and treatment tools for a variety of neurological and psychiatric diseases but also hold the potential to redefine our view of the human condition.

In the last ten years, this question has attracted unprecedented attention from both private (e.g. Paul Allen donating \$500M to the Allen Institute for Brain Science) as well as public sources (e.g. the EU spends \$1.3B on developing a computer simulation of the brain, the US multi-billion dollar Brain Activity Map (BAM) effort announced earlier this year).

The history of science brims with examples, which show that most great breakthroughs in understanding follow on the heels of advances in experimental techniques and instrumentation, a trend that is very pronounced in the history of neuroscience: the Golgi stain and electron microscopy taught us neuronal structure and sub-structure, microstimulation and optogenetics allowed us to functionally dissect neural circuits, and recently, electrocorticography has started to uncover how information is processed on the 'mesoscale' and how oscillations might mediate intra- and inter-areal communication on the cerebral cortex.

Table 1.1: Comparison of signals acquired using different neural interfaces. The spatial resolution estimates were derived from Fig. 2 of [153].

	EEG	ECoG	LFP	AP
Spatial resolution	3 cm	0.5 cm	1 mm	0.2 mm
Frequency contents	0.1 - 50 Hz	1 - 300 Hz	1 - 500 Hz	0.5 - 10 kHz
Invasiveness	None	Significant	High	High
Coverage	Whole Brain	Hemisphere	$\approx 10 \text{ mm}^2$	$\approx 10 \text{ mm}^2$
Signal stability	Unlimited	Decades	Years	Months
Signal amplitude	$< 10 \mu\text{V}$	$< 100 \mu\text{V}$	$< 1 \text{ mV}$	$< 1 \text{ mV}$
Signal type	continuous	continuous	continuous	discrete

1.2 The ideal neural interface

While there are several formidable obstacles to completing the BAM project, it is widely recognized that current methods for the observation of neural activity *in vivo* are not quite up to the task. Broadly speaking, desirable features for an ‘ideal’ neural interface are:

- **Stability:** the sources of the acquired neural signal should remain invariant with time.
- **Large area coverage:** ideally the activity of the entire brain should be observable.
- **Low power consumption:** power levels should be kept very low to avoid damaging neural tissue or biasing neural processes.
- **Continuous:** device should enable uninterrupted data acquisition during physiologically normal behavior, such as e.g. sleep.
- **Unobtrusive:** natural movement should not be encumbered.
- **Minimal invasiveness:** the device should not disturb or damage the neural structure and allow natural behavior of the subject.
- **High spatiotemporal resolution:** an ideal device resolves individual neuron firing events in both time and space.
- **Longevity:** the device life-time should exceed the life time of the implanted subject.

Achieving all of the above features simultaneously in a single device would be a very worthwhile but also ambitious undertaking. As implied in Table 1.1, there is typically a trade-off between feasibility to achieve high spatial resolution that requires intraparenchymal sensors to penetrate neural tissue, and the ability to record from a large area (or volume) of brain tissue.

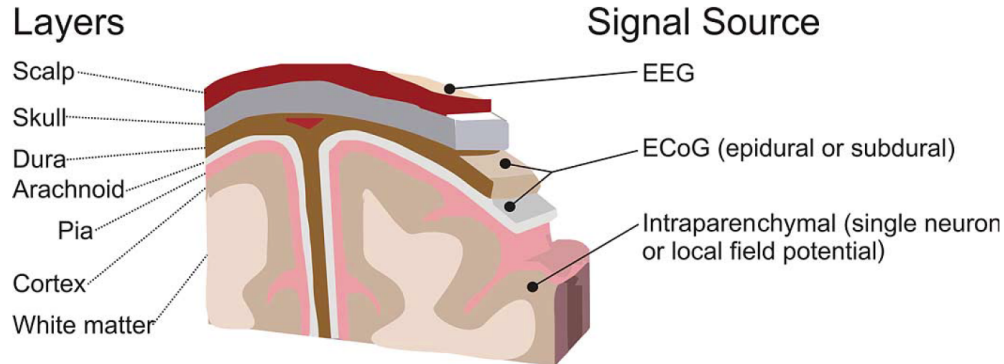


Figure 1.1: Rough anatomical cross section of the head and corresponding electrophysiological recording modalities. Reproduced with permission from Schalk and Leuthardt [147], ©IEEE 2011.

In Table 1.1, we compare state-of-the-art electrophysiological recording modalities and emphasize their characteristics in terms of lifetime, invasiveness and spatial resolution. Non-invasive techniques such as electroencephalography (EEG) can in principle be used to record signals chronically from most of the brain, and for prolonged periods of time. Unfortunately, they suffer from poor spatial resolution of the order of several cm. Penetrating electrodes made of micro-machined silicon [119] or Pt-Ir [116] microwires provide superior spatiotemporal resolution but only allow recording over an area of a few square mm². They can record both the action potential (AP) of individual neurons and the local field potential (LFP) but penetrating electrodes destroy neural tissue and cause scar tissue formation, which often limits the recording lifetime to a few months (a few years at best) making it impractical for translation to clinical use in humans.

ECoG holds the greatest potential as a clinically viable recording modality. While a craniotomy is still needed for implantation, the electrodes do not penetrate or scar the cortex. ECoG relies on surface electrodes and does not breach the blood-brain barrier. The sensors are implanted in the sub- or epidural space that is nearly devoid of an immune response. The resolution of current clinical ECoG grids used in human epileptic seizure focus localization prior to surgery is on the order of half a centimeter. Even given such limited spatial resolution of FDA-approved ECoG arrays, ECoG has recently seen a surge in popularity in the research community because it allows access to human, task-related electrophysiological recordings.

1.3 The neural basis of ECoG

The brain is an electric organ, which was known or at least conjectured for millennia: e.g. Galen, who lived between 129-199 A.D., suggested, as a treatment for headaches, placing an

electric Torpedo Fish on the patient's forehead [103] - essentially a form of transcutaneous electrical nerve stimulation [118].

Each ionic current in the brain (and there are many different cellular processes generating such currents) gives rise to a (scalar) field of electric potential. Due to the linearity of Maxwell's equations, all of these scalar fields sum linearly (superposition principle of electrodynamics) to give rise to a cumulative 'electric brain potential' field. The value of this field, for each point in space, can be measured as a voltage difference between that point and some arbitrarily chosen reference point. For purely historical reasons, this 'brain potential' has various names, depending on where and by what means we measure it. Measured with electrodes placed on the scalp, it is known as the electroencephalogram (EEG¹), if electrodes are placed into the intracranial space beneath the skull, we call it (subdural or epidural) electrocorticography (ECoG²). When we insert an electrode into the brain and measure the brain potential in the extracellular space, we call it the local field potential (LFP). While from the point of view of physics all of the above (see Fig. 1.1) are essentially the same phenomenon, the above measurement techniques emphasize the contribution of vastly different sources to the recorded signal.

Every current through an excitable membrane, be it part of the soma, axon, or dendrite contributes to the electric brain potential. Synaptic activity, more specifically excitatory Ca^{2+} and Na^{+} currents through N-methyl-D-aspartate (NMDA) and α -amino-3-hydroxy-5-methyl-4-isoxazolepropate (AMPA) receptors, is thought to be one of the biggest contributors to the extracellular fields because synaptic currents are relatively slow and thus likely to overlap in time and to add up constructively to macroscopically measurable signals [38]. It is important to keep in mind that in order to maintain electroneutrality, any membrane current must have a return current close-by (closed-field) or further away (open field). Large pyramidal neurons tend to have spatially extended dendritic arbors that may often give rise to spatially extended open field current dipoles. Fortunately for the electrophysiologist, in the cortex, the long and thick, apical dendrites of pyramidal neurons are aligned perpendicular to the cortical surface - a configuration predestined for constructive interference of synchronous current dipoles [22, 98]. By contrast, much faster axonal action potentials, which generate a large voltage 'spike' in close proximity to a soma or axon, are thought to contribute less to ECoG and EEG signals that are recorded at a greater distance from the source and are attenuated by the $\frac{1}{r^2}$ distance dependence of the (rather small, closed field) dipole potential, and by destructive spatiotemporal averaging [121]. It is well-worth noting, however, that in cases where a mesoscale population of neurons fires in synchrony, e.g. because the population firing is time-locked to the phase of some brain rhythm (θ , γ , etc.), the contribution of the action potential to the LFP can be substantial [185].

There are a number of important non-synaptic events that may give rise to significant LFP signals: Long-lasting high-amplitude dendritic Ca^{2+} spikes, e.g. triggered by back-

¹Invented in Germany in the late 1920s by Hans Berger who was initially motivated by a desire to prove that telepathy was a real, physical phenomenon; in part for this reason, his work has not been taken seriously until independent verification in 1934 [162].

²Developed in Montreal, Canada, in the early 1950s by Jasper & Penfield.

propagating action potentials, can reach amplitudes around 50 mV [99] but unfortunately the occurrence of such spikes *in vivo* is poorly understood. Another potential non-synaptic source of LFP are voltage-dependent resonant membrane oscillations [99], which have been found to lie in the γ range (30-90 Hz) for certain types of inhibitory interneurons [134], which also quite commonly synchronise their membrane oscillations.

Post-bursting afterhyperpolarizations (AHTs) can be comparable in amplitude to synaptic events and last just as long [24]. Especially if bursting is coordinated in time between nearby neurons, AHTs may measurably influence the LFP signal.

Last but not least, non-neural, glial sources may be responsible for very low frequency features (slower than 0.1 Hz) in recorded brain potentials [133].

Interspecies differences

On average, the LFP amplitude has been observed to follow the progression mouse>rat>cat>primate>human, i.e. it is anti-correlated with mammalian brain size. There are at least two conceivable explanations of this phenomenon:

- In animals with larger brains, neurons are distributed over a larger volume in a staggered fashion that leads to partial cancellation of somato-dendritic currents [21].
- Larger animals have larger pyramidal cells that are packed less densely [62], effectively resulting in a lower conductivity.

In epidural ECoG this progression is exacerbated due to the fact that the dura in animals with a larger cranium tends to be thicker than in animals with a smaller cranium. And when ECoG electrodes are placed subdurally: in animals with a smaller brain, layer 1 of cortex is thinner and pyramidal cells are closer to the surface electrodes [172].

Are extracellular brain potentials an epiphenomenon?

One big elephant in the room is the question of whether extracellular field potentials are just an epiphenomenon of intra-cellular information processing [39] or if the extracellular fields influence the transmembrane potential in a biologically significant way that mediates feedback or amplification through *ephaptic coupling*. While it is unclear if all features (especially low-amplitude, high-frequency features such as gamma) of the LFP cause physiologically relevant feedback on neurons, it has been shown that low-frequency, low voltage gradients can indeed influence neural activity and cognitive function [118].

Volume conduction may obscure true cortical current sources

Extracellular medium is anisotropically conductive and the exact path of current spread through the extracellular volume (i.e. volume conduction) depends on the value of the conductivity tensor, which is unknown in practice. This fact often masks the true location

of the current multi-poles that are the source of the extracellular fields [70, 98]. Volume conduction effects are most severe when the brain potential is measured far away from the source, as is the case in EEG and epidural ECoG in larger primates.

The motivated reader in search of more references on the origin of extracellular potentials is kindly advised to consult a most excellent review by Buzsáki, Anastassiou, and Koch [23].

1.4 Spectral features of the ECoG signal

The amplitude of local field potentials shows a power law behaviour of the form $\frac{1}{f^n}$, with $n \in [1, 2]$ where the amplitude drop-off as a function of frequency is commonly attributed to dendritic low-pass filtering [97]. In large neurons with extended dendritic arbors, such as pyramidal cells, this effect is particularly pronounced. Some of the low-pass filtering properties are also often attributed to capacitive effects in the extracellular medium, albeit existence and origin of non-ohmic effects in the extracellular lumen remain controversial [102, 121]. In recent years, increased attention has been paid to the contribution of network effects and phase-amplitude coupling to the $\frac{1}{f^n}$ law of LFP power scaling. As pointed out in Buzsáki's *Rhythms of the Brain* [22] one should take this overall statistics of the LFP with a grain of salt because the statistics of stimulus-evoked LFPs, which occur on time-scales relevant for sensory information processing is often dominated by oscillatory behavior and grossly deviates from a scale-free power-law.

1.5 Technological advances in ECoG

Brief history of electrocorticographic arrays: our work in context

In the early 1950s, two very innovative neurosurgeons at the Montreal Neurological Institute, Herbert Jasper and Wilder Penfield, realised that recording electrical potentials directly from the surface of cerebral cortex, bypassing the low-pass filtering volume conduction effects of the skull [121], allowed precise localization of seizure onset zones in epileptics. Their technique, which involved placing a small number of ball-shaped electrodes mounted on a frame (ball-grid array) onto the pia mater, was an essential part of what became known as the *Montreal procedure* [128]. In the 70s, Penfield's ball-grid arrays were replaced by flexible strips and arrays of platinum-iridium disk-electrodes (10 mm pitch, 2 mm electrode diameter, usually 16-64 electrodes per sheet) mounted on medical-grade silastic. Thin wires were hand-soldered to the electrodes and routed to a battery of connectors. This technology has been grandfathered into FDA-approval for acute studies (<30 days in duration) because its marketing predated, and it has not been "significantly changed", since May 28, 1976. Due to the fact that any modern technological innovation in ECoG would have to pass the barrier of regulatory approval, archaic silicone-platinum devices are to this day the only ECoG arrays approved for clinical use in human patients. The main commercial suppliers at the time of

writing (2013) are Ad-Tech Medical Instrument Corporation (www.adtechmedical.com) and PMT Corporation (www.pmtcorp.com). In the last decade, the idea that denser μ ECoG grids may be useful for more precise mapping of seizure onset zones, eloquent cortex, and clinical research gained increased traction among neurosurgeons [121, 174]. In response to the new demand, commercial manufacturers started offering custom ECoG electrodes, including grids made by embedding microwires into silastic pillars. Unfortunately, the ends of these wires were often cut irregularly, which not only caused recording site impedance to vary widely (see Fig 1.2) but risked scratching the cortex, breaking off pieces of wire inside the cortex, and causing hemorrhaging and seizures. These issues ultimately lead Ad-tech to recall all μ ECoG arrays manufactured in this fashion between 2006 and 2012³

The Williams lab at the University of Madison Wisconsin was among the first [77] to apply modern photolithographic microfabrication techniques to μ ECoG arrays and remains to this date one of the more technologically innovative μ ECoG engineering labs [76, 148, 164]. Rubehn et al. in Prof. Thomas Stieglitz' lab at IMTEK (Freiburg, Germany) followed suit by microfabricating the first large-channel count (252 electrodes, 1 mm electrode diameter, 2 mm electrodes pitch) polyimide-based μ ECoG [143] specifically developed for use in non-human primates (NHP) [17]. In this work, connecting the wafer-level device to commercial connectors was accomplished in a rather cumbersome, serial soldering process. The Stieglitz lab further streamlined the interconnect process in more recent work [41]. The Maharbiz lab at UC Berkeley entered the field in 2011 by reporting the densest high-channel count μ ECoG at the time (256 channels, 500 μ m electrode spacing, Parylene C was used throughout, doubling as both substrate and insulator) [87] quickly followed by the first *fully optically transparent* μ ECoG array that uses indium tin oxide, a transparent conductor that shows no photoelectric artifact when illuminated with visible light, and is compatible with optical recording and stimulation modalities [89]. That work has since been expanded on by the Li lab Michigan State University that is working on integrating LEDs directly above the transparent ITO electrodes [84]. A collaboration between the Rodgers lab at UIUC and the Litt Lab at the University of Pennsylvania, contributed two important innovations to μ ECoG hardware. First, the researchers realized that while arrays that optimally conform to the curvature of the brain need to be extremely thin and mesh-like to ensure mechanical compliance, such devices are very hard to handle and place during surgery. They developed a backing of water-soluble, biocompatible spider-silk to structurally support extremely thin and flexible μ ECoG arrays [75]. Moreover, Vivendi et al. addressed the problem of growing interconnect complexity associated with a larger number of recording channels by designing a 360 channel μ ECoG (500 μ m electrode pitch) with ultra-thin, silicon-based, active electronics for first-stage amplification and analog multiplexing, integrated into each electrode. With this device, the Litt lab was able to demonstrate in epileptic canines that ictal spikes, which seem very similar when averaged by larger electrodes, appear as different types of traveling waves (spiral or planar) in high-resolution μ ECoG, some of which only appear in epileptic

³See Class 1 recall notice: <http://www.fda.gov/medicaldevices/safety/listofrecalls/ucm342797.htm>, accessed on 11/21/2013.

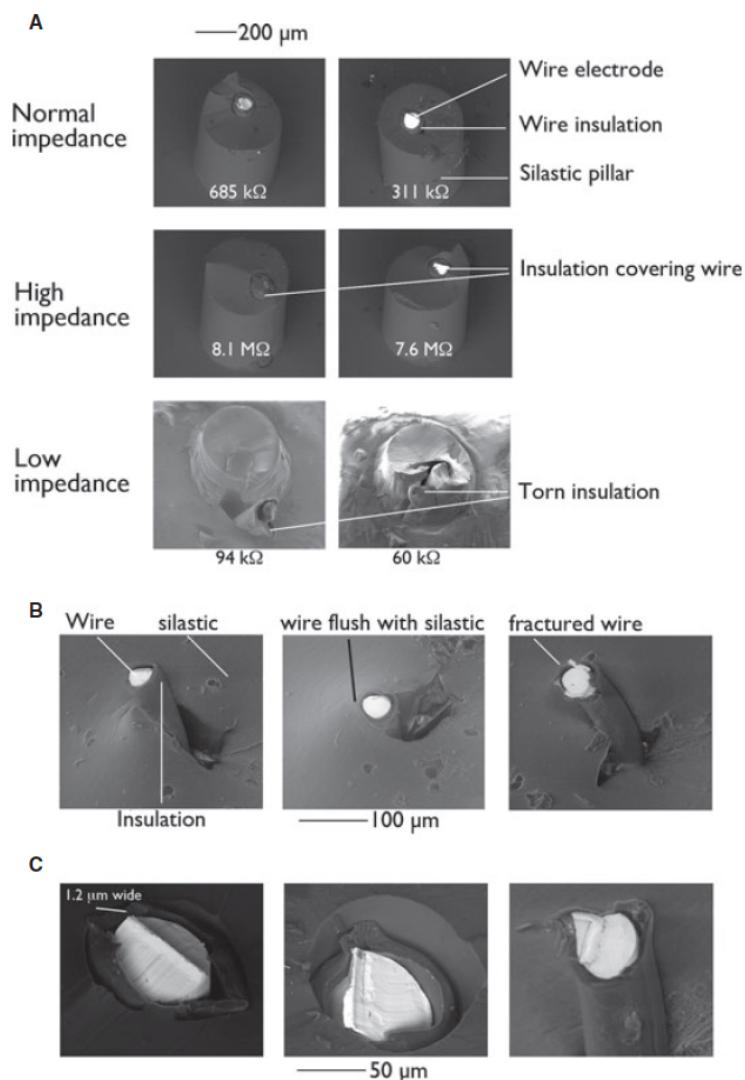


Figure 1.2: SEM of microwire ECoGs. (A) Scanning electron microscopy of PMT microelectrodes. The 40- μm wires are embedded in silastic pillars. Top: typical appearance showing exposed metal wire tip. Impedances (magnitude at 20 Hz) ranged from 200 $\text{k}\Omega$ to 5 $\text{M}\Omega$. Text shows measured impedance for indicated electrode. Middle: the highest impedances occurred when insulation covered the wire tip, minimizing surface area. Bottom: electrodes with torn insulation had more exposed surface area and much smaller impedance. The electrodes are also not centered in the silastic pillar. (B) SEM of Ad-tech microelectrodes. Left: typical appearance of 40- μm wire extruding from the silastic backing. Middle: very short wire unlikely to contact tissue. Right: example of irregular, fractured edge. (C) Sharp and irregular edges were present from both manufacturers (Left/middle: PMT. Right: Ad-tech). Figure and caption reproduced from [161] with permission of Wiley Periodicals, Inc. ©2013 International League Against Epilepsy.

but not in healthy brain. Unfortunately, Viventi’s active μ ECoG is difficult to fabricate with high yield and cannot be chronically implanted as it fails electrically (severe current leakage as a consequence of insulation break-down) within 12 hours⁴.

Khodagholy et al. at Ecole Nationale Supérieure des Mines fabricated one of the densest μ ECoGs published at the time of writing of this thesis (60 μ m electrode pitch), and treated his electrodes with a thin film of PEDOT:PSS, an ionically doped conductive polymer that decreases electrode impedance, lowers noise, and renders the electrode-electrolyte interface more Ohmic [72]. Khodagholy et al. also developed an array of PEDOT-based transistors [73] for electrocorticographic recordings. In order to operate the transistors near maximum transconductance, the entire brain needs to be biased at 300 mV, which may influence brain function, as even *transcranial* direct current stimulation (tDCS) has been shown to influence brain function significantly [118]. Khodagholy argues that one of the principal advantages of measuring current flowing between source and drain of the PEDOT transistor, modulated by the brain potential acting on the gate, rather than the brain potential directly, lies in an improved signal-to-noise ratio of 22.3 dB.

Last but not least, solving the interconnect complexity challenge and reducing potential for failure of wires by developing a wireless electrocorticographic systems has recently started to receive increased attention [29, 40, 57, 111, 165]. In a collaboration between the Maharbiz and the Rabaey labs, under the lead of Dr. Rikky Muller, a fully implantable wireless μ ECoG system was developed that consists of a mixed digital-analog integrated circuit, which is bonded directly to a 64-channel platinum-Parylene μ ECoG array with monolithically integrated thin-film loop antenna [12]. The integrated circuit unifies chopper-stabilized amplification, digitization, digital multiplexing, and a wireless backscattering radio in a single chip that leverages the advantages of a 65 nm CMOS process to avoid the use of off-chip capacitors through digitally-heavy architecture. The system is fully wireless (both data and power) and surpasses state-of-the art by an order of magnitude regarding power consumption (224 μ W for 64 channels) and die area (1.72 mm² total) [140].

μ ECoG and the quest for optimal resolution

There is no consensus in the field, as to what constitutes optimal spatial sampling of the electrocorticographic signal, i.e. how far apart ECoG electrodes should be placed in order to extract the maximum amount of information without oversampling. Oversampling the available signal has a number of practical disadvantages. As neural recording electrodes are scaled down, their impedance increases to first order like the inverse of the electrode area [120]. That impedance increase contributes thermal noise to the recording that leads to a loss of small amplitude signals below the noise floor. Since the ECoG signal has a $\frac{1}{f^n}$ spectrum, as outlined in the last paragraph, high frequency signal components, that are implicated in local information processing [25] are strongly affected by increased electrode impedance (electrode modifications for impedance and noise reduction are discussed in chapter 5). Each

⁴Personal communication with Jonathan Viventi.

of the ECoG electrodes needs to be connected to a front-end that amplifies the tiny cortical potentials that typically range from <1 to 100s of μV [23].

In the case of *passive* ECoG grids, which have no integrated electronics and are instead used in combination with discrete rack-mounted commercial amplifiers (e.g. from Tucker Davis Technologies, Plexxon, Neuralynx, and others) there is an innate trade-off between electrode density and areal coverage. Increasing electrode density while keeping the total area coverage constant implies an increase in the total number of recording sites, which leads to an explosion in wiring and interconnect complexity. Practical large-area high density designs are limited by the routing complexity of conductive traces between electrodes, the number of connectors that can be placed on the test subject's head, and by the number of available external amplifier channels. Routing a larger number of conductive traces can be achieved either by making the traces narrower or by accommodating additional traces in the third dimension through multilayer designs. Either way, the increase in channel count for passive ECoG grids comes at the expense of increased fabrication complexity (smaller minimum feature size, multi-layer cost and yield penalty, or both) and compromised signal integrity (higher likelihood of track damage for thinner tracks, shorts in multilayer structures, faulty connections at the transition between ECoG array and data acquisition electronics, and generally higher capacitive channel cross-talk for narrower or multilayer tracks).

Integration of active electronics with the microelectrode array helps to mitigate some of the above issues. Placing the first stage of amplification as close as possible to the recording electrode aids in maintaining signal integrity and the use of integrated multiplexing can lower the required routing and interconnect complexity [174]. Integration of a wireless transmitter using inductive coupling, infrared light, or ultrasound [155] for untethered powering and/or communication may reduce the need for transcranial wires entirely. However, even in the most optimistic untethered scenario, the area per channel available for the electronics will ultimately scale inversely to the number of channels, and the total power required, as well as the requisite bandwidth of the communication channel, will scale with the number of recording channels. Ultimately, heat dissipation constraints and FCC-mandated legal limits on the specific absorption or radiation⁵ will limit the total power available for any given device area, thus limiting the maximum possible channel density. Even if all of the above issues were to be overcome through miraculous advances in electrical engineering, what would a researcher or clinician do with that much data? Collecting data at overly high spatial sampling would put an unnecessary tax on storage space and post-processing capacity.

Thus, in order to use electrocorticography to its full potential in research and in the clinic, it is important to gain a sense of “optimal” spatial sampling. First of all, it is crucial to realize that the quest for optimal spatial sampling in ECoG without any additional constraints is not a well-defined scientific question. We could ask, for instance: “At what length scale does the information contained in the electrical potential measured on the surface of the cortex cease to contain *independent information*?” Unfortunately, what constitutes independence, is highly contextual, i.e. dependent on the experimental paradigm used to ask that question.

⁵See <http://www.fcc.gov/document/fcc-review-rf-exposure-policies>, accessed on 12/16/2013.

We have identified at least four broad classes of such paradigms in present literature:

1. Application of some statistical measure (correlation, coherence, mutual information, relative entropy, etc...) to spontaneous brain activity as a function of location followed by arbitrary numerical thresholding to determine independence. This is by far the most commonly taken approach. The resulting estimates for an independent length scale vary wildly based on the animal model used, on whether the array is placed epidurally or subdurally, on which brain area is studied and on the specific analysis strategy (statistical measure, threshold) employed (Some results found in literature are 1.25 mm in human [45] 0.79 mm in rabbit [44], 0.6 mm in rat and 0.9 mm in human [44], 0.06 mm in rat [72])
2. Independence of physiological responses; this approach is easiest to implement over sensory cortex by measuring receptive fields (visual, auditory, somatosensory) as a function of spatial location. In this paradigm a length-scale ceases to be independent when no difference in receptive field can be resolved across that length scale. The results of this approach may also vary as a function of the selected animal model the specific sensory area, and the set of stimulus parameters used for receptive field estimation.
3. Physical & anatomical independence; what is the “point-spread function”, the spatial extent of the measured ECoG signal in response to a (not necessarily physiologically meaningful) point-like stimulus. e.g. highly localized optogenetic stimulation? When two such stimuli are presented close to one another, at what length scale does it become impossible to distinguish that the evoked ECoG signal originates from two distinct sources?
4. Decoupleability through learning and plasticity (e.g. in a BMI paradigm); provided a test subject’s ECoG signal is coupled to the trajectory of an external actuator in such a way that desired control of the actuator requires the subject to volitionally and differentially modulate the spatial pattern of ECoG signal, at which length scale of spatial modulation does the test subjects ability to learn performing the BMI task above chance level break down?

In this thesis, little effort was spent on approach #1. Others have gone that route before with mixed results and in the author’s humble opinion, producing yet another number $d_{independent} \in (0\text{ mm}, 5\text{ mm})$ using a similar approach would be of limited utility. Some technological groundwork was laid towards approach #3 as described in chapter 6: an optically transparent μ ECoG array was developed that allows for simultaneous optogenetic stimulation and electrical recording through the electrode array. In conjunction with a highly focussed patterned light source (e.g. spatial light modulator (SLM) microscope [117]) one should be able to measure the ECoG point spread function in response to highly focal optical stimulation of neurons that express light-sensitive ion channels (e.g. Opsins [18]). This idea

became the starting point of another PhD student's thesis work and will thus not be included in this dissertation. This dissertation mainly explores paradigms 2 and 4 because they have tangible engineering implications.

Approach #2 suggests guidelines for optimal design of electrocographic arrays for applications in in vivo animal electrophysiology, where fast, robust and non-destructive functional mapping of receptive fields, ideally in chronic, awake, and behaving animal models, is paramount. We report on the utility of μ ECoG to create functional maps of the auditory cortex in rodents in chapter 7.

Approach #4 informs the design of minimally invasive neural interfaces for BMI. In chapter 8 we adapt a simple center-out BMI task for electrocortical control of an auditory cursor. We investigate if rats are able to learn to independently modulate aspects of the surface field potentials on closely spaced electrodes in order to obtain a reward.

1.6 Applications of ECoG

ECoG: Clinical applications in human subjects

Neural interfaces for use in human patients must meet a number of stringent requirements. Most importantly, they should not cause any permanent damage to the delicate neural tissue, as such damage can permanently impair important cognitive functions such as sensory processing, motor control, speech and memory formation. This criterion fundamentally excludes the use of any *penetrating* neural interface on healthy human brain tissue and limits the use of such interfaces either to brain tissue, which is so pathological, that it requires surgical excision (e.g. tumors [10]) or to very rare, experimental exceptions for the severely paralysed (e.g. BrainGate project [64]). Significant work has been undertaken in the last decade to lower the invasiveness and risk of penetrating neural interfaces and to boost their life time and signal stability [105]. However, the marvelous human immune system that opposes the presence of foreign bodies in what is arguably the most important of our organs, proved to be a veritable opponent, rendering it rather unlikely that penetrating neural interfaces will be deemed safe for human use anytime soon.

In the meantime, ECoG has been established as a common neurosurgical tool, because surface electrode arrays placed into the intracranial volume that is mostly devoid of a foreign body response, do not permanently damage the brain, and do not even break the blood-brain barrier. They are comparatively easy to place and remove, and hence became invaluable tools in standard neurosurgical practice such as the localisation of intractable epileptic foci.

Localization of epileptic foci

Roughly 30% of the 60 million epileptics world-wide suffer from refractory (i.e. drug-resistant) epilepsy [173]. The main therapeutics alternative for such otherwise intractable epileptics is to localize the seizure onset zone and surgically remove it. As detailed earlier in this introduction, ECoG was originally developed, and used for decades, to guide the

accurate localization and complete surgical removal of the ictal onset zone. The efficacy of this approach for different subtypes of epilepsy has been extensively reviewed e.g. in [83] and there appears to be a trade-off between incomplete resection, which does not render the patient seizure-free, and excessive tissue removal that may incur neurological or cognitive deficits as side-effects. The ictal onset zone had been widely perceived as a cohesive patch of scarred brain from which the seizures originate until Warren et al. pointed out in 2010 that the seizure onset zone may actually be diffuse and disconnected [178]. Even more recently, Matsumoto et al. have reported highly localized pathological high-frequency oscillations in human patients suffering from focal epilepsy [106]. These discoveries strongly suggest that high-resolution μ ECoG may hold clinical value, as it would allow to localize cortical pathologies more precisely and to maximize surgical outcomes while minimizing removed cortical tissue volume (especially in conjunction with novel surgical techniques such as MRI-guided laser-ablation [166]) and to reduce associated side-effects.

Real-time functional mapping during surgery

Since the days of Franz Joseph Gall, who in 1819 introduced Phrenology, the idea that bumps on the skull correspond to brain areas with specific function, we have come quite far in our ability to localize function on the cortex. Not just for intractable epilepsy but for any type of brain surgery (e.g. tumor resection [10]), cortical mapping is key to ensure that important functional areas such as motor cortex or eloquent cortex remain undamaged. Currently, the gold-standard technique for localization of function in surgical planning is electrical-cortical stimulation (ECS) [3], which frequently causes accidental seizures [92].

Cheung and Chang published a passive ECoG-based mapping technique that allows to map eloquent cortex robustly with single-trial accuracy simply by engaging in a verbal task [31]. High-resolution μ ECoG sensors have the potential to greatly boost the spatial accuracy of such mapping techniques.

Brain-Machine Interfaces for the paralyzed

Brain-machine interfaces hold great promise to improve the quality of life for severely paralysed patients by enabling them to control external actuators, such as motor and communication prosthesis directly with electrical signals generated in their brains. Initial attempts at brain control in the 1990s focused on understanding how the brain represents native control signals (e.g. for the control of a real limb) and on using sophisticated non-linear algorithms to ‘decode’ those signals in ‘open-loop’, see e.g. [49] for early work. A major breakthrough in BMI neural engineering occurred at the beginning of this century when Donoghue [156], and almost simultaneously, Carmena & Nicolelis [28], and Schwartz [163] realized that when the brain is provided with feedback of actuator performance, it is far better at learning a simple linear mapping of neural firing rates onto actuator degrees-of-freedom through plasticity, than our complex pattern recognition algorithms are at interpreting naturally occurring neural code. A schematic closed-loop BMI setup is shown in Fig. 1.3. As early as 1972, Brind-

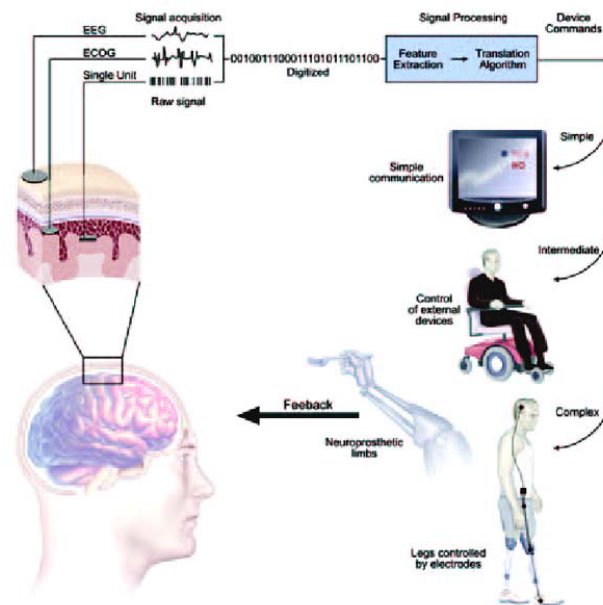


Figure 1.3: The ‘closed-loop’ BMI concept. Neural signals, recorded with any available modality, are processed by a decoder that maps them onto the behavior of an actuator such as a motor or communication prosthesis. The test subject receives sensory feedback about the actuator’s action, and the subjects brain undergoes plastic changes to learn using the decoder to achieve a goal. Reproduced with permission from [93], ©2000-2013 Ovid Technologies, Inc.

ley and Craggs reported a correlation between voluntary movement and ECoG signals [19]. However, when BMI was first demonstrated at the beginning of this century, the notion dominated that resolving single action potentials was a prerequisite for high-performance BMI control [30, 35]. It was not until recently that the BMI community developed a pronounced interest in ECoG-based BMIs for the neural control of high performance motor and communication prostheses [146] because ECoG provides higher spatial resolution than EEG (which enables only BMI control of very limited complexity [94]) while causing less damage to neural tissue than penetrating micro needle arrays [82, 94, 146]. For applications in BMI, developing high fidelity ECoG grids that optimally sample the cortex could enable smaller, less invasive, implants that provide more neural activity data for precision control. Rouse et al. recently demonstrated that monkeys can be trained to decouple gamma activity (power of electrocortical field potentials present between 65 and 115 Hz) on arbitrarily chosen electrodes to perform a 1-dimensional center-out BMI task [142] as opposed to functionally pre-selected electrodes commonly used in human ECoG-BMI experiments on patients who undergo pre-surgical mapping before surgical epilepsy intervention [14]. In 2012, E.F. Chang’s team at UCSF used ECoG recordings in epilepsy patients to infer which word a patient had heard

by recording γ activity over the auditory cortex [108,131]. Such studies may eventually lead to the development of a real-time speech prosthetic for patients with stroke-related aphasia or other forms of severe linguistic paralysis.

A case for ECoG in the treatment of neuropsychiatric disorders

According to a prominent theory of information processing in the brain championed by Fries [46], Buzsáki [22], and Knight [79], cross-frequency coupling between oscillatory features of the LFP subdivides the flow of neural information between and within brain areas into ‘words’ and ‘phrases’ (see [25] for a recent instructional review). Within that framework, many of the most devastating or prevalent neuropsychiatric disorders were found to be associated with abnormal oscillatory activity in brain potentials (“oscillopathies”). For instance, schizophrenics tend to display lower power in the γ band locally and abnormal long-range γ synchronization [170]. Patients suffering from clinical depression, often present with increased or asymmetric α and β power [6]. Bipolar disorder has been associated with decreased γ auditory evoked responses [124], and attention-deficit hyperactivity disorder (ADHD) was linked to increased auditory evoked responses in the γ band [183]. The brains of autistic children often feature excessive high-frequency oscillations [126]. ECoG excels at registering cortical oscillations, especially high-frequency oscillations that cannot be measured with EEG. An entire class of high-frequency oscillopathies may exist that would help distinguish and subclassify neuropsychiatric disorders, enabling more meaningful diagnoses, and more personalised and successful treatment of patients. The development of new psychoactive drugs relies strongly on trial and error; convincing animal models of psychiatric disorders are rare and far-between, and very indirect behavioral measures are commonly used to access efficacy in preclinical trials [47]. Many drugs strongly affect rhythms in the brain [4], and while animal physiology and metabolic response is often a poor predictor of a drug’s effect on humans [115], brain rhythms tend to be highly conserved across mammalian species [25]. Thus, we believe that there is merit to developing rodent models that mimic human oscillopathies and to evaluating drugs pre-clinically using μ ECoG by their ability to alleviate such oscillopathies. While we believe that ECoG will become invaluable in pharmaceutical development, transporting drugs across the blood-brain barrier will remain challenging, and systemically delivered drugs will always come with some degree of side-effects. Remarkably, some purely electric non-pharmaceutical interventions such as Deep Brain Stimulation (DBS) for Parkinsons Disease (PD) have shown very promising results [132], which can be potentially translated to many other devastating neuropsychiatric disorders (OCD, deep depression [53, 85, 149]). But accessing deep brain structures with depth electrodes causes damage to healthy tissue, and thus harbors potential to induce cognitive or neurological disfunction. Since there are pathways between virtually all deep brain structures and cortex [130], it is conceivable that the same therapeutic effects that DBS can provide, can be achieved by highly targeted and locally specific epicortical stimulation [54], e.g. using a high-density μ ECoG array. Thus, there is hope that the diagnostic potential of μ ECoG may not only improve the evaluation and efficacy of psychotropic drugs but that

one day targeted electrical stimulation through μ ECoG may provide a novel independent treatment for severe neuropsychiatric disorders.

Part II
Engineering

Chapter 2

The Parylene C micro-flex process

2.1 Choice of materials

Choice of polymer

No known organic polymer can provide hermetic encapsulation to industry standards [167]. However, several classes of polymers are currently approved for use in implantable medical devices. The most common polymers found in neural implants are polyimide (PI), polydimethylsiloxane (PDMS), and polyparaxylylene (Parylene), recently reviewed by Hasler et al. [60]. The chemical structures of these compounds are shown in Fig. 2.1.

PI, better known under the tradename “Kapton”, subsumes a class of commercially available polymers films of which can be produced by spin-casting polyamic acid derivatives followed by thermal imidization at $\approx 350^\circ\text{C}$ [51]. Photo-patternable polyimide is quite commonly employed for the fabrication of flex-cables and flex-circuits in the microelectronics industry. However, such varieties tend to have poor barrier properties against moisture [5] and thus are unpopular in biomedical implants. PI offers some favorable material properties such as thermostability, high strength, and high electrical resistance. However, PI is not without its draw-backs: it is yellow-orange in color and non-transparent, rather stiff com-

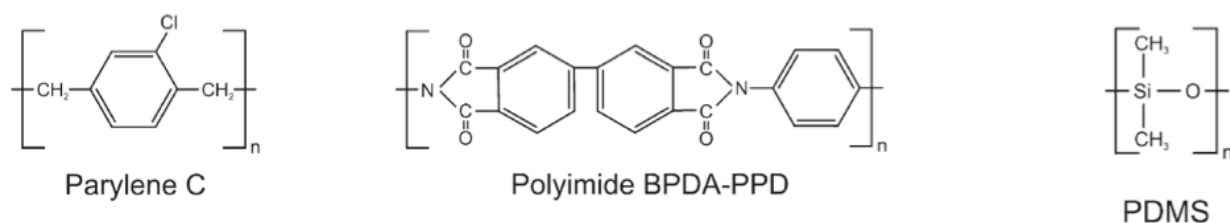


Figure 2.1: Chemical structure and common trade names of biocompatible polymers commonly found in flexible neural interfaces.

pared to neural tissue, and can be contaminated with non-reacted precursors of polyamic acid. Even though a number of studies indicate the PI is biocompatible [157, 179], it is not currently designated as a United States Pharmacopoeia (USP) bioimplantable material for human use.

Silicone, a class of polymers in which repeating siloxane units form the backbone, is hands-down the most successful class of polymers used for biomedical implants. Medical-grade polydimethylsiloxane (PDMS) is a USP Class IV bioimplantable material (i.e. approved without restriction for chronic implantation) and can be spin-cast or molded. Cured PDMS is a good insulator, remains flexible for years, and elicits minimal foreign body response. Still, the use of PDMS for biomedical implants is not without caveats: adhesion between silicone and conductors can be difficult to achieve, as is void-free deposition. Over- or under-cured PDMS still features reactive functional groups that are likely to elicit a higher level of undesired tissue response [4].

Poly(*para*-xylylene, better known under the trivial trade-name “Parylene” describes a class of semicrystalline thermoplasts, originally discovered by Michael Szwarc in 1947, that are deposited from the gas phase through pyrolytic dissociation of molecularly pure di-*para*-xylylene into *para*-xylylene that polymerises upon contact with a surface at room temperature into highly conformal Parylene thin films of ultra-high molecular weight [42]. Since the films are deposited from molecularly pure precursors, there are no concerns about batch-to-batch variations in quality, incomplete curing, or solvents leaking out over time. Since the precursor monomer is gaseous, it can penetrate complex topography, which results in highly conformal, pinhole-free films (at least for thicknesses $>2 \mu\text{m}$). Parylene C, a chlorine mono-substituted derivative, is a USP class IV bioimplantable material that is colorless and transparent across the entire visible spectrum. Unfortunately, in general Parylene C shows poor adhesion to metals, which necessitates the use of adhesion promoters such as γ -MPS (3-Methacrylopropyltrimethoxysilane) when used as substrate or encapsulant for conductors. However, fortunately for applications in neural engineering, Parylene C has very good intrinsic adhesion to platinum due to the chemical stability of Cl-Pt coordinative bonds [81]. Parylene derivatives can be surface-functionalized for even better adhesion or increased biocompatibility with a wide variety of functional groups (or entire bio-active molecules such as signaling peptides) via Friedel-Crafts-Acylation [175].

Due to Parylene C’s excellent mechanical, electrical, optical, chemical, and biological properties, we concluded that it is an excellent candidate to serve both as substrate and as insulator for high-density μECoG . At the time this work commenced in 2009, to the best of the author’s knowledge, no Parylene C based ECoG arrays had been published.

Choice of conductor

Conductors that are well-established for use in neural interfaces have been recently reviewed in [32]. Most commonly reported is the use of tungsten, stainless steel, platinum and platinum alloys (mostly alloyed with iridium), iridium oxide, and titanium nitride. However, in recent years, carbon (in the form of microfibers and nanotubes) and conductive polymers,

most notably poly(ethylenedioxythiophene) (PEDOT) have aroused increased interest. All of the above materials have their own pros and cons, with the optimum requirements for recording electrodes differing from those for electrodes intended to stimulate neural tissue. Stimulation electrodes need to inject enough charge to depolarize neural membranes, which often requires voltages sufficiently high to cause irreversible electrochemical processes that degrade the electrode material [33, 141] and/or are harmful to biological tissue [107]. The main goal of stimulating electrode development is to minimize such adverse electrochemical processes. Recording electrodes on the other hand, are designed to listen to very low-amplitude signals, typically ($1 \mu\text{V}$ - $500 \mu\text{V}$). Such low voltages are insufficient to cause redox reactions at the electrode/electrolyte interface and associated Faradaic currents. The major challenges for recording electrodes lie in minimizing the electrodes' thermal noise contribution by lowering their impedance, and in optimizing the electrodes' biocompatibility; once under attack by the immune system, an electrode of sub-par biocompatibility is quickly coated in electrically inactive scar tissue, which renders it useless for chronic neural recordings. In this work we were interested in developing μECoG arrays primarily for passive recording of neural activity and decided to use platinum based on its superior biocompatibility and excellent intrinsic activity in vivo. Last but not least, there are well-established methods to reduce the impedance of platinum electrodes through electrodeposition of Platinum Black, a highly porous form of platinum which we will explore in more detail in Chapter 5.

2.2 Wafer-level fabrication

We have made numerous refinements to our multilayer Parylene C MEMS fabrication process since it was first presented in [87], with variations later published in [89, 90]. This . In this chapter we are discussing the most advanced version of the process that was refined and adapted to micro-fabricate $15 \mu\text{m}$ thin 5-layer neural probe cables (2 patterned conductor layers sandwiched between 3 Parylene C layers) with conductor traces as thin as $5 \mu\text{m}$, at $10 \mu\text{m}$ pitch, and a trace length/width aspect ratio of up to 13,000, defined by lift-off. Cross-sectional diagrams of the individual processing steps are shown in Fig. 2.3.

Parylene C deposition

Parylene C (poly(*para*-chloro-xylylene), obtained from Specialty Coating Systems, was conformally deposited (Specialty Coating Systems Parylene Deposition System Model 2010; parameters displayed in Table 2.1) onto a particle-free p-type silicon carrier wafer. Great care was taken to avoid particulate contamination of the Parylene layer because such particulates greatly reduce lithographic yield in later processing steps. The wafers were taken directly out of the sealed wafer box and cleaned with a strong stream of N_2 . Wafers were placed into a wafer cassette, also prior cleaned with nitrogen. The wafer cassette was wrapped in very fine stainless steel mesh (obtained from McNichols, square weave, stainless steel type 304, 325 mesh, 0.0014" Wire, 0.0017" opening). We found that when deposited through the

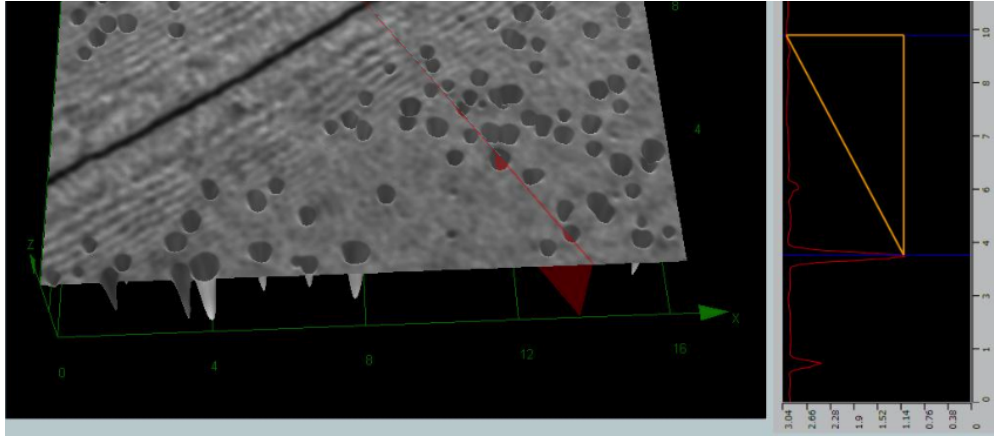


Figure 2.2: Pinholes in $< 2\mu\text{m}$ thin Parylene C layer observed with Olympus laser scanning microscope (LEXT). The hole marked in the profile is approximately $1.9\ \mu\text{m}$ deep.

Table 2.1: Parylene deposition parameters.

$T_{furnace}$	$T_{chamber}$	$T_{vaporizer}$	$P_{chamber}$	Mass	Thickness	Uniformity
$360\ ^\circ\text{C}$	$57\ ^\circ\text{C}$	$80\ ^\circ\text{C}$	25 mTorr	13.5 g	$5\ \mu\text{m}$	10 %

stainless steel mesh, 2.5 - 3 g of Parylene C dimer yielded approximately $1\ \mu\text{m}$ of Parylene C on the wafer with about 10% thickness variation across the wafer. That number should be recalibrated periodically as it tends to vary with the cleanliness of the Parylene tool. Also, the protective stainless steel mesh should not be reused: Parylene deposits on the mesh and changes the pore sizes; it can not be cleaned off easily using solvents or reactive ion etching. Total Parylene thickness determines ultimate device stiffness and is in practice limited to approximately $8\ \mu\text{m}$ per layer, which is the maximum thickness which can be etched through a 8-12 μm thick photoresist (SPR220) mask. Also, Parylene C layers must be thicker than $2\ \mu\text{m}$ for insulation purposes to avoid shorts due to pinholes in the Parylene C. Such pinholes are rather difficult to detect with conventional or even with electron microscopy. We were able to image them using an Olympus laser scanning microscope (see Fig. 2.2). We typically used $5\ \mu\text{m}$ thin Parylene for all layers.

Lithography for lift-off

The conductor was patterned in a bi-layer lift-off process. All lithography masks (5", dark field, chrome on soda-lime glass) were drawn in Tanner L-Edit v14-v16 and manufactured by laser direct-write at Fineline Imaging or Frontrange Photomask. A $1.3\ \mu\text{m}$ thick layer of G-line photoresist (OCG 825) was spun at 5000 revolutions per minute (RPM) onto the

Parylene. The wafer was soft-baked at 90 °C for 60 seconds and flood exposed (Karl Suss MA6, $0.14 \frac{J}{cm^2}$). A layer of I-line photoresist (OiR 10i 1.1 μm thick) was then spun at 4100 RPM and soft baked at 90 °C. The wafer was exposed with a dose of $0.06 \frac{J}{cm^2}$ and developed in OPD 4262 for 45-55 s. A 20 s etch in oxygen plasma (80 sccm and 200 W radio frequency (RF) power, process pressure ≈ 76 mTorr) was performed in the Plasma-Therm PK-12 RIE tool to de-scum the surface and improve adhesion for metal deposition.

Conductor deposition

For conventional μECoGs with metal electrodes we deposited a tri-stack of platinum (10 nm), Au (140 nm), platinum (50 nm), obtained from Sigma-Aldrich, by electron-beam evaporation, which we patterned by lift-off. Platinum serves as an ideal adhesion layer on Parylene C. It is chemically inert under physiological conditions but forms strong coordinative bonds with the chlorine substituted onto the Parylene C backbone. Unfortunately, due to the limited ductility of Pt and the thermal cost associated with Pt evaporation, thick homogenous layers of Pt on Parylene C come out cracked (see bond-pad micrograph in Fig. 3.3 for some early results). The thick layer of malleable gold in the middle of the stack helps amortizing thermal mismatch and other mechanical stresses preventing metal cracking as well as lowering the trace resistance. The top layer of platinum promotes adhesion to the next layer of Parylene C. For this adhesion mechanism to be effective however, it is crucial to achieve low base pressure before the evaporation, ideally on the order of $1 \cdot 10^{-8}$ Torr. In order to avoid Parylene crazing, it is important to control the chamber and substrate temperature to $< 100^\circ\text{C}$; we achieved highly improved results and stress-free devices with very little curl by switching to an electron-beam evaporator with a cooled chuck.

Lift-off

Lift-off is performed in an acetone bath under agitation with a weak stream of nitrogen for typically 1-2 hours. If lift-off is too slow or incomplete, heating the acetone in a 60 °C water bath can be of help. Sonication or other mechanically assisted methods of lift-off completion are a last resort and should be avoided as they can introduce holes into and bubbles under the Parylene C layer that lead to problems during subsequent vacuum processing steps (etching, metal deposition). Conventional strippers such as PRS3000 and 1165 should not be used on Parylene-coated wafers as they tend to delaminate the Parylene from the wafer.

Lithography for via etching

Thick photoresist, SPR-220 (8-12 μm was spun at 1800 RPM, soft baked at 115 °C, exposed using the low-vac mode of Karl Suss MA6 contact-aligner ($\frac{J}{cm^2}$), post-exposure-baked at 115 °C for 390 s, tank-developed for 5-12 min in MF26A developer, and hard-baked at 80 °C for 15 min.

Great care was taken to avoid cracking of SPR-220 due to fast heating or cooling. We used manual hotplates, placed cleanroom wipes underneath wafers, moved wafers very slowly onto the hotplate, removed them down slowly and placed them on a stack on cleanroom wipes to achieve an extremely gradual cool-down. It also proved crucial to wait at least 2 hours between exposure and post-exposure bake (PEB) and to make sure that the PEB lasted exactly 6.5 minutes. In this process step we recommend to err on the side of overexposing and overdeveloping the SPR-220 for, while slightly enlarged vias matter little, vias that are not properly cleared of insulator render devices electrically dead and are hence catastrophic.

Under no circumstances may 1165 or PRS3000 be used for lift-off or resist stripping. These strippers act like detergents and quickly lift the Parylene off the carrier wafer.

Parylene C etching

Vias were patterned in the Parylene C by oxygen plasma reactive ion etching (RIE) (oxygen, 200 W, 76 mTorr, 10 x 30 s intervals with 30 s cool-down periods in Plasma-Therm PK-12 RIE) through an SPR-220 thick (8-12 μm) photoresist mask. The etch rate for Parylene C under these conditions fluctuates around 440 $\frac{\text{nm}}{\text{min}}$; the etch recipe yields a sidewall angle of approximately 60°. The 30s on/off regimen is absolutely crucial: Plasma tends to heat up the metal tracks and to completely destroy the devices if the cool-down periods are not observed.

Vias, through-holes, and device outlines are etched in identical oxygen plasma etches. Initially, we used separate masks for vias and outlines. However, we realised that metal provides a robust etch stop for oxygen RIE. Hence we transitioned to defining vias and outlines on the same mask. This approach cuts down on the number of masks needed and helps to clear the vias by a 100% over-etch. However, it does not reduce lithographic complexity: given the modest selectivity of the etch recipe for Parylene C over SPR-220 of approximately 1.1, the resist (which, in some areas, can be as thin as 8 μm) had to be re-spun and re-patterned before etching each of the 5 μm Parylene C layers.

It is worthy of note that oxygen blanket etches of Parylene can result in the introduction of pinholes, presumably due to field-focussing near contaminants and defects in the film.

After the etch, the remaining PR is stripped in acetone.

Release

Since no adhesion promoter was used before Parylene C deposition onto the silicon carrier wafer, a mild detergent bath was sufficient to induce release. In some cases where the device footprint is particularly small, resist-stripping in acetone after the device outlines are etched, can induce release prematurely.

Optional steps

Indium tin oxide (ITO)

The conductor patterned by lift-off does not have to be a metal. We have successfully sputtered indium tin oxide (ITO), a transparent conductor, onto Parylene C. ITO was sputtered from an $In_2O_3 : SnO_2$ (10 wt% SnO_2) target in Edwards Auto 306 DC and RF Sputter Coater in argon (Ar) at a pressure of 2.2 mTorr (base pressure: $4 \cdot 10^{-5}$ Torr) and a DC power density of $1 \frac{W}{cm^2}$, yielding a 110 nm thick layer (sputter time: 33 min, deposition rate: $3.3 \frac{nm}{min}$).

Layer stacking

We have demonstrated devices with up to two conductive layers, interconnected by etched vias. In principle, it is straightforward to extend this process to n conductor layers by repeating steps 6-9 from Fig. 2.3. However, note that layer yield is generally multiplicative. Also, in practice, the increasing amount of topography, makes clean lift-off of fine features more difficult for multi-layer processes.

Adhesion promoters

Gamma-MPS (γ -methacryloxypropyltrimethoxysilane), a.k.a. A-174 is a standard industrial Parylene-on-metal adhesion promoter. We have deposited A-174 using an AMST Molecular Vapor Deposition System MVD100. We ran the process several times with and without deposition of the adhesion promoter. We have not observed any difference in device longevity. While Gamma-MPS, or the use of other adhesion promoters may be essential to ensure good adhesion of Parylene on stainless steel or other metals, platinum's natural chemical affinity for Parylene C renders adhesion promoters unnecessary. In fact, while adhesion promoters may improve the adhesion of Parylene to metal, they likely impede bonding between two sequential layers of Parylene C.

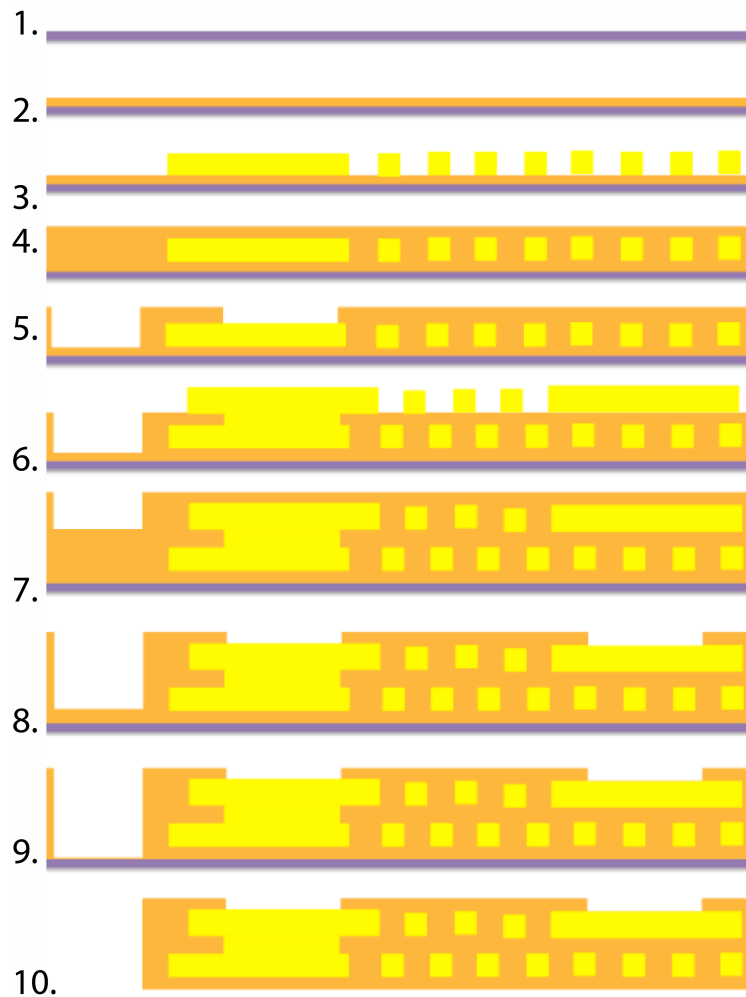


Figure 2.3: Cable Fabrication in cross-section. Parylene layers are indicated in orange, metal layers are yellow and the silicon carrier wafer is shown in blue. (1) Cleaning silicon carrier wafer (2) Parylene C deposition [$5 \mu\text{m}$] (3) Platinum-gold-platinum (10 nm Pt / 140 nm Au / 50 nm Pt) e-beam evaporation and lift-off (4) Parylene C deposition [$5 \mu\text{m}$] (5) Via etch in oxygen plasma (6) Platinum-gold-platinum (10 nm Pt / 140 nm Au / 50 nm Pt) e-beam evaporation and lift-off (7) Parylene C deposition [$5 \mu\text{m}$] (8) Via etch in oxygen plasma (9) Via etch in oxygen plasma (10) Device release in mild detergent. This figure was modified from [90] with permission ©2013 IEEE.

Chapter 3

Designs

In this chapter we present fabricated μ ECoG designs in roughly chronological order. We discuss design features and the intention behind them. We comment on whether the desired goals were achieved, and summarize what has been learned in each design iteration. Moreover, in as far as testing results obtained with the presented devices have not been discussed in other parts of this thesis in more detail, they will be briefly summarized here. We have made a conscious choice to only make use of fully biocompatible materials that are already FDA-approved for implantation in humans: platinum and Parylene C, as described in 2.1. These choices cannot guarantee that FDA-approval can be obtained for this technology but are expected to facilitate the regulatory process.

3.1 256 channel μ ECoG with 500 μ m pitch

The very first 256-channel μ ECoG we fabricated is shown in Fig. 3.1 (1). We successfully demonstrated with this first device that the Parylene C process allowed us to manufacture a μ ECoG thinner and denser than the most advanced μ ECoG in literature at the time [143]. While the engineering demonstration was largely successful, and allowed us to hold on to the “ μ ECoG crown” until publication of [174], it was also highly impractical. The electrode array was much too large to be conveniently placed over rodent cortex, and the printed circuit board, designed to carry sixteen 16-channel Omnetics connectors, was also too large (5” x 5”) to be chronically implanted in a rodent and unwieldy even for acute animal experiments. The following section contains a modified reproduction of [87], with permission of ©IEEE 2011.

The second iteration, sketched in Fig. 3.1 (2) that we published in [87] in 2011 was a 256 channel μ ECoG with an electrode pitch of 500 μ m and square electrodes 440 μ m x 440 μ m in size (Fig. 3.2). A 6 cm long Parylene C cable was monolithically integrated with the ECoG array on wafer level. This cable was thermocompression-bonded to a fan-out plastic circuit board (PCB) using the anisotropic conductive film (ACF) process described in more detail in 4.1. Cable and electrode pads were routed on separate metal layers and interconnected

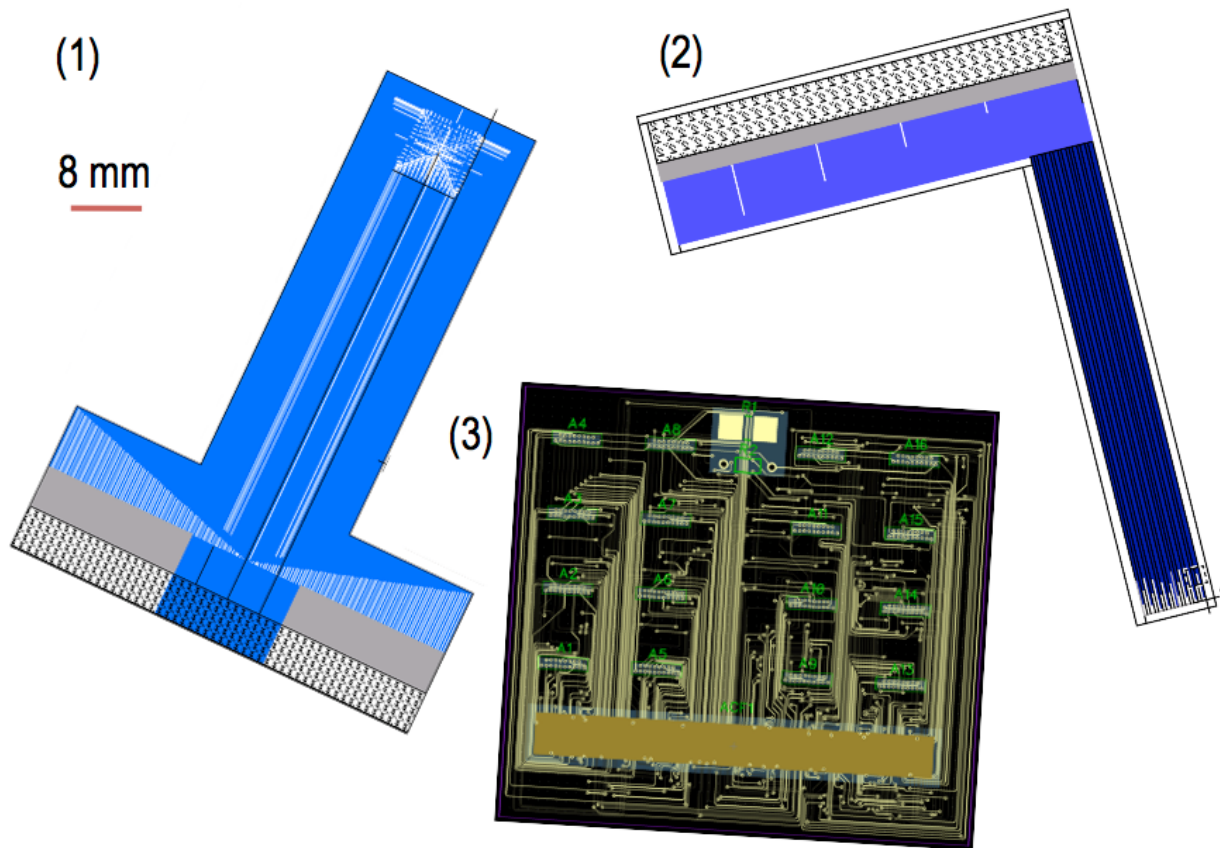


Figure 3.1: CAD designs: (1) Three-layer devices (Parylene/metal/Parylene), (2) five-layer device (Parylene/metal/Parylene/metal/Parylene), (3) fan-out PCB layout.

through etched vias. This enabled larger electrode pads than could be realized with a single metal layer, decreasing electrode impedance, improving the signal-to-noise ratio (SNR) and preventing spatial aliasing. The assembled device is shown in Fig. 3.3. Moving the wire routing to the lower metal layer, has enabled us to accommodate the active sensing area in a rodent craniotomy 3.5. But our primary neuroscience collaborators at the time (Bao lab) only had a 16-channel electrophysiology rig at their disposal. Thus, we were only able to test a few channels on an anesthetised rat *in vivo*. We eventually arrived at the conclusion that such large-area dual-metal-layer devices manufactured in our Parylene process are simply too low yield to be useful.

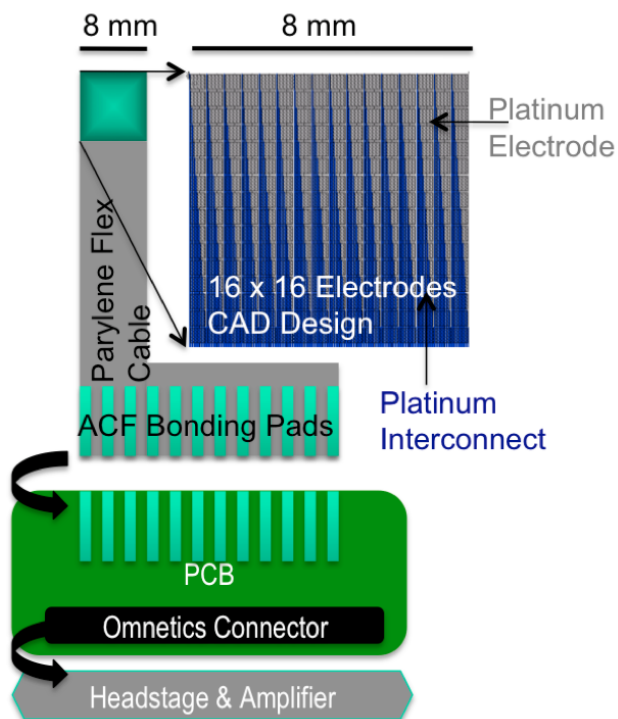


Figure 3.2: Full system concept: the 256-electrode grid (CAD design) is monolithically integrated with the Parylene cable on wafer level. The Parylene cable fans out into an array of pads, which are ACF-bonded to a PCB outfitted with Omnetics connectors compatible with commercial headstages and amplifiers. Figure and caption were partially modified from [87] with permission; ©IEEE 2011.

Characterization of the electrode-electrolyte interface by electrochemical impedance spectroscopy

We have characterized the electrode/electrolyte interface by electrochemical impedance spectroscopy (EIS) (Solartron constant-voltage mode, frequency sweep: 0.1 Hz to 10 kHz, AC-amplitude: 50 mV, open circuit potential: 265 mV). The device formed the active electrode, a platinum wire served as the counter-electrode and a silver wire served as the reference electrode. We used artificial cerebrospinal fluid (aCSF, Artificial CSF Perfusion Fluid, Harvard Apparatus, ion concentrations in mM: $[Na^+] = 150$; $[K^+] = 3.0$; $[Ca^{+2}] = 1.4$; $[Mg^{+2}] = 0.8$; $[PO_4^{-3}] = 1.0$; $[Cl^-] = 155$) as the electrolyte. The Nyquist plots have been fitted to a modified Randles Cell model to extract the line resistance ($R_s = 11.32 \pm 0.02$ k Ω), charge transfer resistance ($R_p = 102.5 \pm 0.5$ k Ω) and the parameters of the constant phase element (CPE: $n = 0.763 \pm 0.004$; $P = 51.8 \pm 0.4$ s $^n \Omega^{1+n}$), see Fig. 3.4.

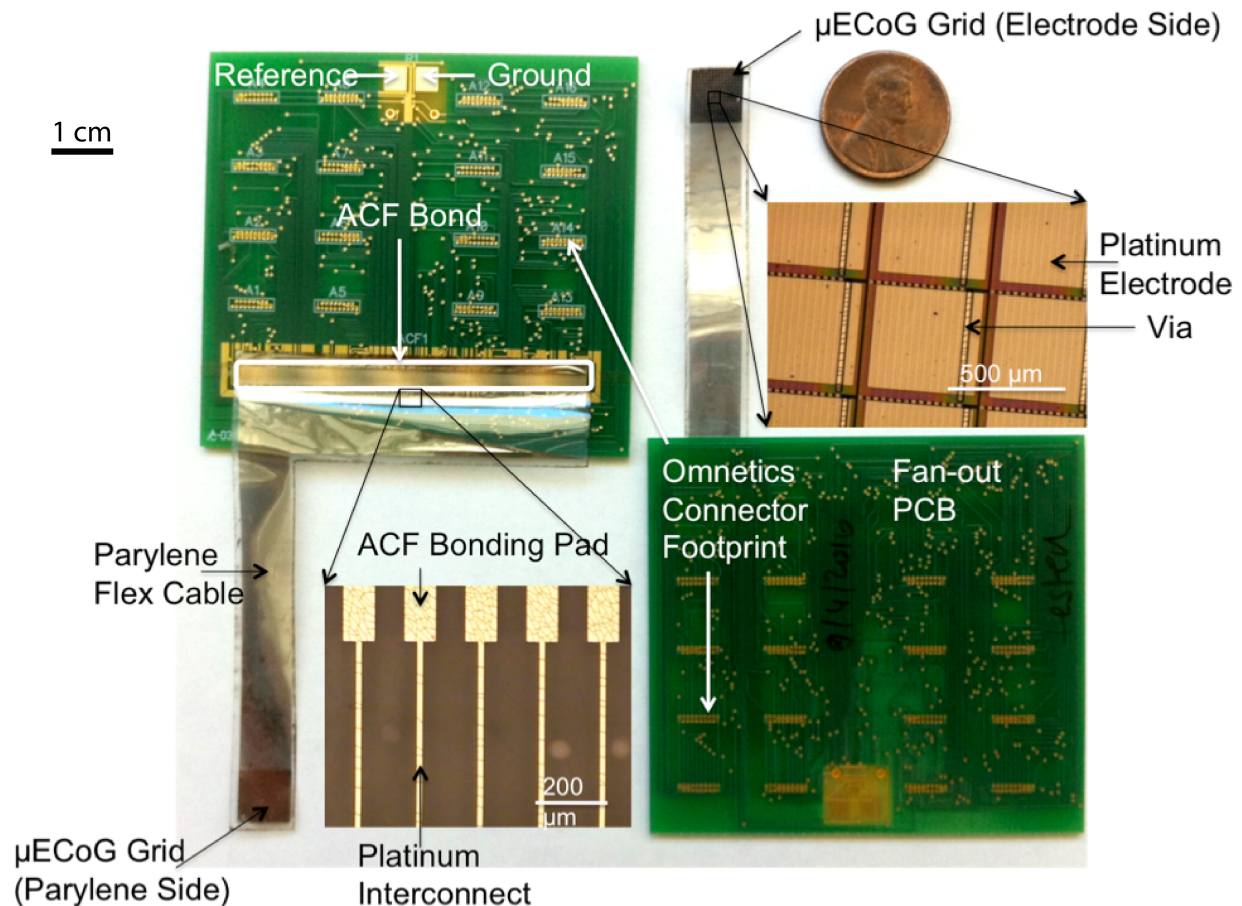


Figure 3.3: Annotated post-fabrication photographs show the released flexible electrode array with Parylene cable ACF-bonded onto the fan-out PCB. Micrographs show the transition region between Parylene cable and ACF bonding pads (bottom left) and a close-up of the electrode pads including plasma-etched vias (top right). Observing the micro-cracks in the ACF bond pads led us to switch from using a single thick Pt layer to a Pt/Au/Pt tri-stack. Figure and caption were partially modified from [87] with permission; ©IEEE 2011.

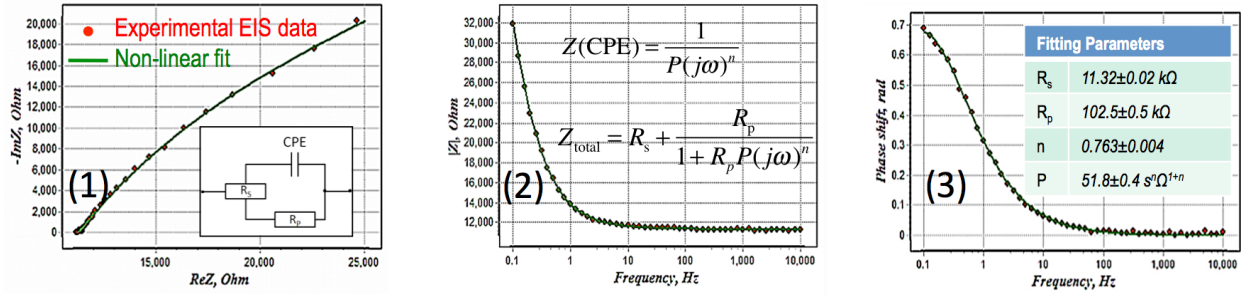


Figure 3.4: Characterization of electrode/electrolyte interface by electrochemical impedance spectroscopy: We have characterized the electrode/electrolyte interface by electrochemical impedance spectroscopy (EIS) between 0.1 Hz and 10 kHz using artificial cerebrospinal fluid (aCSF) as electrolyte. (1) Nonlinear fit of Nyquist plot, insert shows equivalent circuit of the modified Randles Cell. (2) Nonlinear fit of the impedance modulus $|Z|(f)$, insert shows impedance of a constant phase element (CPE) and total impedance of the modified Randles Cell. (3) Nonlinear fit of the phase $\theta(f)$, insert shows model parameters obtained by non-linear fitting of the EIS data to the modified Randles Cell model using EIS Analyser [16]. Figure and caption were partially modified from [87] with permission; ©IEEE 2011.

In vivo electrophysiological recordings

The μ ECoG array was tested *in vivo* on the auditory cortex of the rat. The University of California Berkeley Animal Care and Use Committee approved all procedures used in this study. One female Sprague Dawley rat was pre-anesthetized with buprenorphine ($0.05 \frac{\text{mg}}{\text{kg}}$) administered subcutaneously 30 min before anesthesia with sodium pentobarbital ($50 \frac{\text{mg}}{\text{kg}}$ for induction by intraperitoneal injection, $10\text{-}20 \frac{\text{mg}}{\text{kg}}$ supplemental as needed by intramuscular injection). Atropine ($0.1 \frac{\text{mg}}{\text{kg}}$) and dexamethasone ($1 \frac{\text{mg}}{\text{kg}}$) were injected subcutaneously. The rat was secured with a custom head holder and the cisterna magna was drained of cerebrospinal fluid to reduce brain pulsation and edema. An incision was made in the skin over the right auditory cortex, the temporalis muscle was removed, and the skull was exposed so that a wide craniotomy and durotomy could be made. Artificial CSF (same as for EIS characterization) was continuously applied to the exposed area. We placed the electrode array on the cortex and recorded responses (sampling rate: 384 Hz) to 25-ms white noise bursts played through a custom-made tube speaker inserted into the left ear to evoke responses in the right auditory cortex. The sounds were presented at 10-dB attenuation increments between 10 dB to 80 dB attenuation in order to sample a wide range of intensities. Responses to 63-71 presentations of each intensity were averaged. We have observed acoustic evoked potentials after a characteristic delay of approximately 30 ms post-stimulus. As expected, higher stimulus levels resulted in larger potential amplitudes and slightly shorter response times. (Fig 3.5, a and c). As a control we have moved the μ ECoG array to a location on the brain approximately 5 mm anterior to auditory cortex. As expected, no acoustic evoked

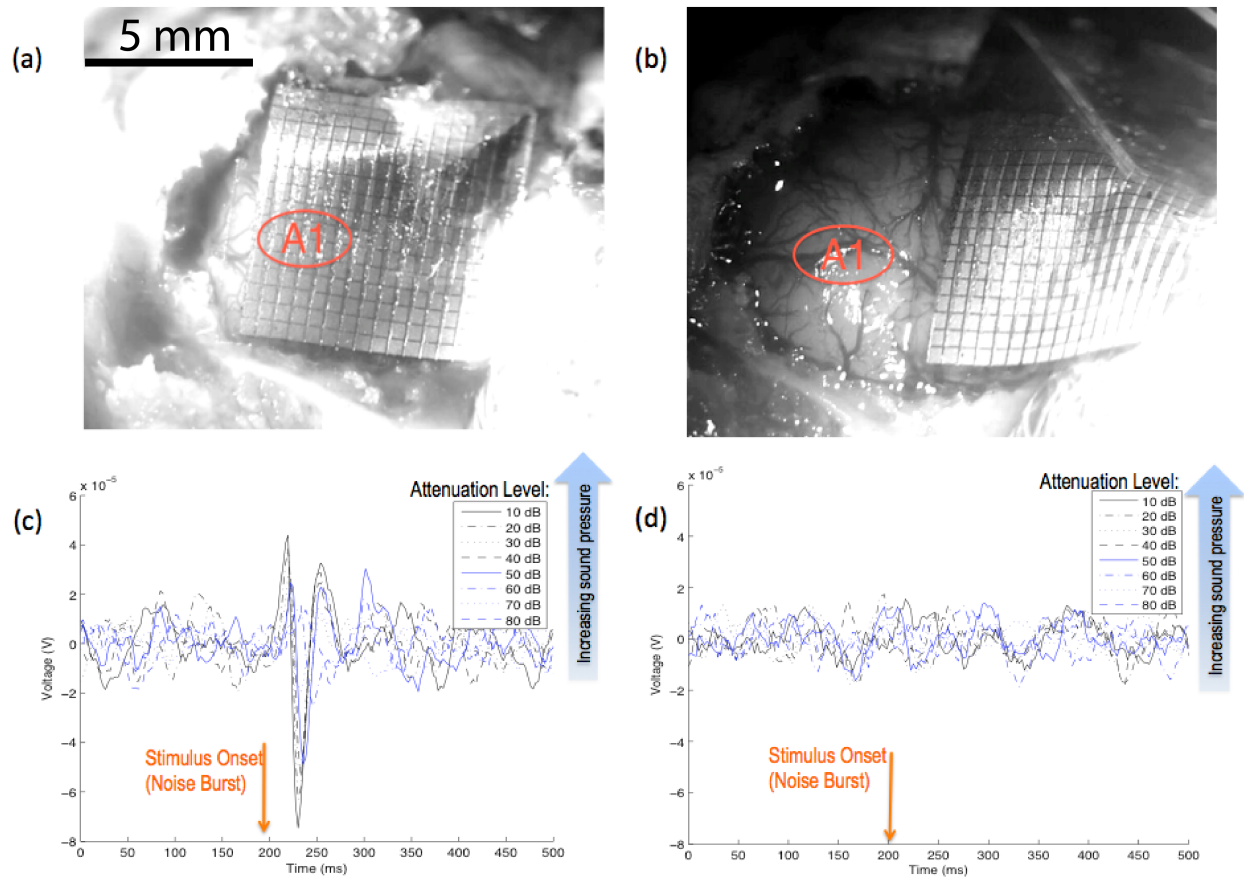


Figure 3.5: First *in vivo* experiment: Under anesthesia, a craniotomy was performed on a rat (female, Sprague-Dawley) and the ECoG array was placed subdurally on the primary auditory cortex (A1). (a) Grid placed on primary auditory cortex (A1): Acoustic evoked potentials were observed approx. 30 ms after stimulus onset, at attenuations below 50 dB (c). Note that the legend displays the *attenuation* level in dB. Lower attenuation levels correspond to higher sound pressure levels, which result in larger potential amplitudes and shorter response times. (b) Grid placed off A1 as control: Away from the auditory cortex, no acoustic evoked potentials could be recorded under identical stimulation conditions (d). Figure and caption were partially modified from [87] with permission; ©IEEE 2011.

potential has been observed in the control experiment (Fig. 3.5, b and d). Sound stimuli were generated using Cool Edit Pro (Syntrillium, 97656 Hz sampling rate) and a Tucker-Davis Technologies system (TDT System 3) was used for speaker calibration, sound delivery (through a STAX speaker), and electrophysiological recording.

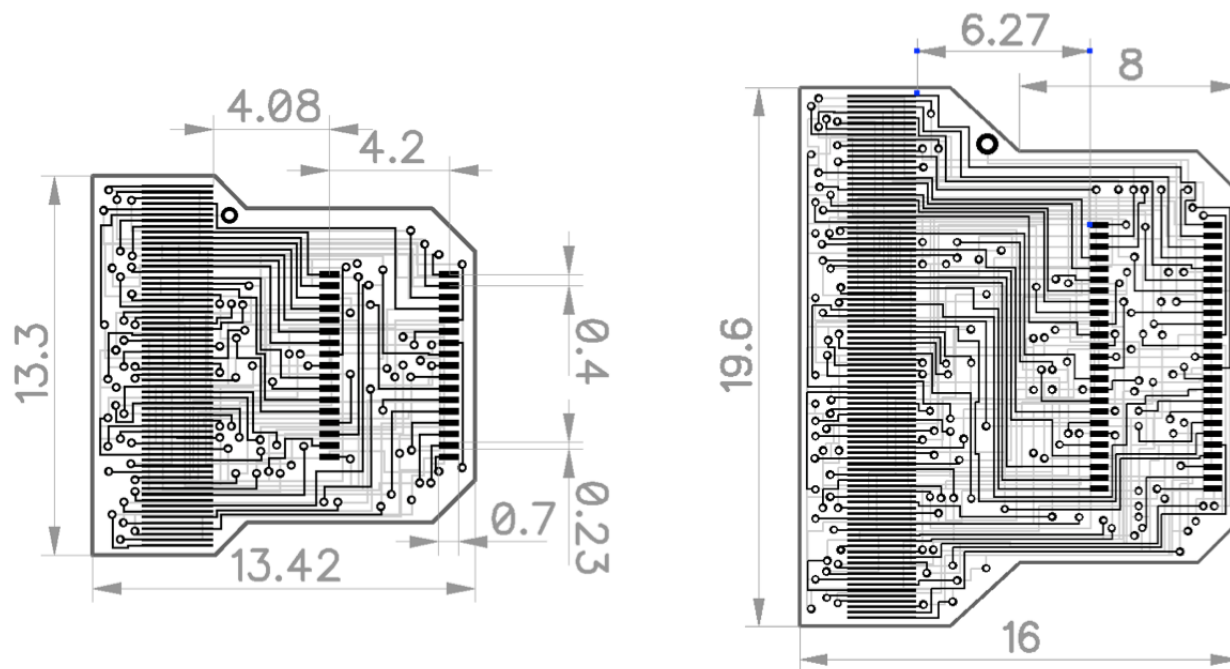


Figure 3.6: Highly miniaturized 4-layer adapter PCBs: The 64-channel (left) and 96-channel (right) adapter boards are practical for acute and even for chronic implantation in small rodents such as mice and rats. The PCBs feature 3 mil trace-space and 6-mil laser-etched vias. All dimensions are given in mm. We purchased these custom boards with an immersion-gold finish from Beta Layout, Ltd. (<http://www.beta-layout.com>).

3.2 Design of PCB adapters

Realising the impracticality of the PCB design shown in Fig. 3.1 (3), we decided to make a number of design changes. We abolished the very expensive (\$50) long-lead-time (8 weeks) Omnetics connectors in favor of 34-pin and 50-pin Hirose connectors (cost: \approx \$1; lead time: 24 h), for ≤ 64 -channel and ≤ 96 -channel μ ECoGs, respectively, that were used in TDT's Zif-Clip system. We also redesigned the adapter PCB to be dramatically smaller by migrating to a 4-layer board with 3 mil trace/space and 6 mil vias (Fig. 3.6). These PCBs were so small that the 64-channel version was successfully implanted chronically in the cranium of a mouse (!) in Karl Deisseroth's lab at Stanford (in collaboration with Viviana Gradinaru).

3.3 Design for simultaneous μ ECoG and Blackrock ‘Utah’ Array recordings

In order to investigate the origins of the μ ECoG signals more closely, we have contemplated to combine μ ECoG with simultaneous distributed intracortical single/multi unit recordings using a 96-channel Utah (now Blackrock) array [119]. For this purpose, we have designed and manufactured a family of devices with varying electrode sizes (50 μm - 400 μm in diameter) similar to Fig. 3.7, and etched through-holes for the silicon microneedles of the Utah probe. Unfortunately, post-fabrication, we realised that it is nearly impossible to align a 2D-array of microneedles to the perforations in the μ ECoG. Additionally, the 96-channel Utah array was prohibitively expensive for rodent experiments and we did not have an opportunity to test the idea in a non-human primate (NHP) at the time.

3.4 μ ECoGs for acute auditory neuroscience

For acute experiments on the superficial tuning properties of the auditory cortex in rat, we have developed the 64-channel and 96-channel designs shown in Fig. 3.8. The purpose of these devices was to cover the entire primary auditory cortex (A1) at the highest density (200 μm pitch, 8x8, and 8x12, respectively) feasible to achieve with single-layer routing (10 μm trace/space), while maintaining an electrode diameter sufficiently large (40 μm electrode diameter) to contribute less than 1 μV integrated thermal noise, while still having a chance to record from potentially present single/multi units. Furthermore, the devices in Fig. 3.8 have relatively long, slender cables (7 mm) and positioning flaps that allow moving the device precisely with tweezers without damaging the delicate metal traces. Available trace-free space on the array was used to maximize the size of through-holes for a higher degree of flexibility and conformity to the curvature of the the cortex (meshed design inspired by [75]). The perforations also allowed the introduction of penetrating laminar probes for simultaneous laminar and μ ECoG recordings, which are described in detail in Sec. 7.3.

3.5 μ ECoGs for chronic implantation

In order to conduct μ ECoG-based BMI experiments in chronically implanted, awake behaving rodents, we have developed a modified version of the acute devices (Fig. 3.9), which feature a minimized array foot-print that helps to keep the area of the craniectomy as small as possible for improved post-surgical recovery of chronically implanted animals. The cable was shortened so that it can rest flat against the skull of a rat with the array positioned over motor-sensory cortex and the PCB adapter board placed vertically (on-edge), roughly along the mid-line.

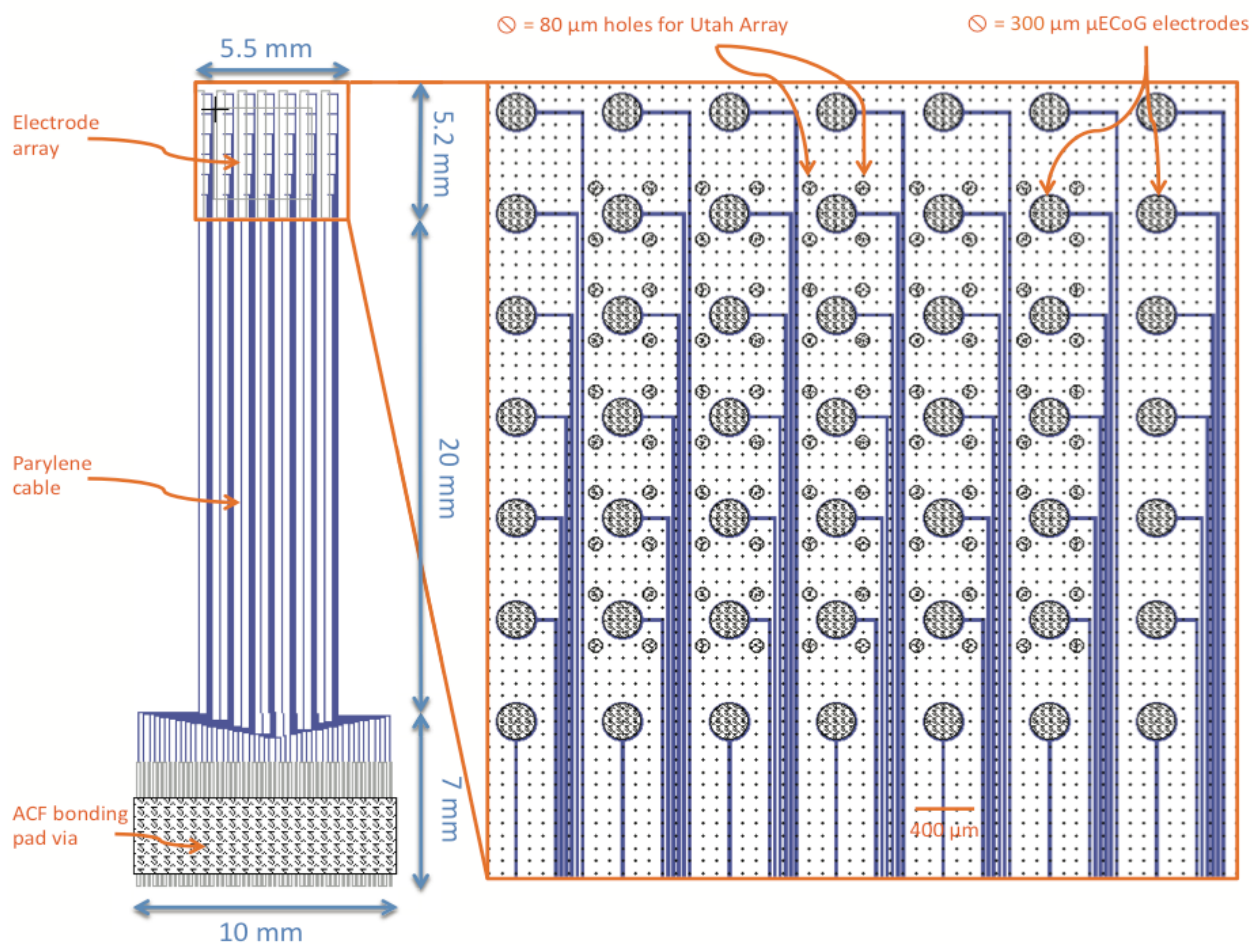


Figure 3.7: CAD design of μECoG for integration with 96-channel Blackrock ('Utah') Array introduced through plasma-etched perforations between the μECoG electrodes.

3.6 μECoG s with monolithically integrated antenna for wireless power delivery and communication

In order to develop a trans-cranial-wireless μECoG that allows to avoid skull-penetrating wires for data read-out and powering, we have proposed to implement the antenna (for both power delivery and data transmission) on the same flexible metal layer onto which the μECoG electrodes are patterned. This design avoids the need for a large rigid structure to be implanted into the intracranial space. The design of the device is shown in Fig. 3.10. The overall form factor was chosen to meet the following conditions:

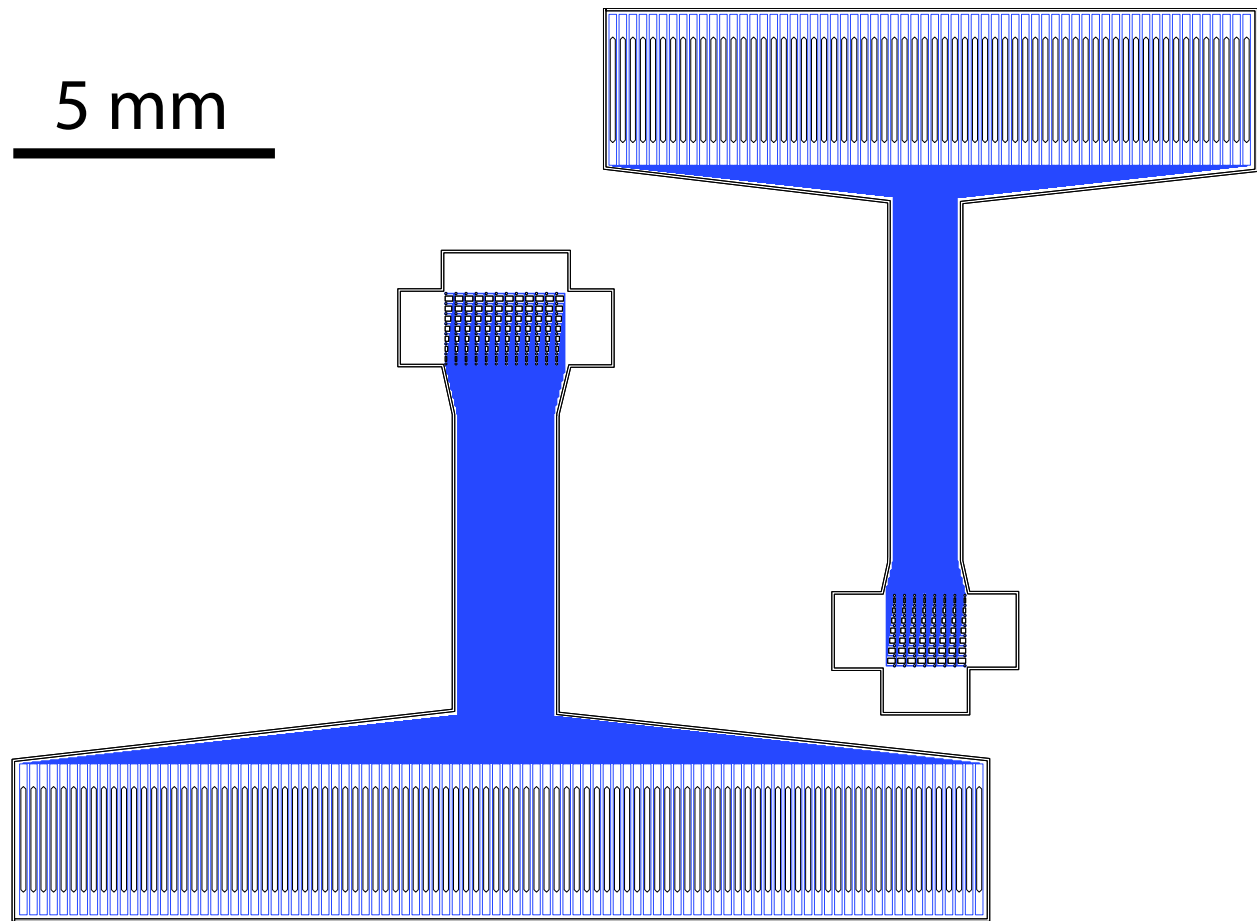


Figure 3.8: 96-channel (left) and 64-channel (right) μ ECoGs with 7 mm cables and positioning flaps for acute *in vivo* studies. Etched perforations between electrodes allow for simultaneous μ ECoG and laminar probe recordings. The electrodes are 40 μ m in diameter; electrode pitch is 200 μ m.

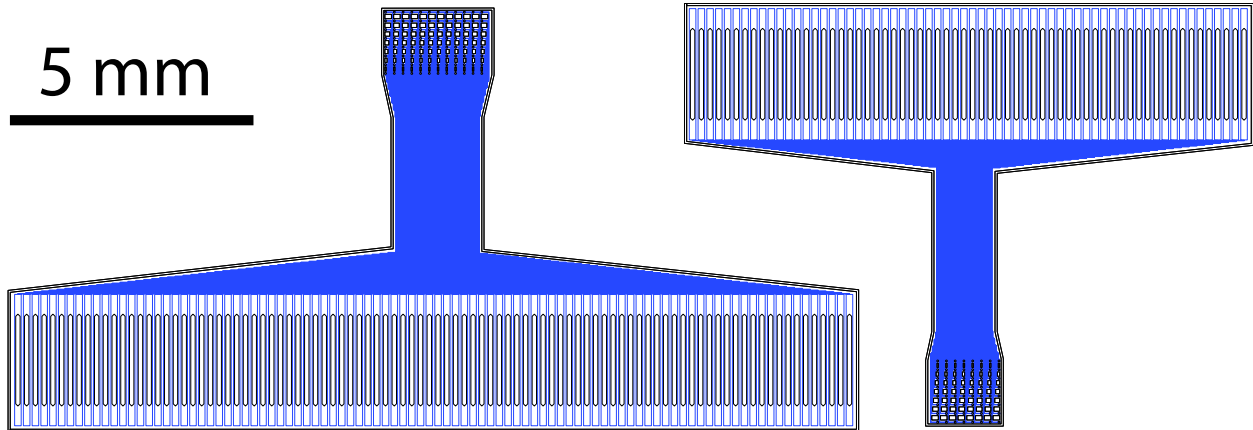


Figure 3.9: 96-channel (left) and 64-channel (right) μ ECoGs with 3 mm cables and a minimized implantable area (no positioning flaps) to enable minimally invasive craniectomies for chronic implantation and BMI studies. The electrodes are $40\ \mu\text{m}$ in diameter; electrode pitch is $200\ \mu\text{m}$.

- Higher density than any μ ECoG available for clinical use ($400\ \mu\text{m}$ electrode pitch, 8×8 channels)
- Large enough area to be interesting for use in humans, e.g. for communication BMI ($3\ \text{mm} \times 3\ \text{mm}$ total area of the sensor array)
- Small enough that it can still be tested on the cortex of a rat ($6.5\ \text{mm} \times 6.5\ \text{mm}$ total head size, including antenna)

The square single loop antenna trace ($750\ \mu\text{m}$ trace width) was simulated in Ansys high frequency structural simulator (HFSS) [12,13] to ensure that sufficient power can be coupled-in wirelessly across the skull without exceeding the maximum specific absorption ration (SAR) allowed by the Federal Communications Commission (FCC). The device features two internal references that effectively act as a physical common-average reference across the sensor grid’s field of view. The total area of both references equals to the total area of all μ ECoG electrodes (impedance matching) in order to reduce 60 Hz noise entering the IC front-end. The ACF bond pads for the references and the antenna are particularly large in area in order to ensure interconnect robustness and low impedance. In addition, the electrode diameter D and the electrode edge-to-edge spacing d obey the “Spatial Nyquist” condition $D > \frac{d}{2}$, i.e. they act as a spatial anti-aliasing filter [121] necessary for consistent spatial (spectral) pattern analysis of ECoG activity.

The full system (ASIC in conjunction with the Parylene C μ ECoG array) was successfully bench and *in vivo* tested and reported in [140]. Some photographs of the testing setup are shown in Fig. 3.11.

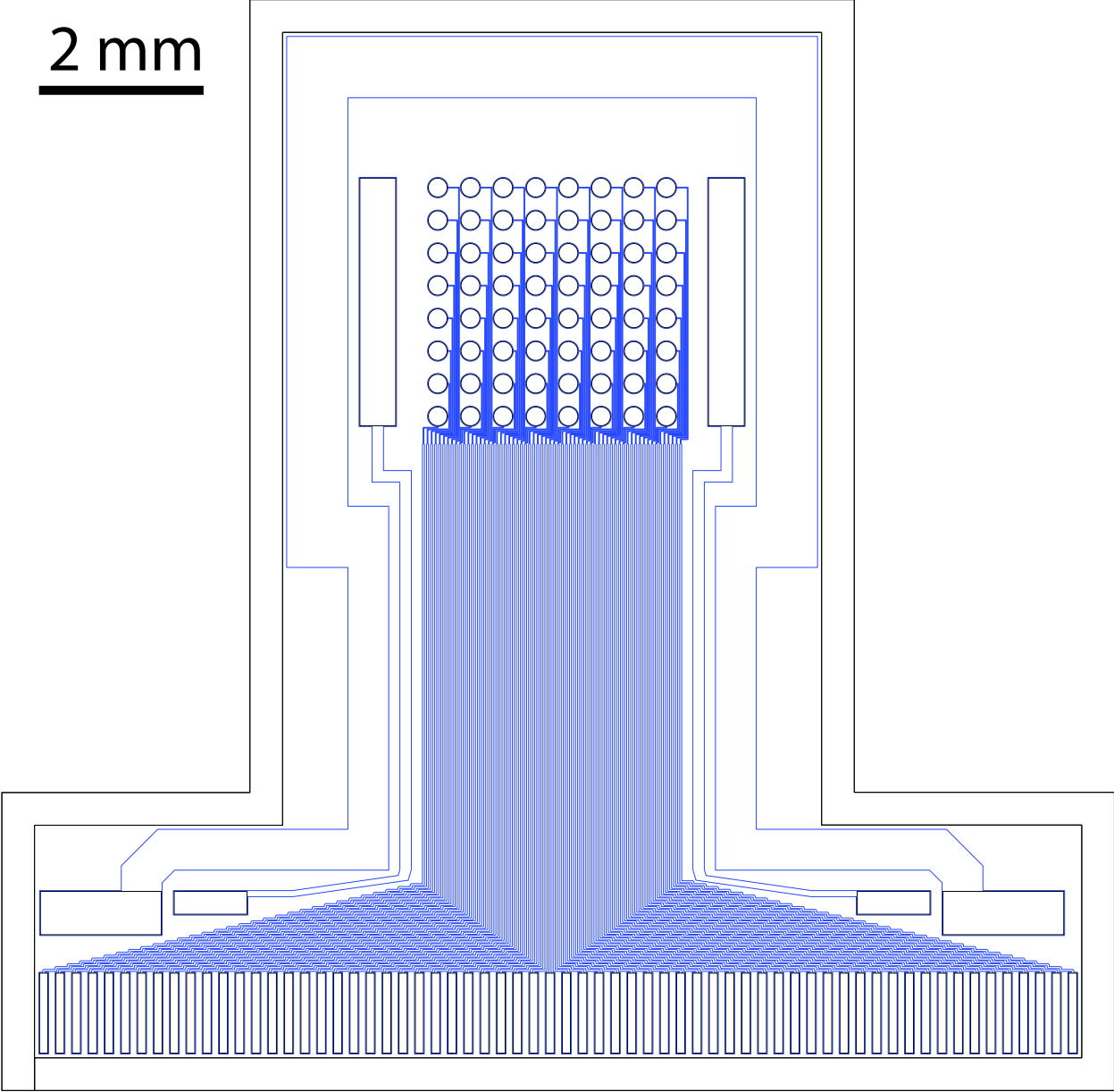


Figure 3.10: Wireless μ ECoG with integrated physical common-average reference and square loop antenna (6.5 mm \times 6.5 mm total). The array features 64 electrodes with a pitch of 400 μ m and an electrode diameter of 230 μ m.

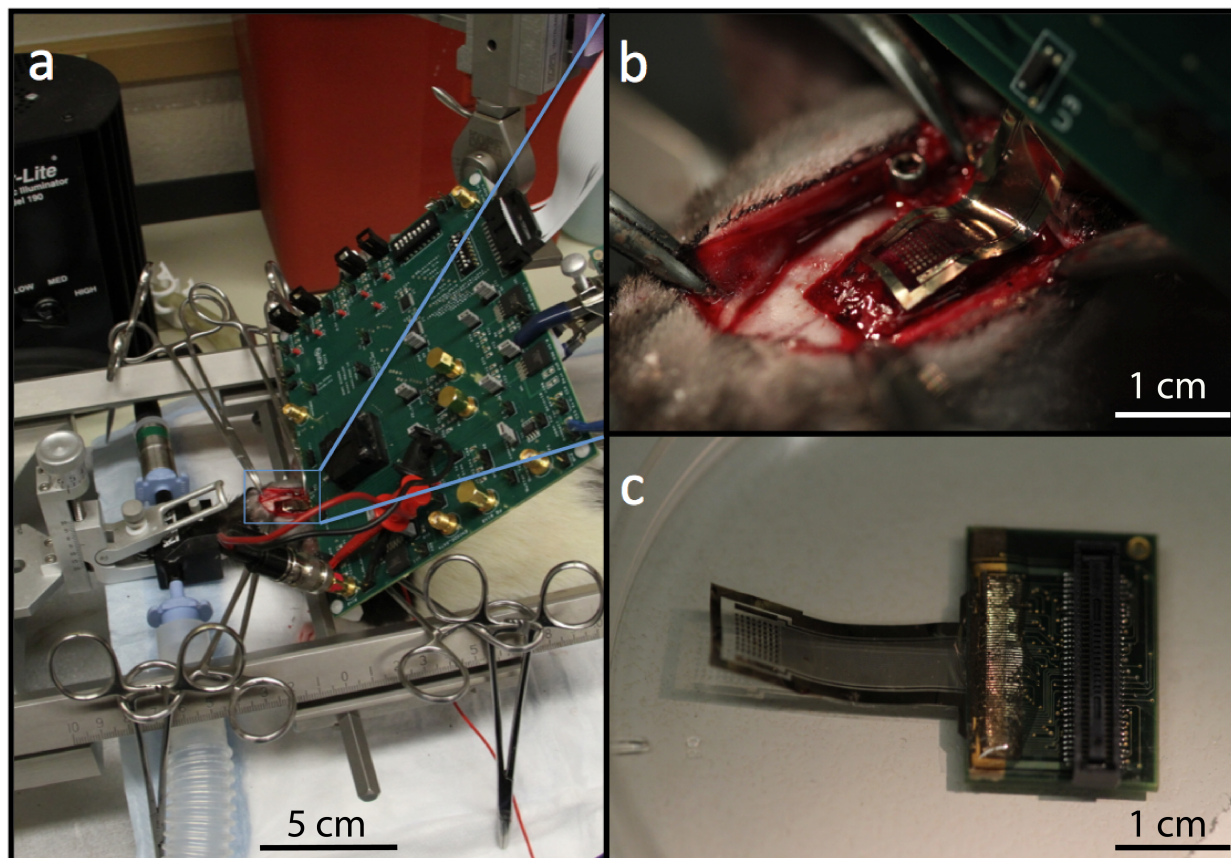


Figure 3.11: Testing of the wireless μ ECoG system *in vivo*. (a) Overview (b) Close-up of μ ECoG array with monolithically integrated antenna on rat cortex (c) μ ECoG array with monolithically integrated antenna ACF-bonded to a controlled-impedance adapter board. The ACF-bond is protected with UV-cured epoxy.

3.7 Optically transparent μ ECoG design

We have designed a 49-channel transparent μ ECoG array with an electrode pitch of $800 \mu\text{m}$ and a 16-channel linear transparent μ ECoG with an electrode pitch of $200 \mu\text{m}$ (Fig. 3.12). A 2 cm long Parylene cable was monolithically integrated with the ECoG array at the wafer level. In our prototype devices all conductors were formed by a tri-stack of chrome (10 nm Cr), gold (200 nm Au) and platinum (50 nm Pt). In the hybrid Au-ITO devices the linear bond pad array (pad dimensions: $100 \mu\text{m} \times 2500 \mu\text{m}$, $200 \mu\text{m}$ pitch) and most of the conductor traces (width: $20 \mu\text{m}$) consisted of Cr/Au (10 nm / 100 nm). However, near the microelectrode array, gold overlapped with indium tin oxide (ITO, 110 nm thick) and the electrodes were made entirely of ITO to achieve transparency (blue-shaded regions in Fig. 3.12). The cable was thermocompression-bonded to a fan-out printed circuit board

(PCB) using the anisotropic conductive film (ACF) bonding process (see Sec. 4.1). The 64-channel adaptor PCB (Fig. 3.6 (left)) was outfitted with two 34-pin ZIF connectors (DF30FC-34DS-0.4V, Hirose; obtained from Digi-Key) compatible with the ZIF-Clip neural recording headstage amplifiers made by Tucker Davis Technologies (TDT). The choice of biocompatible materials and the form factor of our transparent μ ECoG grids allow for acute and chronic application in rodent, feline, non-human primate and, in principle, in human subjects. Characterization and *in vivo* testing of these transparent μ ECoG arrays is discussed in detail in chapter 6. The text in this section has been modified from [89] with permission; ©IEEE 2011.

3.8 μ ECoG design for optical window in Macaque

Indium tin oxide works best for small-area arrays ($<5 \text{ mm} \times 5 \text{ mm}$), since longer ITO traces are prone to cracking. Besides, since Parylene C is transparent to visible light, larger and lower-density ‘mostly transparent’ arrays can be designed using traditional metallic conductors to feature large metal-free areas that allow optogenetic stimulation without interference with electrophysiological recordings. This approach was taken in the design of the μ ECoG array shown in Fig. 3.8. This 192 channel μ ECoG array is intended for NHP (macaque) recordings in the Sabes lab at UCSF in conjunction with a chronic optical window technique developed by Ruiz et al. [144]. The $8 \text{ mm} \times 12 \text{ mm}$ μ ECoG will be placed subdurally, below a transparent silicone inlay. The two 96-channel connectors, compatible with TDT’s ZC96 Zif-Clip headstage, will be located outside the stainless steel transcranial cylinder (Fig. 3.8, bottom right). The electrodes will cover primary motor cortex (M1) and primary somatosensory cortex (S1) at $700 \mu\text{m}$ resolution, while covering the periphery of the cylinder at the coarser resolution of 1.4 mm . The electrode diameter is $40 \mu\text{m}$.

3.9 Ultraflexible ‘Nanoflex’ cables for ultra small ‘nanoprobes’

Neurophysiologists are struggling to scale up the number of simultaneously recorded neurons while at the same time minimizing the impact of probe implantation on brain function. All currently reported electrodes that damage the blood-brain barrier during implantation cause a short term as well as a long term inflammatory tissue response that ultimately results in the formation of a glial scar around the electrode and in degradation of the recorded signal [105].

The exact mechanism of this process is poorly understood, however the combination of large, rigid electrodes and chronic micro-motion due to tethering forces on probes that are anchored to the skull has been implicated [11]. Miniaturizing the cable minimizes tethering forces at the probe-brain interface, allows multiple probes to be implanted in adjacent brain regions, and decreases the damage associated with deep brain implants. State of the art

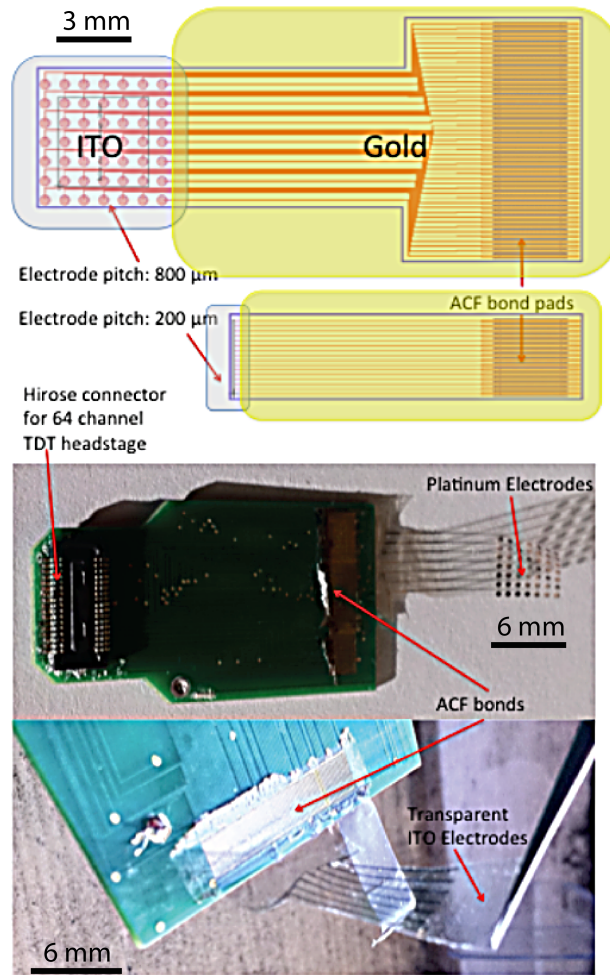


Figure 3.12: Transparent μ ECoG: CAD designs (top) and finished devices (bottom) bonded to adapter boards compatible with TDT's ZC64 headstage. The two 7×7 Parylene devices shown have the same arrays geometry as the as the metallic array shown in the upper photograph (CAD design shown in Fig. 3.7) but the ITO array at the bottom of the figure is nearly invisible due to its transparency. This caption and figure has been reproduced from [89] with permission; ©IEEE 2011.

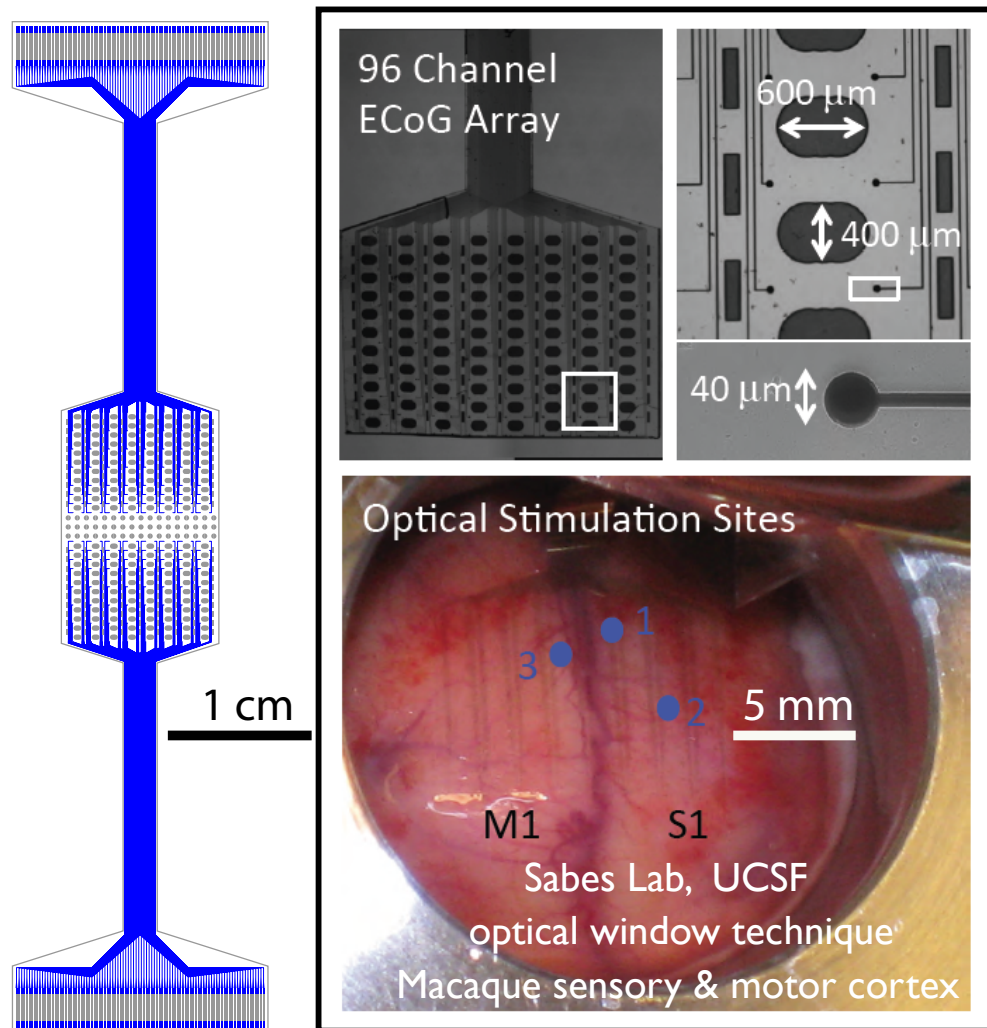


Figure 3.13: μ ECoG below a silicone cranial window in NPH. Left: CAD design of the 2×96 -channel electrode array (pitch $700 \mu\text{m}$ over S1 and M1, and 1.4 mm in the periphery; $40 \mu\text{m}$ electrode diameter). The large ($400 \mu\text{m} \times 600 \mu\text{m}$) perforations allow viral injections and intracortical insertion of an optical fiber for optogenetic stimulation. Image credit: The two photographs on the right were taken and labeled in part by Dr. T. Hanson and Dr. A. Yazdan, ©Sabes lab, UCSF, 2013.

academic flex cables [129] are 700 μm wide and contain 16 parallel Cr/Au trace lines (20 μm wide). The smallest form-factor commercially available 64-channels flex cables for neural probes use polyimide as structural polymer, feature 75 μm trace pitch and are 4.8 mm wide [1]. The text in this section has been modified from [90] with permission; ©IEEE 2013.

Cable design

The cables are comprised of two layers of patterned metal sandwiched between three layers of Parylene (5 μm), resulting in a total stack thickness of approximately 15 μm . Bond pads were patterned on the top metal layer and leads were routed on both metal layers, and interconnected through etched via-in-pads to minimize cable width. The cable width was matched to the widest dimension of the nanoprobe [37] (the bond pad array) to achieve ultra-compliant, free-floating cortical implants and to avoid displacing more than the bare minimum of tissue during cortical or sub-cortical implantation. The 32 channel cable is 270 μm wide with a 2×16 bond pad array on the probe side (70 $\mu\text{m} \times 70 \mu\text{m}$ pads, 120/150 μm pad column/row pitch). The 64 channel cable is 480 μm wide, with a 4×16 bond pad array on the probe side (50 $\mu\text{m} \times 50 \mu\text{m}$ pads, 120/125 μm pad column/row pitch). Cable lengths varied from 7 mm to 65 mm.

Mechanical analysis

Under normal physiological conditions the brain floats in cerebrospinal fluid, untethered to the skull. A neural probe cable (which is anchored to the skull on one end and to a neural probe inside the cortex on the other) introduces a tether that can exert force on the delicate neural tissue as the neural probe moves with the brain relative to the skull under the influence of cardioballistics, respiration, and inertial effects. Such forces are directly proportional to the bending or torsional stiffness of the cable, which for small displacements is assumed to behave like a Hookean spring. We modeled a unit-length (10 mm) of the cable as a cantilever beam (with the clamped end at the PCB bond site) with a concentrated load at the end that is connected to the neural probe. In this case, according to Timoshenko beam bending theory, the bending stiffness in the lateral x (width) and y (thickness) directions can be calculated as follows [50]:

$$k_x = \frac{1}{4} E h \frac{w^3}{l^3} \quad (3.1)$$

$$k_y = \frac{1}{4} E w \frac{h^3}{l^3} \quad (3.2)$$

where E is the Youngs Modulus of the cable material, h is the thickness of the cable, w is the cable width, and l is the cable length. These parameters for the Neuronexus 64-channel cable and the Nanoflex 64-channel cable are listed in Table 3.1:

Table 3.1: Comparison of bulk material properties between Neuronexus and Nanoflex cables. This table has been modified from [90] with permission; ©IEEE 2013.

	E [GPa]	ν	w [mm]	h [μm]	l [mm]
Neuronexus Hx64 64	7.5 [8]	0.34	4.8	20	10
Nanoflex 64	2.75 [2]	0.4	0.475	15	10

Table 3.2: Comparison of calculated mechanical properties between Neuronexus and Nanoflex cables. This table has been modified from [90] with permission; ©IEEE 2013.

	G [Pa]	k_x [$\frac{N}{m}$]	k_y [$\frac{N}{m}$]	k_ϕ [$\frac{Nm}{rad}$]
Neuronexus Hx64	2.8	$4.8 \cdot 10^3$	$7.2 \cdot 10^{-2}$	$1.08 \cdot 10^{-5}$
Nanoflex 64	0.98	1.11	$1.1 \cdot 10^{-3}$	$1.57 \cdot 10^{-7}$

Since the area and thickness of the metal traces is small ($<1\%$) compared to the area of the cable composed of Parylene/polyimide, the Youngs modulus of the bulk cable material can be used with relatively little error as the overall Youngs modulus for the cable.

The torsional stiffness can be similarly estimated [184]:

$$k_\phi = G \cdot \frac{1}{l} w h^3 \cdot \left(\frac{16}{3} - 3.36 \frac{h}{w} \left(1 - \frac{h^4}{12w^4} \right) \right) \quad (3.3)$$

where G is the shear modulus for the material calculated as $G = \frac{E}{2(1+\nu)}$ where ν is the Poisson Ratio for the material. The calculated mechanical properties for the two cables are summarized in Table 3.2.

The Nanoflex cables presented here are $66\times$ less stiff than the Neuronexus cables in the thickness direction, and $3730\times$ more compliant than the Neuronexus cables in the width direction. Moreover, the Nanoflex cables have approximately $68\times$ less torsional stiffness than the Neuronexus cables.

Cables can be placed inside of cannulas for deep brain penetration

While the shorter cables (7 mm and 12 mm) are intended for free-floating recordings from the cerebral cortex, the longer cables (20 mm and 65 mm) could be introduced into ultra-thin cannulas (Fig. 3.17) for deep brain recording and stimulation (DBS) at a spatial resolution far superior to that of DBS electrodes currently available in clinical practice [132]. As DBS technology is gaining acceptance for the treatment of Parkinsons and other severe psychiatric disorders, we anticipate increased demand for such technology.

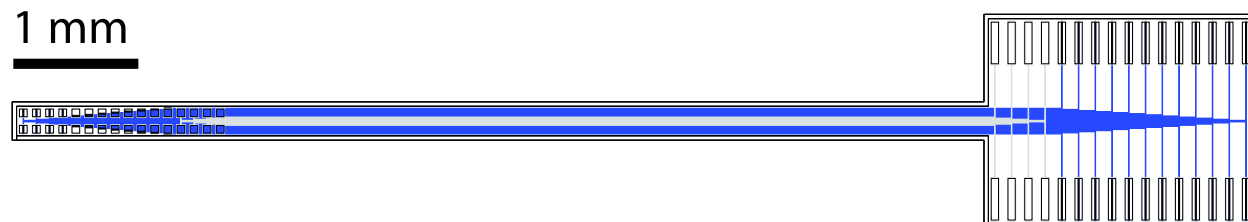


Figure 3.14: Cable layout for 32-channel cable (bottom metal layer shown in blue, top metal layer in grey, hatched regions indicate access and cut-out vias). This figure and caption have been modified from [90] with permission; ©IEEE 2013.

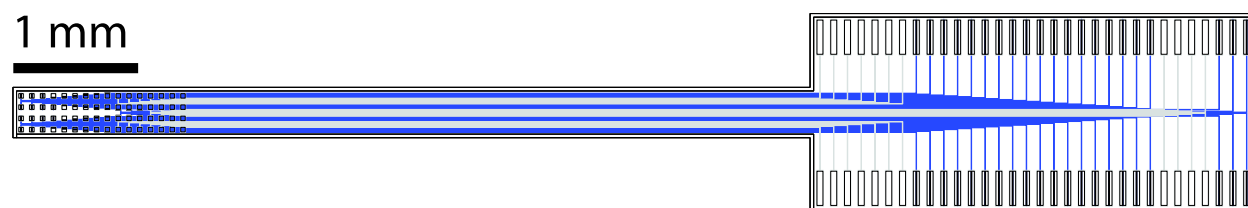


Figure 3.15: Cable layout for 64-channel cable (bottom metal layer shown in blue, top metal layer in grey, hatched regions indicate metal-access and cut-out vias). This figure and caption have been modified from [90] with permission; ©IEEE 2013.

Cables left unbonded on the probe side can be used for μ ECoG

The 32 channel Parylene cable can also be used as a μ ECoG provided the probe end is left unbonded. Electrochemical spectra acquired between 5 Hz and 5 kHz using a 64-channel impedance analyzer (nanoZ, White Matter, LLC) in phosphate-buffered saline (PBS) show a consistently low electrode impedance spectrum that is well fit by the Randles cell model (Fig. 3.18).

We have measured the series resistance of the cable traces as a function of length and calculated the trace resistance to approximately $60 \Omega\text{mm}$, which means that the trace impedance is negligible compared to the electrochemical impedance of the nanoprobe ($2\text{M}\Omega$ at 1 kHz) [37] and even small compared to the impedance of a probe bond pad on the cable ($20\text{-}70 \text{ k}\Omega$ at 1 kHz). Thus, it is safe to consider the cable trace contribution to Johnson noise is negligible.

Discussion

Our Nanoflex cables push the state of the art on Parylene flex technology [37] for neural probes in terms of length, aspect ratio, trace density, the total number of channels, and

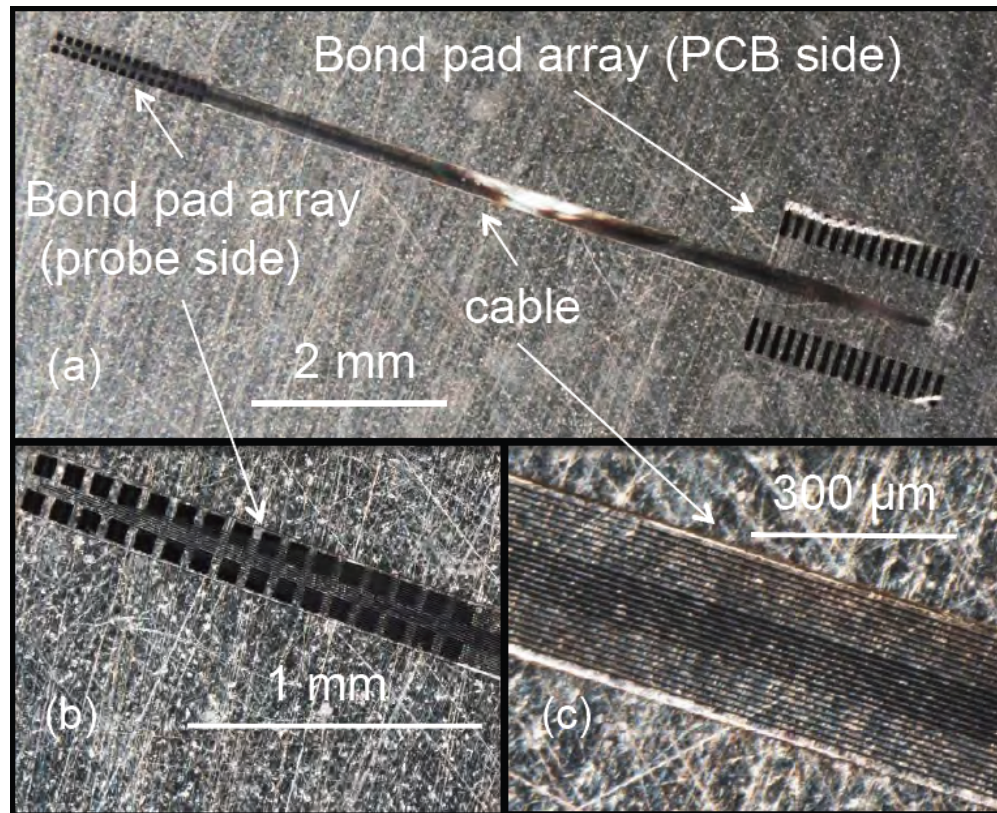


Figure 3.16: Nanoflex cables: (a) 7 mm long 32 channel Nanoflex cable. (b) Magnified view of the probe bond pad array. (c) Magnified view of high-density traces. This figure and caption have been modified from [90] with permission; ©IEEE 2013.

mechanical compliance. The cable width is one order of magnitude below that of commercially available devices (Fig. 3.19), which results in a reduction of stiffness by two orders of magnitude. Given the resulting reduced tethering forces, we expect the technology presented here to be of great utility for chronic neurophysiology in small animals, enabling long-term chronic high density epi- intra- and sub-cortical recordings and stimulation.

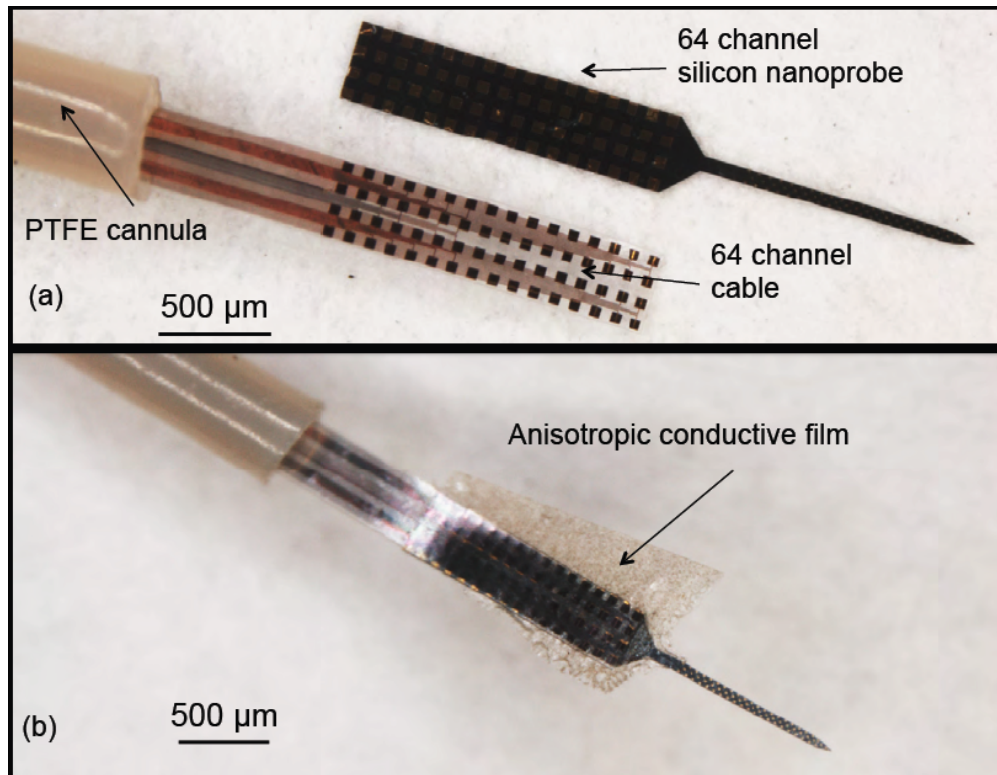


Figure 3.17: DBS probe assembly: (a) 64 channel cable introduced into an ultrathin-wall ($250\ \mu\text{m}$) semi-rigid PTFE cannula adjacent to a 64 channel silicon nanoprobe. (b) the cannula cable ACF-bonded to the 64 channel nanoprobe. This figure and caption have been modified from [90] with permission; ©IEEE 2013.

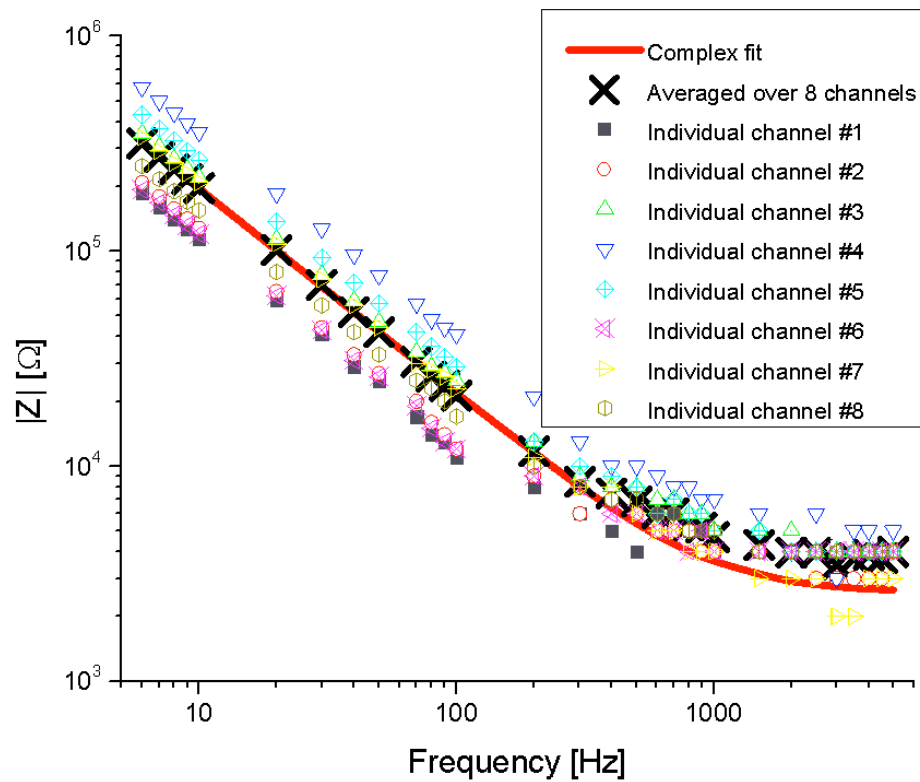


Figure 3.18: Electrochemical impedance spectrum measured across the interface of several cable electrodes (unbonded probe array) immersed in artificial cerebrospinal fluid aCSF. The electrodes show consistently low impedance ($<1\text{M}\Omega$) at 1kHz and are hence suitable for use as μECoG probes.

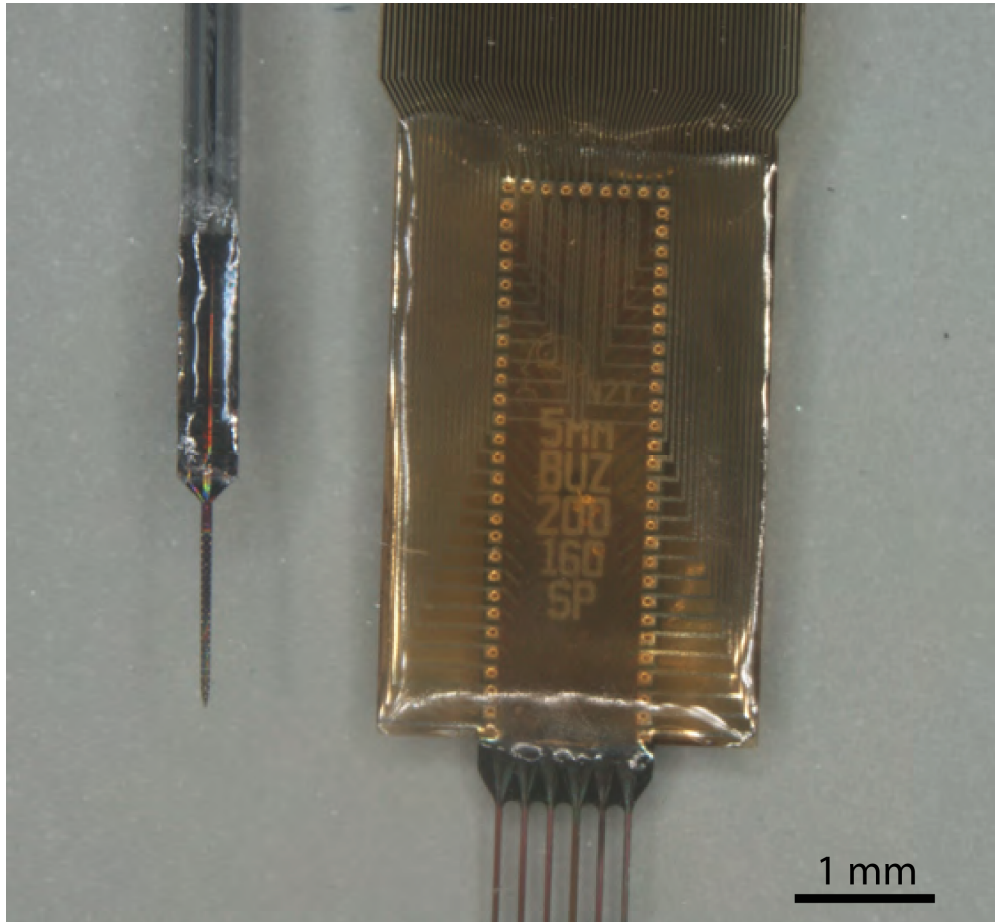


Figure 3.19: A 64 channel Nanoflex cable with integrated nanoprobe (left) alongside a commercially available 64 channel flexible cable with multi-shank silicon probe [1]. This figure and caption have been modified from [90] with permission; ©IEEE 2013.

Chapter 4

Assembly and packaging

Bonding of metalized Parylene C devices to adapter PCBs , and even more so to silicon nanoprobe, can be a formidable challenge for the pad dimensions used in this work. One cannot simply solder the pads for several reasons. Conventional solder bonds very poorly to platinum, and even if a solder-friendlier metal such as gold was patterned as the top layer of the metal stack, the metal-Parylene adhesion is not sufficient to support mechanical load. We successfully adapted anisotropic conductive film (ACF) bonding to interconnect high-density electrocortical grids, with adapter PCBs [87]. However, bonding with commercially available ACF suffered from low process yield when used for very small bond pad arrays, such as those of neural probe cables. Following the work of Sutanto et al [7, 9] we shifted our focus to two alternative techniques: low temperature solder thermocompression (LTST) bonding and silver epoxy thermocompression (SET) bonding. We have also developed a *de novo* interconnect technology that we named conductive sticky polymer thermocompression (CSPT) that relies on inkjet-printing of conductive polymer adhesive. The text in this section has been modified from [89, 90] with permission; ©IEEE 2011-2013.

4.1 Anisotropic Conductive Film Bonding

The wafer level devices were bonded to the PCB in an ACF process illustrated in Fig. 4.1 (a). ACF (3M 5552R, 2 mm wide) was pre-bonded to the PCB using an Ohashi HMB-10 table-top bonder equipped with a 2.5mm wide bond head (3s, 90°C, $10 \frac{kg}{cm^2}$). Parylene devices were aligned under a stereomicroscope using a custom alignment system comprising two vacuum chucks mounted on xyz -micropositioners, and tacked to the ACF film with a soldering iron heated to 200 °C. The final bond was performed using the HMB-10 (22s, 200° C, $20 \frac{kg}{cm^2}$) with the PCB optionally mounted in a custom-milled jig to protect the connector on the backside of the PCB. A typical bond is shown in Fig. 4.1 (b).

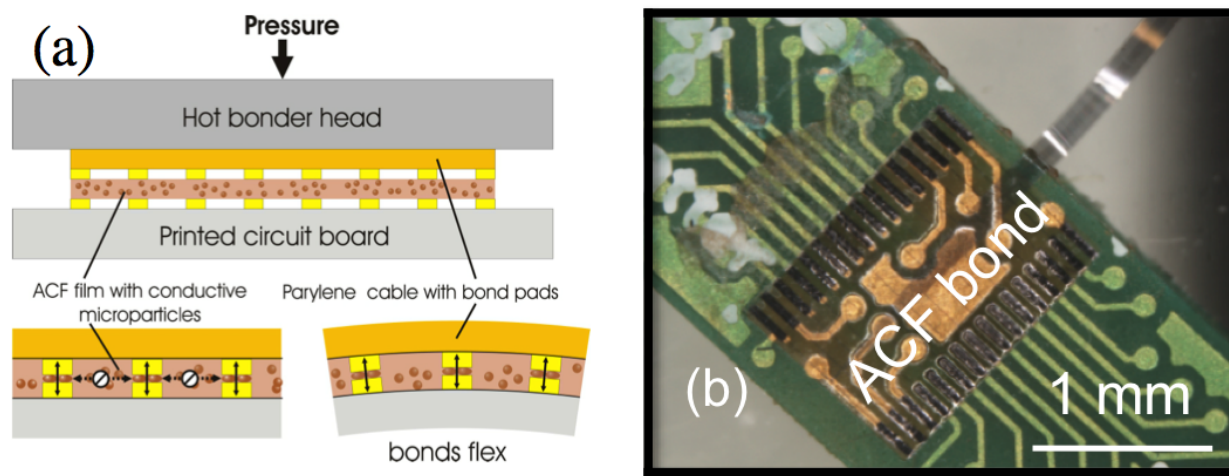


Figure 4.1: Anisotropic conductive film bonding: (a) Top: ACF film is thermo-compressed between complementary pad arrays. Bottom left: Gold-coated polymer microspheres establish a robust electrical connection. Between adjacent pads the micro particles remain surrounded by insulating thermoplastic resin that prevents shorts. Bottom right: ACF resin provides mechanical stability under flexion. (b) 32 channel cable ACF-bonded to adaptor PCB. This caption and figure have been modified from [89] with permission; ©IEEE 2011.

4.2 Low temperature solder thermocompression (LTST) bonding

As an alternative method to bond the Parylene cable to the PCB, the PCB pads were first tinned with a low-temperature solder paste (melting point (MP) = 138 °C) obtained from ChipQuik (part #SMDLTLFP). Excess solder and flux were thoroughly cleaned using isopropyl alcohol (IPA). Next, a cable was attached to a glass slide, PCB bond side face-up, using a drop of IPA to adhere the cable to the slide using surface tension. A thin layer of flux gel (ChipQuik, part #SMD29130CC) was applied to the bond pad area, taking care to limit application to the bond pad area only. The cable was then transferred to the PCB so that the bond areas of the cable and PCB were correctly aligned, using a microscope to fine-tune the alignment. Note that since the cable is mostly transparent, it is relatively straightforward to align the cable bond pads to the bond pads on the PCB. With the flux from the Parylene cable acting as a temporary adhesive, the assembly was then transferred to the bonder table. The bond head was heated to 230 °C and the bond pressure was calibrated using a load cell to achieve $10 \frac{kg}{cm^2}$ across the bond pad array. A silicone rubber sheet was placed over the bond area between the PCB-cable assembly and the bond head to achieve more uniform bonding pressure distribution. Cable and board were thermocompressed for 15 seconds and the PCB-cable assembly was set aside (Fig. 4.2 (a)). Next, a nanoprobe [37] was transferred

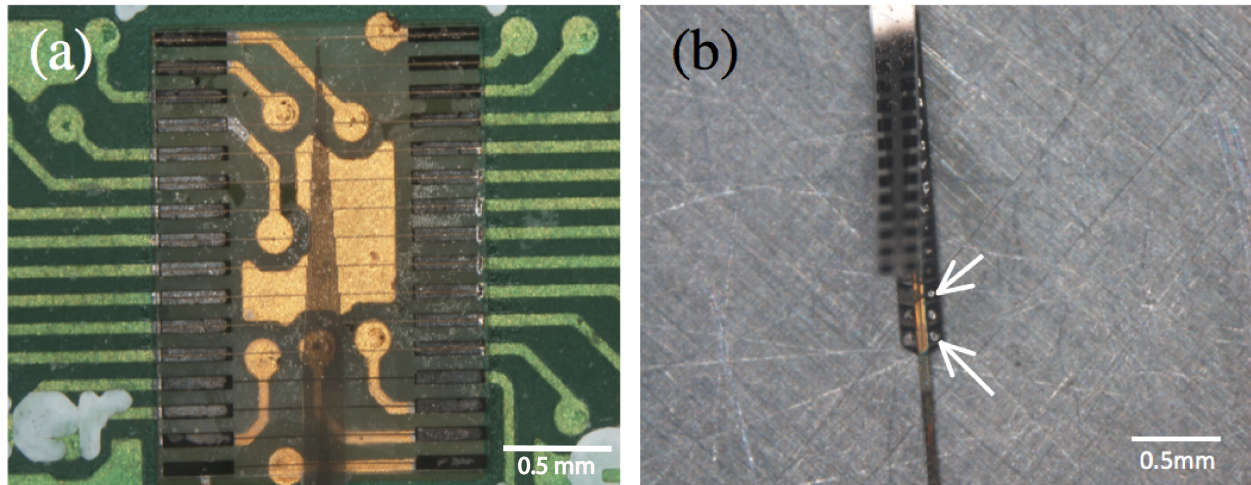


Figure 4.2: Low temperature solder thermocompression bonding: (a) 32 channel nanoflex cable bonded to an adaptor PCB. (b) Aligning the other end of the cable to a nanoprobe prior to bonding: solder bumps are visible on the nanoprobe bond pad array (arrows).

to a microscope glass slide with the bond pads facing up. The low-temperature solder was applied to the bond pad area of the silicon probe. The probe and slide were then transferred to a convection oven heated to 170 °C for 5 minutes to allow the solder to reflow on the probe bond pads. Excess solder was removed using a soldering iron and IPA. Flux was then applied to the bond area of the probe, and the probe bond area was aligned to the bond area of the cable (Fig. 4.2 (b)), with the flux acting as a temporary adhesive between the cable and the probe tip. The silicone rubber sheet was placed between the assembly and the bond head in order to distribute bonding pressure more evenly. A custom aluminum jig was machined to hold the PCB-cable assembly to facilitate this process and to avoid damage to the board-to-board connectors soldered to the backside of the PCB. The entire assembly was then bonded at a temperature of 400 °C and a bond pressure of $10 \frac{kg}{cm^2}$, for 5 minutes. The high bond head temperature was necessary because the aluminum jig acted as an efficient heat sink, which was desirable as it prevented solder reflow on the connector side of the adaptor PCB in addition to protecting the Panasonic board-to-board connectors. In the final step, both bond areas (probe and PCB ends) were underfilled and encapsulated with a thin layer of biocompatible UV-curable epoxy (Loctite 3526).

4.3 Silver epoxy thermocompression (SET) bonding

A third method to bond the Parylene cable to the PCB used conductive silver epoxy. The epoxy (Circuit works CW2460) was first patterned onto a glass slide in the exact pattern of the bond pad layout using a solder stencil (custom laser-machined stainless steel, 200 μm

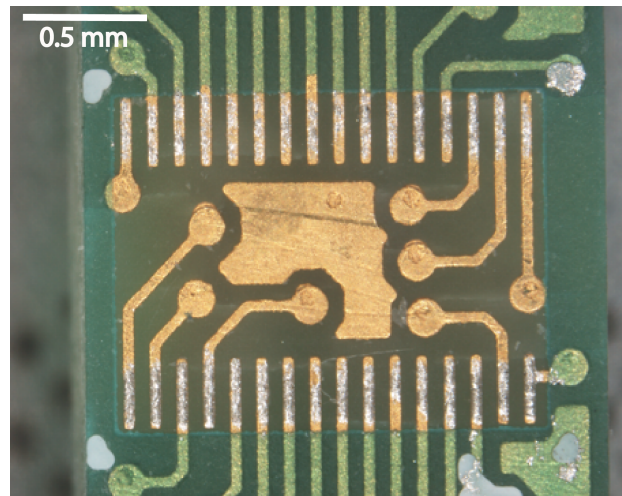


Figure 4.3: Silver epoxy thermocompression bonding: contact transfer was used to pattern epoxy on the pads of a 32 channel adapter PCB.

thick, obtained from PCB Pool). The epoxy was then pushed through the stencil using a custom mechanical press. Under a microscope, the epoxy pattern on the glass slide was aligned to the bond pads of the PCB, after which the glass slide and the PCB were brought into contact so as to transfer the epoxy pattern onto the bond pads (Fig. 4.3). Next, a cable was aligned to the bond area, using a drop of flux between the cable and the PCB as a temporary adhesive. The entire assembly was then bonded using the HMB-10 bonder (60 s, 230 °C, $10 \frac{kg}{cm^2}$). Setting the cable-PCB assembly aside, epoxy was again transferred to a glass slide, this time using stencils matching the bond pad pattern on the silicon probe. Under a microscope, the epoxy pattern on the glass slide was aligned to the bond pads of the probe, after which the glass slide and the probe were brought into contact so as to transfer the epoxy pattern onto the bond pads. The probe bond area was aligned to the bond area of the cable (which was already bonded to a PCB). The silicone rubber was placed on top of the assembly and the assembly was thermocompressed (5 min, 230 °C, $10 \frac{kg}{cm^2}$). In the final step, both bond areas (probe and PCB) were underfilled and encapsulated with a thin layer of Loctite 3526.

4.4 Conductive sticky polymer thermocompression (CSPT)

It is particularly problematic to use ACF on very small-area bond-pad arrays, such as the nanoprobe-nanoflex interface, in part because it is impractical to cut and handle ACF-pieces that small. If the used piece of ACF is larger than the bond-pad array, the resin is

pressed out past the edges of the device. The extra resin is very difficult to remove after the bond is complete (see e.g. Fig. 3.17), and can sometimes cause the entire assembly to adhere strongly to the working table of the ACF bonder, which can lead to destruction of the assembly during an attempt to separate it from the table. At the same time, it is also difficult to pattern solder or conductive epoxy using reflow, or stenciling/stamping techniques, respectively, with sufficient precision to avoid shorts.

We have found inkjet-printing to be an intriguing option for patterning conductive adhesive in a highly precise and controllable manner. However, jetting requires the ink to be of low-viscosity (10-12 cPs), to have a surface tension in the range of 0.028-0.033 $\frac{N}{m}$, and to not contain any particulates $> 0.2\mu\text{m}$ ¹, which eliminates commercially available solder pastes or conductive epoxies described earlier in this chapter. A mixture of PEDOT:PSS and D-Sorbitol (see Fig. 4.4 for IUPAC names and chemical structures) has been reported to work well as a conductive adhesive for the lamination of thin film organic electronics [127]. We have obtained commercially available PEDOT:PSS inkjet ink (0.8% in H_2O , Sigma-Aldrich) and doped it with D-Sorbitol (1 %wt). Sorbitol increases the conductivity of PEDOT:PSS [125] and grants the mixture adhesive properties. The doped ink was printed using a commercially available research grade Dimatix Materials Printer (DMP-2800), courtesy of the Subramanian lab at UC Berkeley. It proved to be easier to print the PEDOT:PSS:Sorbitol bumps onto the rigid components (adapter PCBs and nanoprobes) than onto the Parylene flex cables. However, it is conceivable to print the conductive glue onto the flex components before lifting them off the wafer if the PEDOT bumps can be rendered insoluble first, e.g. by soaking them in ethylene glycol [127]. A single coat of the PEDOT mixture resulted in rather shallow bumps ($<1\mu\text{m}$) with poor adhesive properties. However, after we calibrated alignment of the print head, we were able to repeatedly print onto the same location with 5-10 μm xy-alignment accuracy. We allowed the ink to dry for 10 s before reprinting. As shown in Fig. 4.5 (top) by printing 10 times over the same area, we were able to produce beautifully aligned bumps of sticky and conductive PEDOT:PSS:Sorbitol on top of PCB adapter boards, that were $20\pm 3\mu\text{m}$ tall. Fig. 4.5 (bottom) shows bumps of conductive, sticky glue, roughly 40 μm in diameter and 3 μm tall, on the bond pad array of the neural nanoprobe, produced by repeated printing ($3\times$) of only 4 drops of ink per pad (each time) onto the same location.

Under a microscope, the Parylene device was aligned to the PCB or to the nanoprobe. Next, a cable was aligned to the bond area and tacked onto the bond pad array using a soldering iron (200 °C) through a cover slip. The assembly was transferred to the ACF bonder, covered with the silicon rubber film, and thermocompression performed (30 s, 130 °C, 10 $\frac{\text{kg}}{\text{cm}^2}$). in order to exceed the melting point of Sorbitol (95 °C at the bond site) rendering the bumps adhesive. In the final step, both bond areas (probe and PCB) were underfilled and encapsulated with a thin layer of Loctite 3526.

¹From <http://www.fujifilmusa.com>, Dimatix Materials Printer Jettable Fluid Formulation Guidelines, accessed on 11/28/2013.

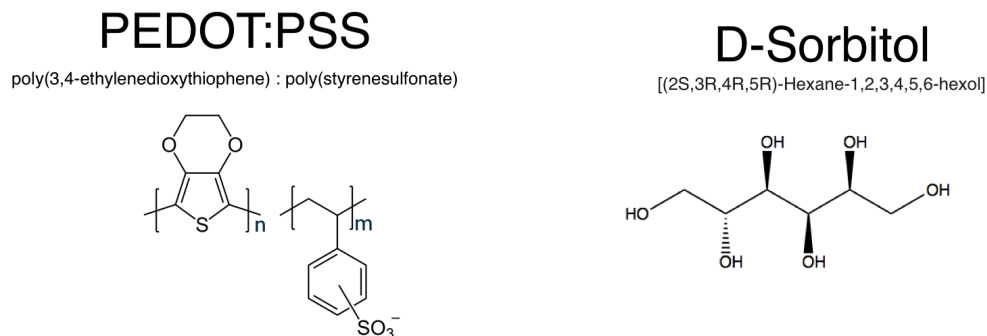


Figure 4.4: Chemical structure and IUPAC names of PEDOT, PSS and D-Sorbitol [127].

4.5 Juxtaposition of bonding methods

A major advantage of ACF bonding is that it not only provides electrical interconnects but also mechanical stability, even under flexion (see Fig. 4.1 (a), bottom right corner). The insulating thermoplast acts as an adhesive and loads are distributed between the metal pads and the Parylene surface between the pads. As a consequence, ACF-bonds do not require any underfill (although an encapsulation step may be indicated if the bond area itself is to be implanted). Unfortunately, we have found two major problems with ACF bonding of nanoflex cables. First, dimensions of our bond pad array significantly push the manufacturer's recommended minimum bond area of $(100\mu m)^2$, which often results in unsatisfactory yield of around 25%. Second, even is a successful bond is achieved, it is very difficult to remove excessive ACF without damaging the bond (Fig. 3.17).

The main problem with the other three methods is that they require underfill and encapsulation for mechanical stability, because, despite the fact that platinum shows excellent adhesion to Parylene C, the metal-Parylene interface cannot bear much mechanical load. The solder method will successfully bond up to 70% of the bond pads with extremely high success rate across attempts (>99%), meaning that 70% of the electrodes will be free from shorts and have low bond resistance. However, due to the nature of working with reflowing solder it can be difficult to increase the yield of working electrodes per device beyond 70% in this process. In contrast, the silver epoxy method has more of an all-or-nothing yield characteristic. When the epoxy process is successful, bond pad yield is >95%. However, the epoxy process requires an additional intermediate pattern transfer step (glass slide) such that success rate trial-to-trial is only around 50%. Thus, one should only consider using the epoxy process if very high (> 70%) yield of electrodes is critical.

The PEDOT:PSS:Sorbitol method is a novel development that was able to achieve approximately ($\approx 70\%$) yield as well. It may also be the only functional alternative for extremely small bond pads ($< (50\mu m)^2$) on very thin flex substrates. It offers the immense advantage that it does not require removal of excess material from tiny bond-pad arrays of

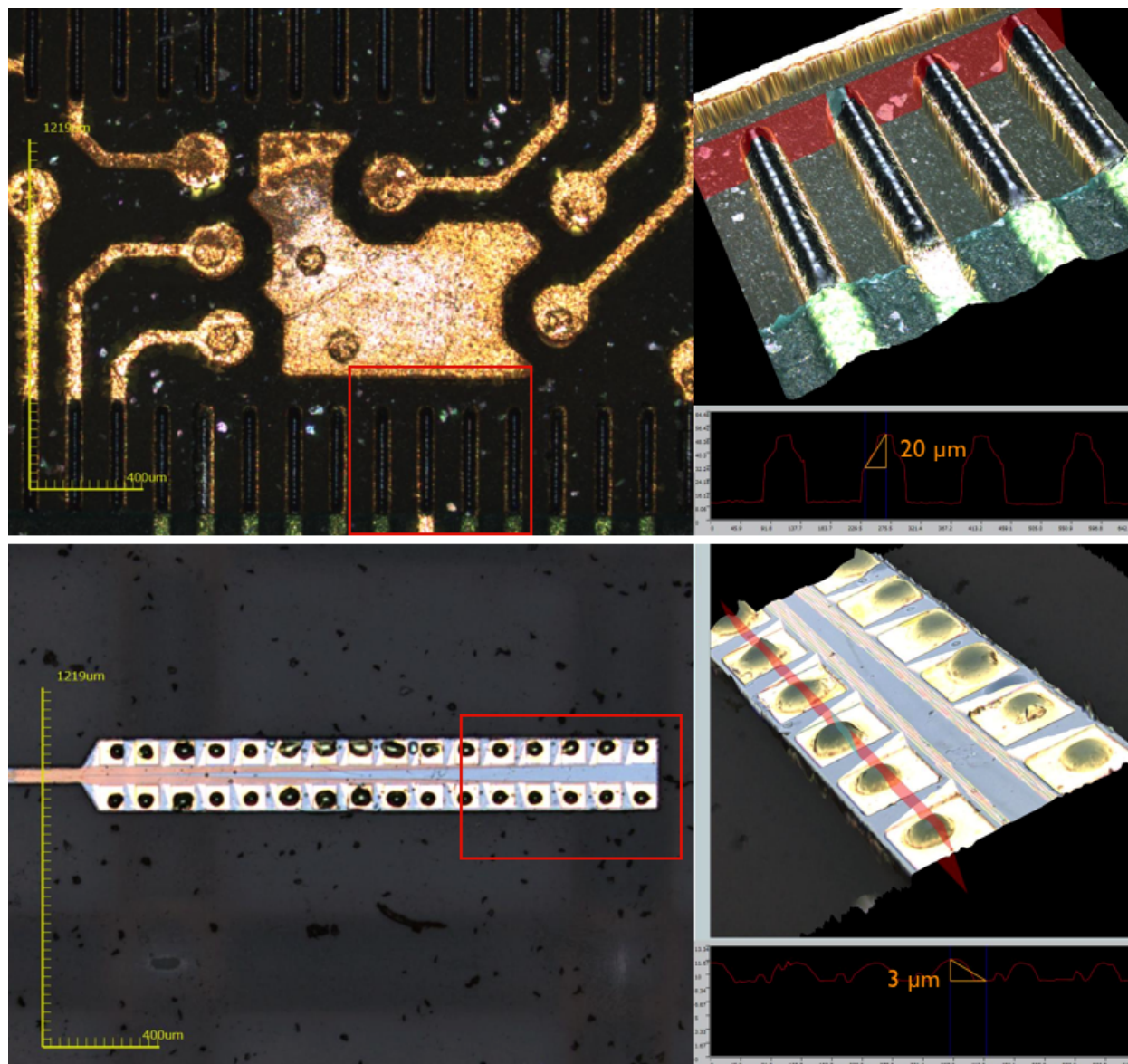


Figure 4.5: PEDOT:PSS:D-Sorbitol printed on bond pad arrays. Top: 20 layers printed sequentially onto PCB, close-up of red box and optical profilometry results shown on the right. Bottom: 3 layers printed sequentially onto nanoprobe bond pad array, close-up of red box is displayed on the right. The 3D images were taken using an Olympus LEXT laser confocal microscope.

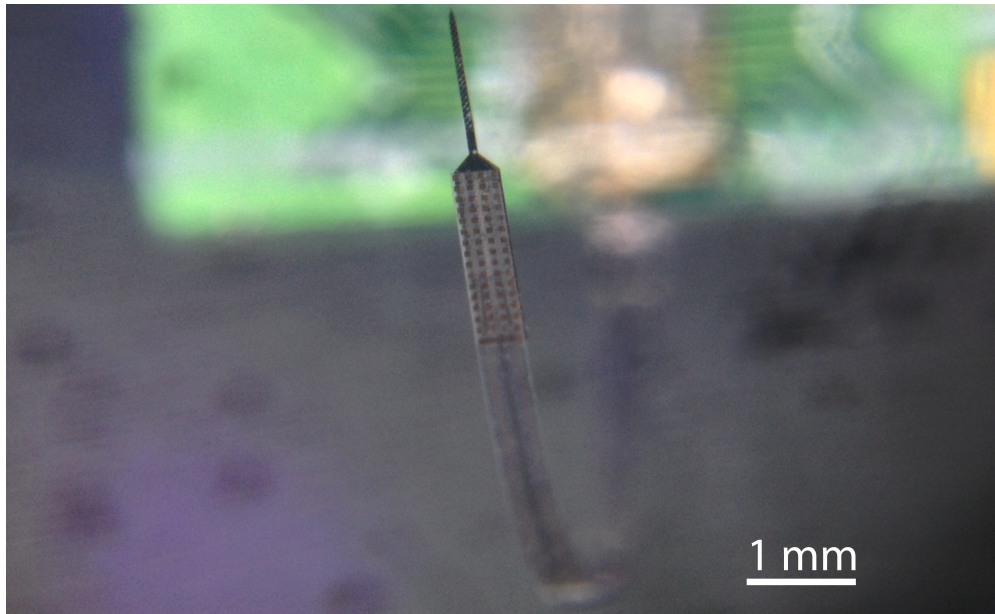


Figure 4.6: 64-channel Nanoprobe CSPT-bonded to Parylene C cable.

hard-to-handle devices. However, it is not without its flaws: alignment of devices under the inkjet printer can be tricky and the sorbitol frequently tends to clog up the nozzle, which can lead to a non-uniform thickness of the adhesive bumps, or if undiscovered, even to shorts between the bond pads through randomly sputtered conductive ink bridges.

Chapter 5

Post-fabrication modifications

5.1 High-temperature annealing of Parylene C devices in inert atmosphere boosts life-time

Wen et al. demonstrated that a high-temperature anneal of Parylene-encapsulated metal in a nitrogen atmosphere can significantly improve device lifetime [95,96]. During the anneal, we placed Parylene devices between two highly polished stainless steel blocks coated with Liquid Wrench Silicone Spray to prevent adhesion between the steel and Parylene C. This block was transferred to a vacuum oven at 200 °C and allowed to anneal for 48 hours under nitrogen back-flow (to prevent oxidative degradation of Parylene). The stainless steel block (with cables) was then removed once the oven had cooled down to 100 °C, and allowed to cool to room temperature. The block was submerged in isopropyl alcohol (IPA) in order to gently release the cables. The slow cool-down was essential to avoid excessive thermal stress in the devices.

To assess the effective lifetime of our Parylene C devices, we performed high temperature soak tests at 85 °C and 95 °C in calcium- and magnesium-free Dulbecco's Phosphate Buffered Saline (DPBS) for one week. DPBS is closer in composition to cerebrospinal fluid (CSF) than pure isotonic saline solution that is often used in lifetime testing experiments while maintaining a constant pH due to phosphate buffering. The absence of calcium and magnesium prevents phosphate or carbonate precipitation at elevated temperatures. During the soak test, we measured electrochemical impedance at 1kHz every 5 minutes. We defined lead failure as a significant increase ($> 1M\Omega$) in electrochemical impedance measured at 1 kHz using an impedance analyzer (nanoZ 1.2, White Matter, LLC). A sharp rise in impedance indicated an open circuit due to conductor cracking or dissolution. Conversely, a sudden decrease in impedance, especially when coupled with equalization of impedance magnitude and phase across several leads, was interpreted as delamination or short. Our lifetime estimation at body temperature (37°C) is based on the Eyring-Polanyi equation 5.1 from transition state theory:

$$k = \kappa \frac{k_B T}{h} \exp\left(-\frac{\Delta A^\ddagger}{RT}\right) \quad (5.1)$$

where k is the rate constant of the degradation reaction, ΔA^\ddagger is the Helmholtz free activation energy for the degradation reaction, T is the absolute temperature, R is the ideal gas constant, k_B is Boltzmann's constant, h is Planck's constant, and κ denotes the transmission coefficient (the probability that the activated complex transitions into the product state). The transmission coefficient is traditionally assumed to be equal to 1 for most processes in polymers where the molecular masses are much greater than the electron mass and the temperatures are far above absolute zero [67]. Typically, the Gibbs free activation energy ($\Delta G^\ddagger = \Delta H^\ddagger - T\Delta S^\ddagger$, where ΔH^\ddagger is the activation enthalpy and ΔS^\ddagger denotes the activation entropy) appears in the Eyring-Polanyi equation, which is appropriate for reactions performed at constant temperature and pressure. Since our test container was sealed in order to prevent evaporation, the test was effectively performed at constant volume and pressure such that using the Helmholtz free energy ($\Delta A^\ddagger = \Delta U^\ddagger - T\Delta S^\ddagger$, where ΔU^\ddagger denotes the activation inner energy) was more appropriate. Under the assumption that the decay follows first order kinetics (i.e. is a Poisson process), the half-life time of an electrode ensemble is related to the decay rate constant by $t_{\frac{1}{2}} = \frac{\ln(2)}{k}$. We estimated the half life time by the mean time to failure (MTTF) on a per-electrode basis at elevated temperature (Fig. 5.1). We computed the Helmholtz activation energy using

$$\Delta A^\ddagger = -RT \ln\left(\frac{\ln(2)h}{k_B T \cdot MTTF(T)}\right). \quad (5.2)$$

Annealed cables survived longer than one week at 85 °C and 95 °C. Thus, by making the conservative assumption that all channels on the annealed cable would have failed immediately after the 95 °C soak test was aborted (i.e. $MTTF = 7$ days), we obtained a lower bound for the Helmholtz free activation energy of failure for the annealed cable. The lifetime at physiological temperature (37°C, 310 K) was estimated using

$$MTTF(T = 300K) = \frac{\ln(2)h}{k_B T} \cdot \exp\left(\frac{\Delta A^\ddagger}{RT}\right). \quad (5.3)$$

The soak temperatures, observed $MTTF$ s, activation energy estimates and projected half-lives at physiological temperature (37° C) are summarized in Table 5.1. The text of this section has been modified from [90] with permission; ©IEEE 2013.

5.2 Platinum black lowers electrode impedance

A passive neural interface, modeled as an ideally polarizable electrode, corrupts the acquired signals of neural origin with thermal voltage noise (Johnson-Nyquist) [68, 122]. The square of that noise \bar{V}_{noise}^2 is proportional to the real part of the electrode impedance $\Re(Z(f))$ [91]:

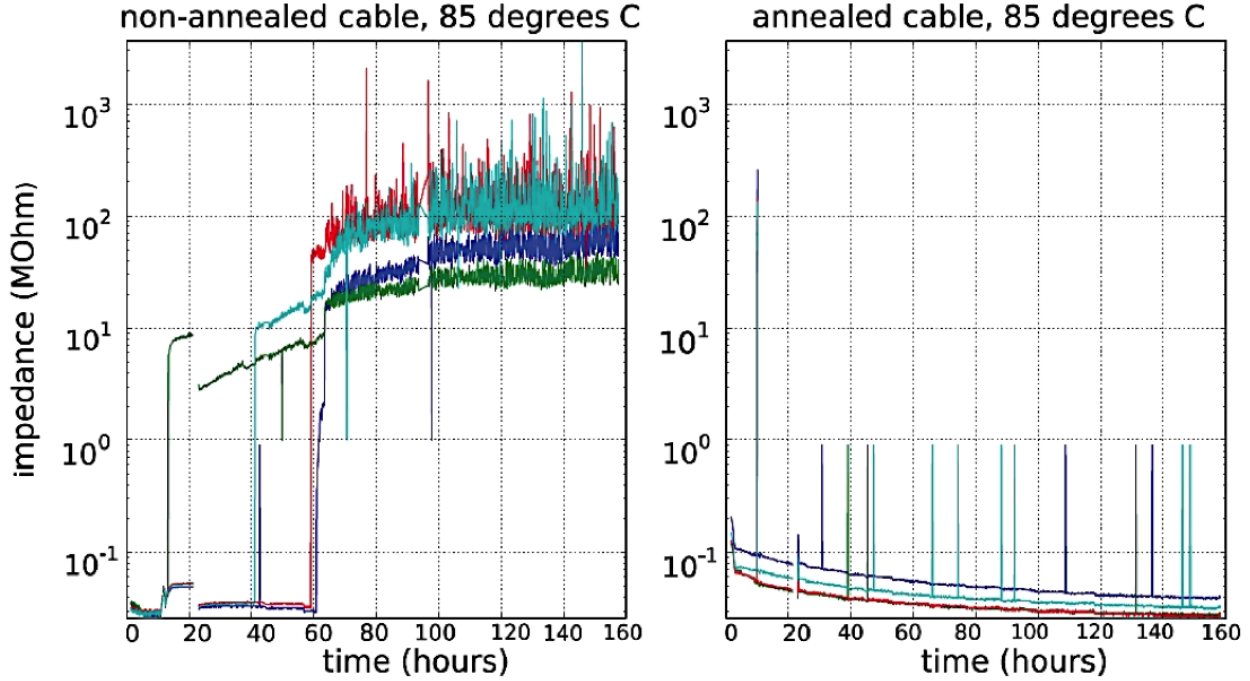


Figure 5.1: Accelerated lifetime testing at 85°C in DPBS. Individual lead impedances at 1 kHz are shown as a function of soak time for two cables (without nanoprobe). (a) Non-annealed cable: representative impedance time course for four channels, which fail catastrophically after 12-60 hours ($MTTF = 43$ h). (b) Annealed cable: the impedances decreased slightly over time, however no failures occurred within the one-week soak period. This figure and caption have been reproduced from [90] with permission; ©IEEE 2013.

Table 5.1: Accelerated lifetime test parameters for non-annealed and annealed cables. This table has been reproduced from [90] with permission; ©IEEE 2013.

	T [°C]	$MTTF(85^\circ\text{C})$ [h]	ΔA^\ddagger [$\frac{\text{kJ}}{\text{mol}}$]	$MTTF(85^\circ\text{C})$ [yr]
non-annealed cable	85	43	125	3.94
annealed cable	95	> 168	> 133	> 74.5

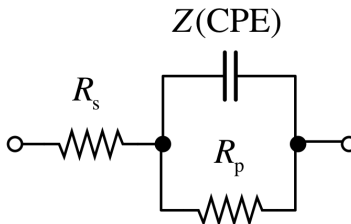


Figure 5.2: Randles Cell [138] equivalent circuit of the electrode-electrolyte interface.

$$\bar{V}_{noise}^2 = 4k_B T \int_B \Re(Z(f)) df \quad (5.4)$$

In equation 5.4 k_B is Boltzmann's constant, T is the absolute temperature, f is the frequency and B is the bandwidth of interest (typically 0.1 Hz - 1 kHz for μ ECoG). In order to reduce the noise associated with the the small geometric area of our microelectrodes, we have increased the electrochemically available electrode area by plating each electrode with highly platinum black, a rough and porous high-surface-area form of platinum [139]. Platinum black was electrochemically deposited according to the reaction equation 5.5:



from a solution of hexachloroplatinate (Thermo Electron Corporation, Orion 010010).

The electrode/electrolyte interface in neurophysiological recordings is commonly modeled [100] by a Randles Cell [138] equivalent circuit (see Fig. 5.2). The capacitive component in this circuit is not an ideal capacitor but a Constant Phase Element (CPE) whose impedance follows a power law given by equation 5.6. The properties of the ionic double-layer at the electrode-electrolyte interface are not purely capacitive due to the fractal nature of the electrode surface [114]. The exponent n in the expression for Z_{CPE} is related to the fractal dimension of the electrode surface D by $n = \frac{1}{D-1}$. Since in general $D \neq 2$ and $n \neq 1$, the CPE contributes a frequency-dependent real resistance component to the total impedance, shown in equation 5.7 by splitting the complex admittance of the CPE ($Y_{CPE} = \frac{1}{Z_{CPE}}$) into its real and imaginary parts. Neural recording electrodes typically encounter potentials < 1 mV, which are far too small to produce Faradaic currents across the electrode-electrolyte interface (i.e. redox reactions at the electrode), so that all currents are essentially displacement currents across the ionic double layer at the electrode-electrolyte interface, which means that μ ECoG electrodes are well-approximated as ideally polarizable electrodes [56]. Since typically for such microelectrodes, the charge transfer resistance R_p across the electrode-electrolyte interface is large ($> 100M\Omega$) we can approximate it as infinite (i.e. an open circuit). Under this approximation, the total impedance of the μ ECoG electrode is given by equation 5.8, which is shown split into its real and imaginary components in equation

5.9. Substitution of equations 5.9 into equation 5.4 yields an expression for the integrated noise power spectral density (NPSD) over the bandwidth of interest B (equation 5.12). As the motivated reader can easily infer from these equations, in order to minimize thermal electrode noise, one needs to lower the real part of the impedance, which can be achieved by lowering R_s , increasing P or increasing n .

$$Z_{CPE} = \frac{1}{Y_{CPE}} = \frac{1}{P(j\omega)^n} \quad (5.6)$$

$$Y_{CPE} = P(j\omega)^n = P\omega^n e^{jn \cdot \frac{\pi}{2}} = P\omega^n \cos\left(n \cdot \frac{\pi}{2}\right) + jP\omega^n \sin\left(n \cdot \frac{\pi}{2}\right) \quad (5.7)$$

$$Z = R_s + Z_{CPE} = R_s + \frac{1}{P\omega^n e^{jn \cdot \frac{\pi}{2}}} = R_s + \frac{e^{-jn \cdot \frac{\pi}{2}}}{P\omega^n} \quad (5.8)$$

$$= R_s + \underbrace{\frac{\cos\left(n \cdot \frac{\pi}{2}\right)}{P\omega^n}}_{real} - j \cdot \underbrace{\frac{\sin\left(n \cdot \frac{\pi}{2}\right)}{P\omega^n}}_{imaginary}, \quad \text{with } \omega = 2\pi f \quad (5.9)$$

$$\Rightarrow \bar{V}_{noise}^2 = 4k_b T \Re(Z(f)) \delta f = 4k_b T \cdot \left(R_s + \frac{\cos\left(n \cdot \frac{\pi}{2}\right)}{P(2\pi f)^n} \right) \cdot \delta f \quad (5.10)$$

$$\Rightarrow \bar{V}_{int,noise}^2 = 4k_b T \int_B \Re(Z(\omega)) \frac{d\omega}{2\pi} = 4k_b T \cdot \int_B \left(R_s + \frac{\cos\left(n \cdot \frac{\pi}{2}\right)}{P(2\pi f)^n} \right) df \quad (5.11)$$

$$(5.12)$$

Fig. 5.3 shows non-linear fits of measured impedance spectra to the above model (equation 5.8) before and after plating using EIS Analyser [16]. The fit parameters show that platinum black deposition lowers the real part of the electrode impedance by simultaneously lowering R_s , increasing P , and increasing n . It is worth noting that while the surface of the platinum electrode looks rough and black after electroplating (Fig. 5.5, left), which accounts for the increase in P , the electrode surface actually appears to become *less* fractal (n closet to 1).

Fig. 5.4 shows an analytical plot of equation 5.11 and the integrated noise power over the bandwidth of interest for μ ECoG (0.1Hz - 1000 Hz) predicted from equation 5.11 based on the model parameters fit in Fig. 5.3. Since thermal noise grows like the square root of the real part of the impedance, a 2-3 order of magnitude decrease in impedance resulted in a factor $10\times$ decrease in expected noise contribution (from $5.6 \mu\text{V}$ to $0.55 \mu\text{V}$) from the electrodes. This improvement took the electrode noise below the input-referred noise of our electrophysiology amplifier, which was $\approx 1\mu\text{V}$.

Plating method

The grid electrodes served as cathodes and were electroplated serially using a nanoZ (White Matter, LLC) in galvanostatic mode for 45 s. The current was limited to -500 nA

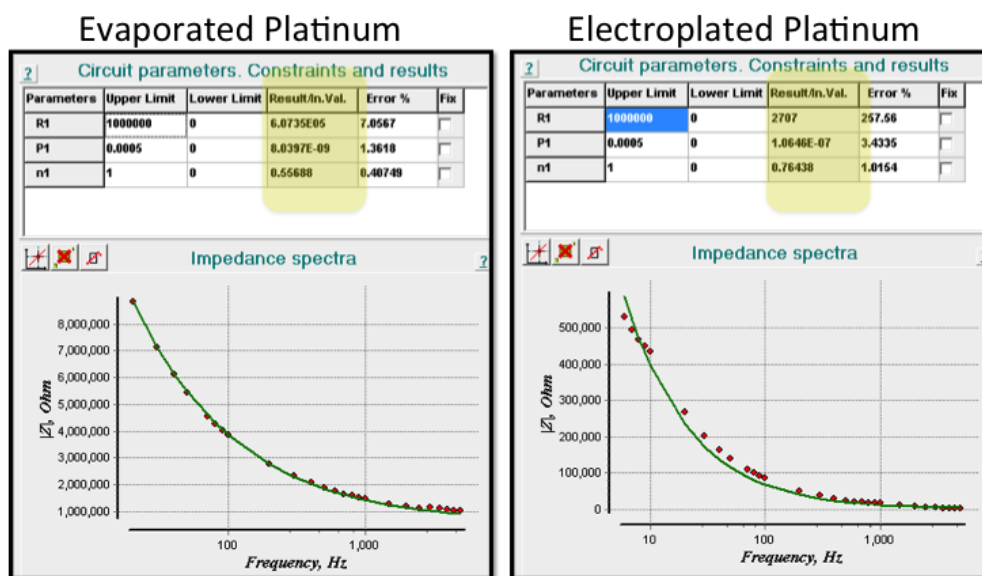


Figure 5.3: Screen shot from the fitting interface of EIS Analyser [16]. Left: nonlinear fit of electrochemical impedance spectrum (EIS) before electroplating of platinum black. Right: nonlinear fit of EIS after plating. The yellow box highlights the change in fitting parameters, which are responsible for the 2-3 orders of magnitude decrease in impedance.

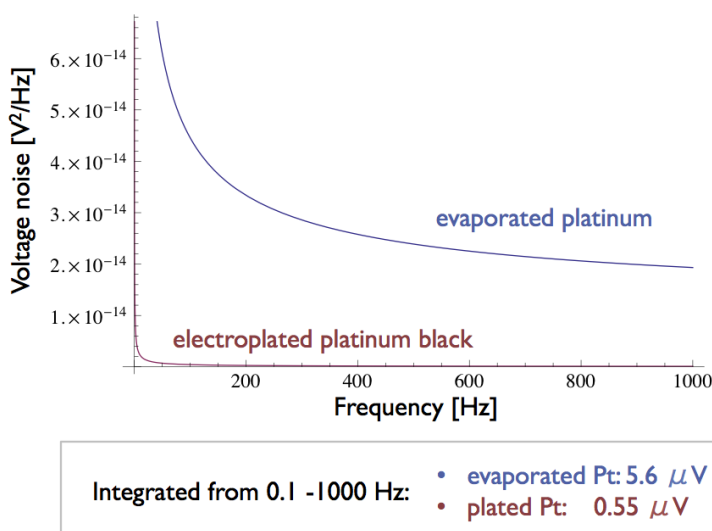


Figure 5.4: Expected noise spectral density and integrated noise power over the bandwidth of interest for ECoG for electrodes before and after surface-modification with platinum black.

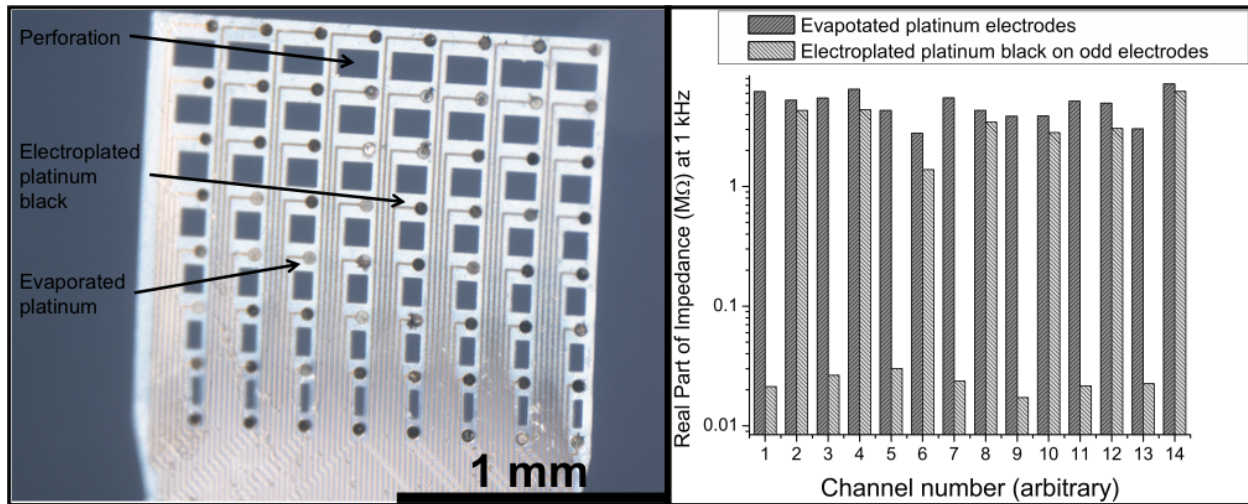


Figure 5.5: Left: Optical micrograph of 64-channel, high-density μ ECoG: The device featured 200 μm electrode pitch, 40 μm electrode diameter and 10 μm minimum feature size (trace/space). Some of the displayed electrodes (gray) consisted of smooth and highly reflective, evaporated platinum. The black electrodes were electrochemically plated with platinum black, a porous form of platinum that increased the effective electrochemically available area and decreases electrode impedance. Perforations in the Parylene, increase the arrays mechanical compliance and allow vascularization through the array [148]. Right: Impedances of plated vs. non-plated electrodes: The dark gray bars show the real part of the impedance for 14 evaporated platinum electrodes. The light gray bars show impedances of the same electrodes after every odd-numbered electrode was direct current (DC) plated with platinum black for 45 s at a current of $-0.5 \mu\text{A}$. Note the logarithmic resistance scale: platinum black deposition reduced the electrode impedance by more than two orders of magnitude. This figure and caption have been modified from [88] with permission; ©IEEE 2013.

(i.e. μ ECoG electrode acting as the cathode, Pt/Ir wire acting as the anode) for round electrodes 40 μm in diameter, which corresponds to a current density of $\approx 400 \frac{\text{A}}{\text{m}^2}$. We were able to decrease the electrode impedance by more than two orders of magnitude compared to evaporated platinum. A comparison between the resistive impedance of plated and non-plated electrodes (measured when immersed in phosphate-buffered saline (PBS) at 1kHz using the nanoZ), is shown in Fig. 5.5. The text in this section has been modified from [88] with permission; ©IEEE 2013.

Chapter 6

A Transparent μ ECoG Array

6.1 Introduction

State of the art tools for simultaneous optogenetic stimulation and electrophysiological recordings, such as optrodes [55], are invasive and can cover only a very small fraction of the cortex with relatively few stimulation and recording sites. In this chapter, we present an optically transparent μ ECoG array, which allows optical stimulation of and optical recording from neural tissue immediately beneath the array (Fig. 6.1). The text in this chapter has been modified from [89] with permission; ©IEEE 2011.

Neural recordings constitute only part of a larger tool kit required to reverse engineer the brain (i.e. to understand its normal or pathological dynamics as properties of underlying neural circuits). Ideally, it is also desirable to be able to write information into neural circuits and to study how this information is transformed in the brain. A specific example of this can be useful in BMI for motor control: successful motor control is highly dependent on proper sensory feedback. In this context, it is essential to close the motor-sensory feedback loop (for example, to integrate a prosthetic limb into a patients proprioception) and this requires information write-in [123].

Neurons can be stimulated electrically but with poor spatial resolution, and stimulation artifacts render simultaneous electrophysiological recordings at the same site very difficult. Boyden and Deisseroth recently demonstrated that neurons can be rendered sensitive to stimulation by light [18]. Neurons transfected with a light-sensitive ion channel, such as channelrhodopsin, bacteriorhodopsin and halorhodopsin, can be individually modulated to either fire or suppress action potentials when illuminated at the correct wavelength. Integration of this powerful new stimulation approach with μ ECoG requires the development of a transparent, flexible, and biocompatible electrode array. The fabrication of flexible transparent electrodes has to date been mainly developed for light-emitting diodes (LEDs), flexible displays and solar cells. Several materials and deposition methods have been investigated to achieve the best tradeoff between transparency and conductivity. Transparent conductive oxides (TCOs) such as indium tin oxide (ITO) can be found in numerous industrial

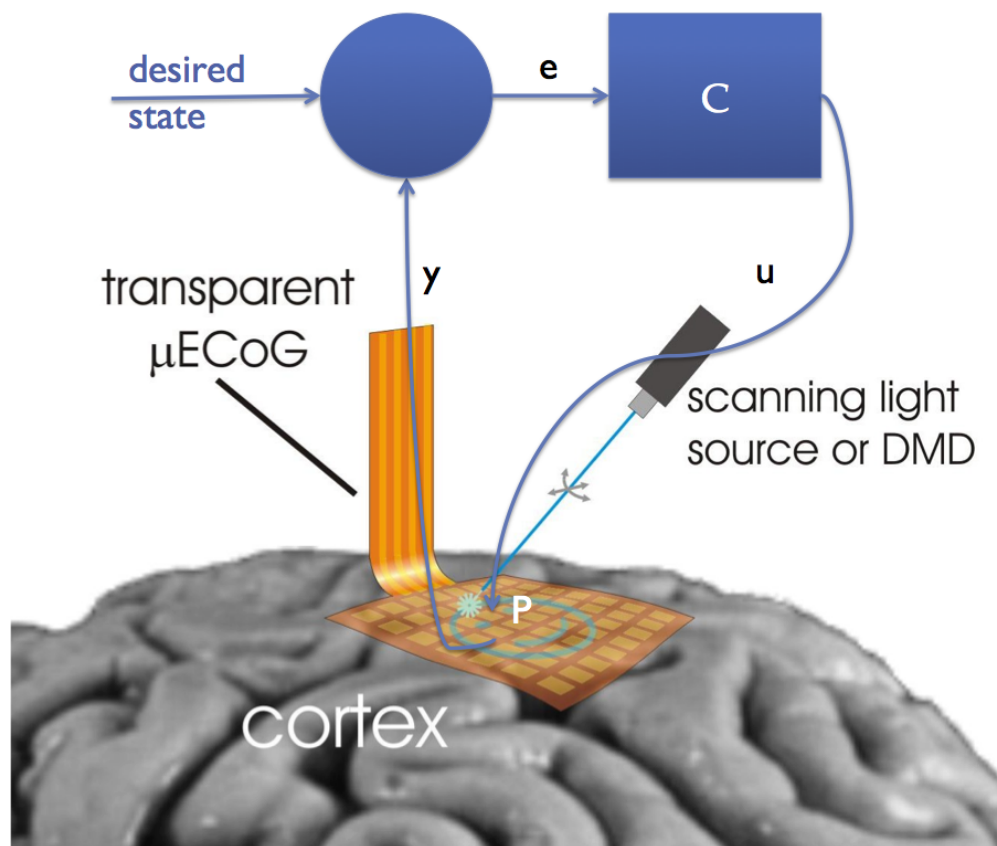


Figure 6.1: Integration of μ ECoG with optogenetics. Patterned light, e.g. from a Digital Micromirror Device (DMD), excites transfected or transgenic neural tissue underneath a transparent μ ECoG array. Electrical activity detected by the μ ECoG could be feedback-coupled with the light-source output to control activation states on the cerebral cortex. This figure and caption have been modified from [89] with permission; ©IEEE 2011.

applications due to their high electrical conductivity and transparency over the entire visible spectrum [168]. However, ITO is a relatively brittle ceramic material and thus it is considered suboptimal for flexible electrodes [15]. While alternatives such as single-walled carbon nanotube percolation networks [5], silver nanowire percolation networks [34] and graphene layers [177] are being investigated, ITO is a material with superior conductivity, transparency and biocompatibility [154], and is easily sputtered and patterned lithographically. Making use of these advantages, we fabricated an ECoG array using ITO as the conductor for all electrodes in the array but unfortunately the large bond pads fractured along stress lines at the edge of plasma-etched vias (Fig. 6.2). Interestingly, ITO microelectrode pads and buried traces remained intact. We successfully mitigated the brittleness of ITO by confining it to the microelectrodes and to short pieces of buried interconnect traces only, while the long

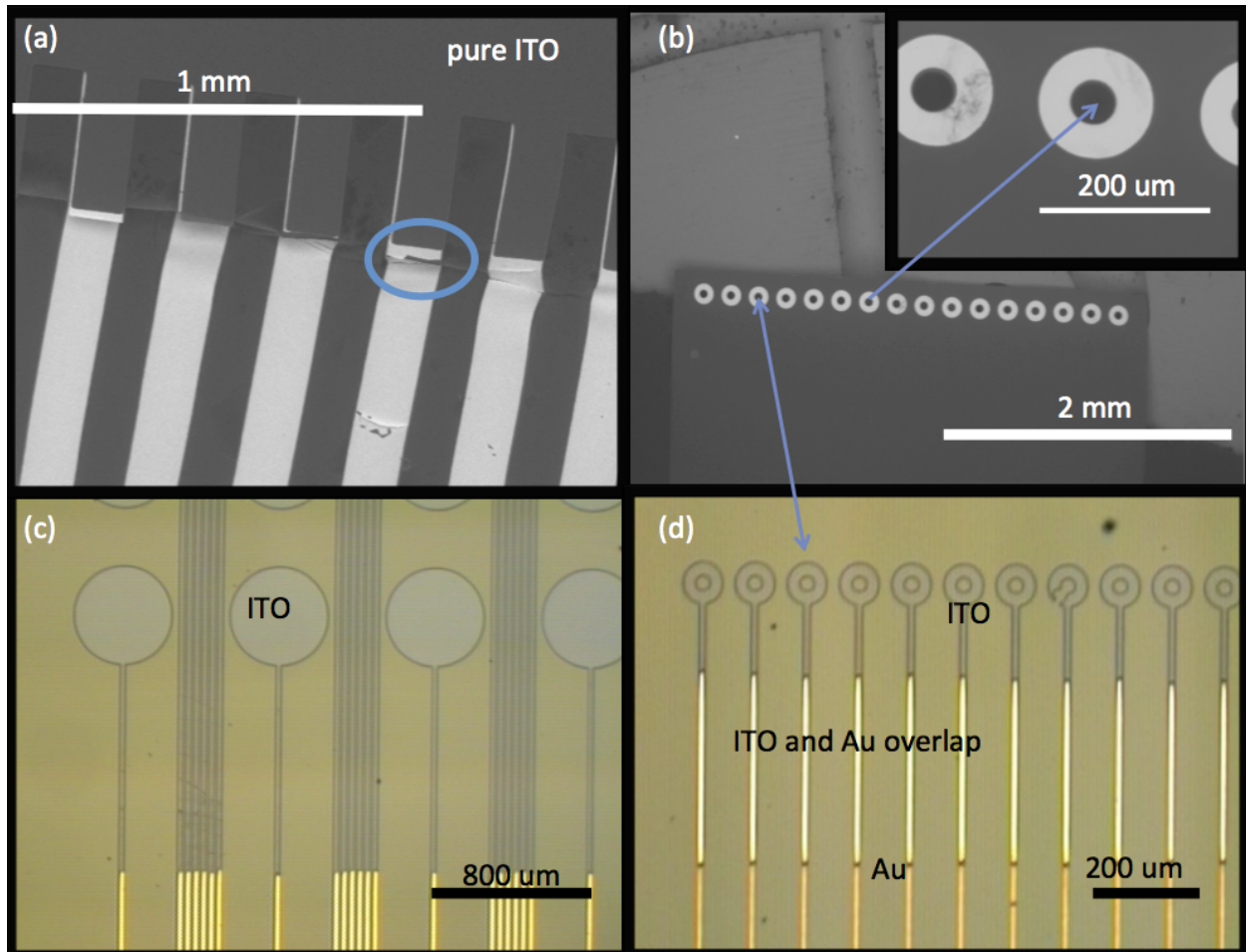


Figure 6.2: Micrographs and SEM images of the 16-channel and 49-channel devices. (a) Bond pad damage on ITO-only devices. (b) Intact electrodes of a 16-channel ITO device. (c) Electrodes and interconnects of a 49-channel Au-ITO hybrid device. (d) 16-channel hybrid array. The ring-shaped electrodes are made of ITO. The light-yellow lines indicate the overlap of Au and ITO. The lower portion of the connections (orange) consists of Cr/Au. This figure and caption have been reproduced from [89] with permission; ©IEEE 2011.

interconnect traces and bonding pads were fabricated using ductile high-conductivity gold.

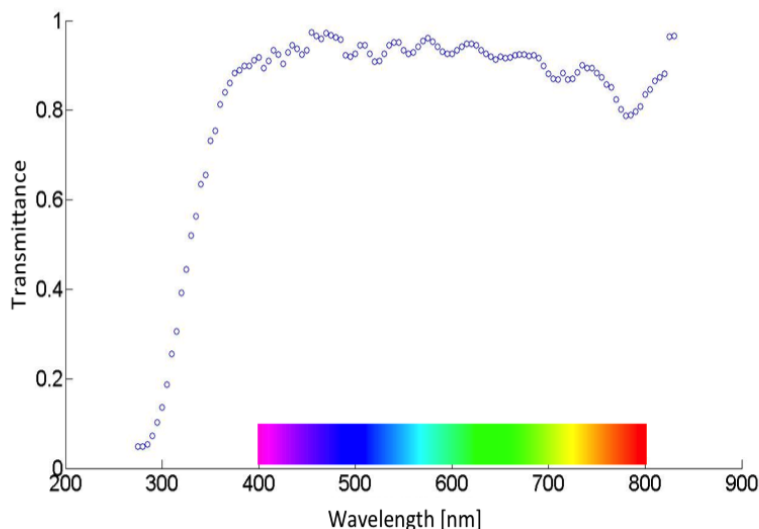


Figure 6.3: Transmittance of the 110 nm thin ITO film is shown as a function of wavelength (285 nm to 830 nm). This figure and caption have been modified from [89] with permission; ©IEEE 2011.

6.2 Results

Optical Properties of ITO μ ECoG

Transparency was measured using an ellipsometer/spectrometer (Sopra GESp) under normal incidence. The transmittance, normalized with respect to the substrate, exceeded 90% over most of the visible spectrum as shown in Fig. 6.3.

ITO shows no photoelectric artifact under visible illumination

Illumination of metal or silicon electrodes during electrophysiological recordings leads to high amplitude light-induced artifacts that can be photoelectric or photoelectrochemical [74] in nature. The conductivity of indium tin oxide is mediated by mobile oxygen vacancies and its transparency is due to a large band gap (2.6 eV to 3.65 eV, depending on stoichiometry) [113] such that ITO electrodes show no photoelectric effect when illuminated with visible light as shown in Fig. 6.4 and thus help reduce artifacts in electrophysiological recordings.

Electrical Characterisation

The sheet resistance of the ITO was measured as $43.7 \frac{\Omega}{\square}$ in a 4-point-probe (VEECO FPP-5000) measurement. The resistivity was calculated to be $4.807 \cdot 10^{-6} \Omega\text{m}$. ITO traces in our

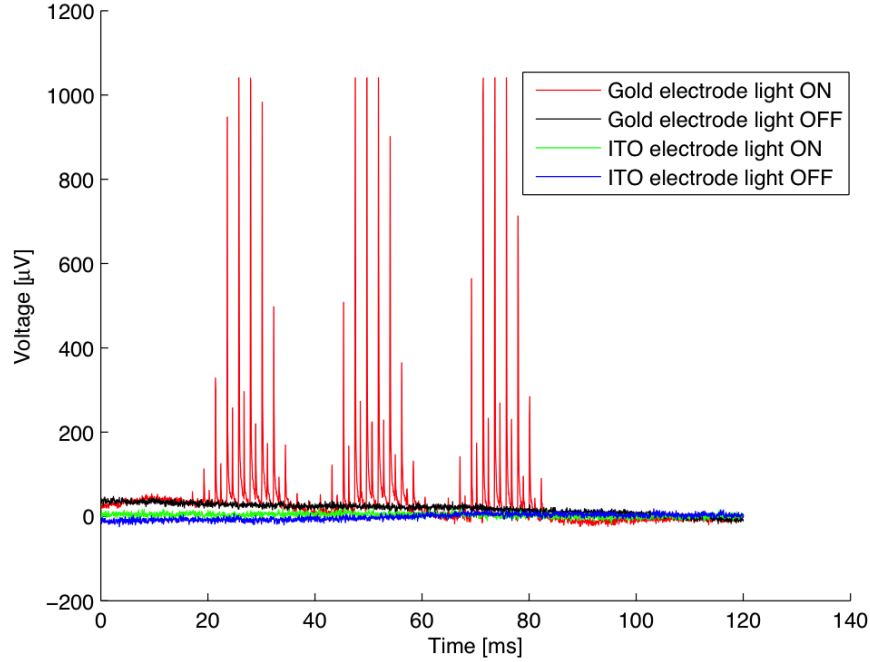


Figure 6.4: ITO and gold electrodes illuminated using a laser scanning microscope. While the gold electrode shows pronounced photoelectric spikes, no such artifact can be seen on the ITO electrodes.

design are between 1 mm and 6.5 mm in length. Thus, from device geometry, we expected a series resistance between 2.2 $k\Omega$ and 14.2 $k\Omega$ for each electrode. We characterized the electrode-electrolyte interface by electrochemical impedance spectroscopy (EIS using nanoZ, White Matter, LLC, frequency sweep: 5 Hz to 5 kHz). The device formed the active electrode and a silver wire formed the reference & counter electrodes. We used artificial cerebrospinal fluid (aCSF, Artificial CSF Perfusion Fluid, Harvard Apparatus, ion concentrations in mM: $[Na^+] = 150$; $[K^+] = 3.0$; $[Ca^{2+}] = 1.4$; $[Mg^{2+}] = 0.8$; $[PO_4^{3-}] = 1.0$; $[Cl^-] = 155$) as the electrolyte. The data were fitted to a Randles Cell model [100,138] (see Fi. 5.2 for equivalent circuit) with impedance given by

$$Z_{total} = R_s + \frac{R_p}{1 + R_p P(j\omega)^n} \quad (6.1)$$

using EIS Spectrum Analyzer [16] to extract the line resistance $R_s = 9.36 \pm 5.53 k\Omega$, charge transfer resistance $R_p = 187.29 \pm 56.17 M\Omega$, and the constant phase element (CPE) parameters $n = 0.87 \pm 0.002$ and $P = 1.58 \pm 0.02 \frac{sn}{\Omega cm^2}$ as demonstrated in Fig. 6.5.

The series resistance value was in good agreement with our predictions. Approximating the CPE with a capacitor, we calculated the capacitance per area of the ITO pads to be $1.39 \pm 0.02 \frac{\mu F}{cm^2}$, which is an order of magnitude lower than that of platinum pads ($60 \frac{\mu F}{cm^2}$) [120].

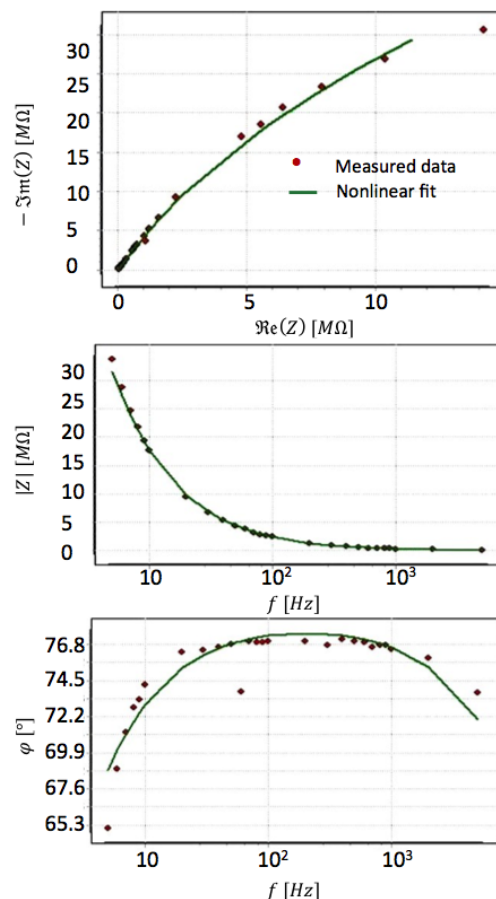


Figure 6.5: Characterization of the electrode-electrolyte interface by electrochemical impedance spectroscopy. The data were adequately fit by the Randles Cell circuit model, see Fig. 5.2. This figure and caption have been modified from [89] with permission; ©IEEE 2011.

The parallel resistance was expected to be very high as all testing was performed at voltages far below electrochemical potentials and no Faradaic charge transfer was expected. We calculated a pad-electrolyte interface resistance of $212 \pm 60 \frac{k\Omega}{cm^2}$, which was similar to values reported for platinum electrodes in literature ($220 \frac{k\Omega}{cm^2}$) [120].

Acute in vivo recording over rat motor cortex

Superficial laser stimulation through a suspended optical fiber (488 nm, 3-18 $\frac{mW}{mm^2}$, 50 Hz pulse frequency, 5 ms pulse width, 1 s duration) of rat motor cortex, transfected using the construct AAV2/1-hSyn-ChR2-YFP, elicited a high frequency neural response recorded by μ ECoG (see Fig. 6.6, right). At a stimulation frequency of 150 Hz, too high for ChR2 to

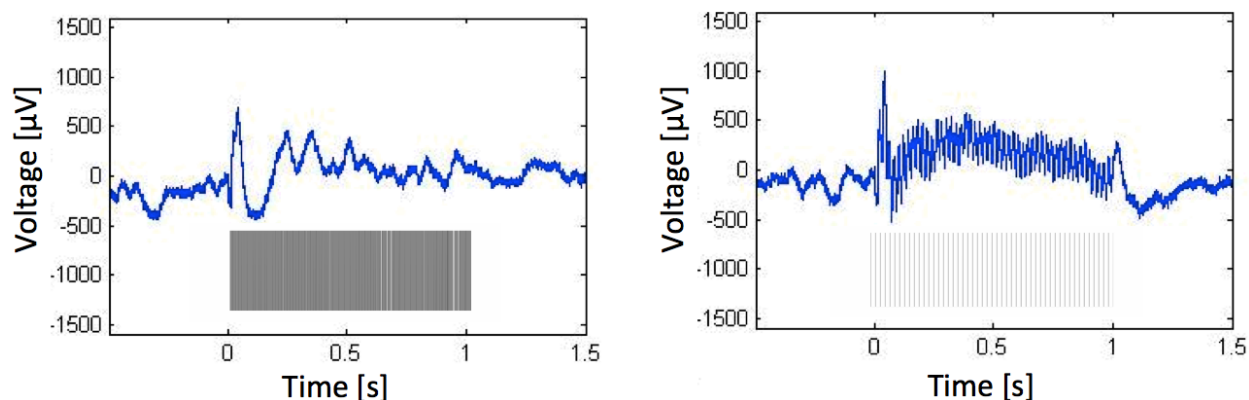


Figure 6.6: Left: Control for photoelectric artifact: at 150 Hz the channelrhodopsin-2 cannot follow and no high frequency response is observed. Right: at 50 Hz the channelrhodopsin-2 follows the laser pulse train and a high frequency neural response is observed in μ ECoG.

follow, only an initial transient but no high frequency response was observed in μ ECoG as shown in Fig. 6.6, left. This control demonstrates that light-induced high-frequency activity is neural in origin rather than a photoelectric or photoelectrochemical artifact.

6.3 Conclusion

Conductive and transparent ITO films were successfully DC-sputtered on Parylene and patterned by lift-off. While ITO on Parylene is quite brittle, our approach successfully combined metal interconnects with ITO microelectrodes, resulting in flexible, transparent hybrid μ ECoGs with good electrical and excellent optical characteristics.

Part III

μ ECoG Applications in Neuroscience

Chapter 7

Functional mapping of auditory cortex

7.1 Introduction

The presence of topographic maps in primary sensory cortices is well established in literature (reviewed in [169], and more recently in [26]) and receptive fields for specific subsets of stimulus parameters can often be found in specific locations of sensory cortices, organised in an orderly fashion. For example, without attempting to provide a comprehensive list of the various known topographic organisations, there is retinotopy in the primary visual cortex (V1) [176], somatotopy in somatosensory cortex [69], and tonotopy in the auditory cortex [151].

The auditory cortex of the rat, for example, can be mapped in great detail by recording the average firing rate of single neurons in response to pure tones varying in amplitude and frequency as a function of electrode location using penetrating tungsten microwire electrodes [135] as shown in Fig. 7.1. Such experiments have demonstrated that while many auditory neurons increase their firing rate in response to very loud stimuli (less specificity), posterior parts of the primary auditory cortex (A1) respond preferentially to lower frequency tones and more anterior A1 responds preferentially to higher pitch for quieter stimuli. It is worth noting that the gold-standard mapping procedure used by Polley et al. [135,136] has several practical disadvantages:

- The entire stimulus set has to be presented with a sufficient number of stimulus repetitions for each set of electrode positions. This is a very slow and laborious process, that can only be performed in acute surgery on an anaesthetised animal and can take anywhere between 12 and 30+ hours depending on the desired mapping resolution and the number of penetration sites mapped simultaneously (typically 1-8).
- Due to the long duration of data acquisition, data may be contaminated by non-stationarities in the overall state of the cortex, i.e. data acquired early in the experiment may not have been acquired under strictly identical conditions compared to data acquired late in the experiment.

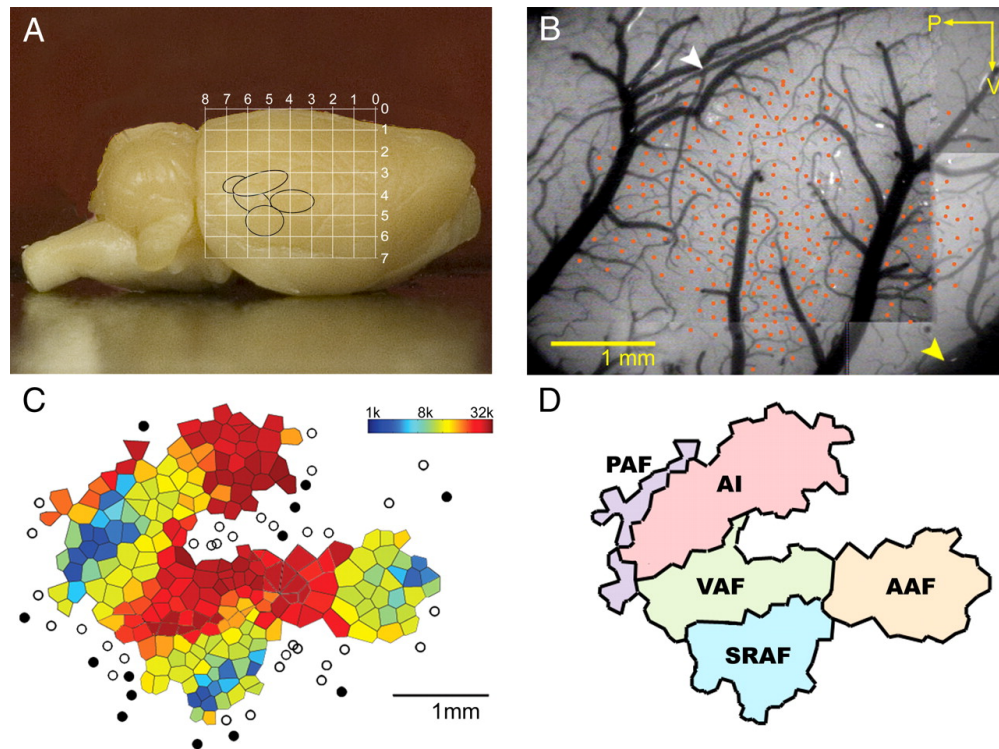


Figure 7.1: Tonotopic organization of multiple fields within the rat auditory cortex. A: an 8×7 -mm grid is superimposed onto a lateral view of the right hemisphere of the rat brain. Numeric values denote distance with respect to bregma (0, 0). Five black ellipses are superimposed onto the temporal cortex to represent the typical position and shape of the 5 cortical auditory fields described in this figure. B: location of 276 separate microelectrode penetrations (orange dots) are shown in reference to the surface vasculature of the right temporal cortex. Yellow arrowhead identifies the rhinal vein. White arrowhead identifies the middle cerebral artery. P and V indicate posterior and ventral, respectively. Scale bar = 1 mm. C: tessellated Voronoi map is constructed such that the polygon color represents the characteristic frequency (CF) associated with neurons located in the middle cortical layers at that position in the map and the polygon area is proportional to the distance separating neighboring penetrations. Filled circles indicate unresponsive sites. Open circles represent sites with sound-driven responses for which a CF could not be defined. D: schematic drawing of the relative position of 5 tonotopically organized auditory cortical fields. Borders between fields were defined by reversals or shifts in the CF gradients. PAF, posterior auditory field; AI, primary auditory cortex; VAF, ventral auditory field; SRAF, suprarhinal auditory field; AAF, anterior auditory field. Figure and caption reproduced with permission from [135], ©2007 the American Physiological Society.

- The mapping is destructive to the delicate neural tissue. Due to the acute nature of the procedure, mapping cannot be repeated in the same animal before, during, and after training in studies of learning-induced plasticity of tonotopic maps such as [58]. This limits the experimenter to comparing maps before and after training in genetically similar animals, missing out on the opportunity to study the dynamics of plastic reorganization in each individual.

In this chapter we are investigating if high-density μ ECoG can be used for rapid and non-destructive high-resolution mapping of receptive fields in auditory cortex, benchmarked against the gold-standard of intracortical spike recordings.

For the sake of completeness, it is worth noting the auditory cortex can also be mapped quickly and non-destructively using intrinsic optical imaging [71] but this method provides limited spatial resolution, uses an indirect measure of neural activity (blood oxygenation) and is subject to the same type of limitations in temporal resolution that prevent fMRI from resolving fast transient neural responses [101].

7.2 Methods

All animal experiments described in this chapter were performed with approval of the UCSF Animal Care and Use Committee. Most of the surgeries were performed by Kris Bouchard in the laboratory of E. Chang at UCSF.

Rats were anaesthetised with a mix of Ketamine and Xylazine and the head was fixed in place using eye bars. Anesthesia levels were maintained with approximately hourly Ketamine/Xylazine injections at a minimum depth that suppressed the toe-pinch reflex. The animal was supplemented with pure oxygen in order to counteract hypoxic brain edema. Body temperature was controlled using a heating pad in conjunction with a rectal thermocouple.

A large craniectomy and durectomy were performed over the right temporal lobe approximately centered over auditory cortex. A 64-channel Parylene C μ ECoG array (200 μ m electrode pitch, 40 μ m electrode diameter, design shown in Fig. 3.8, right) was placed over auditory cortex. A 32 channel Neuronexus laminar probe (A1x32-Poly3-10mm-50-177) was inserted into one of the perforations in the μ ECoG array to a depth of approximately 600 μ m using a micromanipulator (Fig. 7.2). It is crucial to let the brain settle around the laminar probe for at least 15 minutes before recording in order to ensure that the brain is stationary relative to the probe. A photograph of a representative experimental setup is shown in Fig. 7.3.

Acoustic stimuli (white noise bursts or pure tones), recorded on DVD in pseudo-random order were presented to the animal through a calibrated free-field speaker. Neural data was acquired at a sampling rate of approximately 12 kHz using a commercial head stage (ZC64), pre-amp (PZ2) and data processor (RZ2), all purchased from Tucker-Davis-Technologies (TDT). Mathworks Matlab and Adobe Illustrator were used for data analysis, plotting, and visualization.

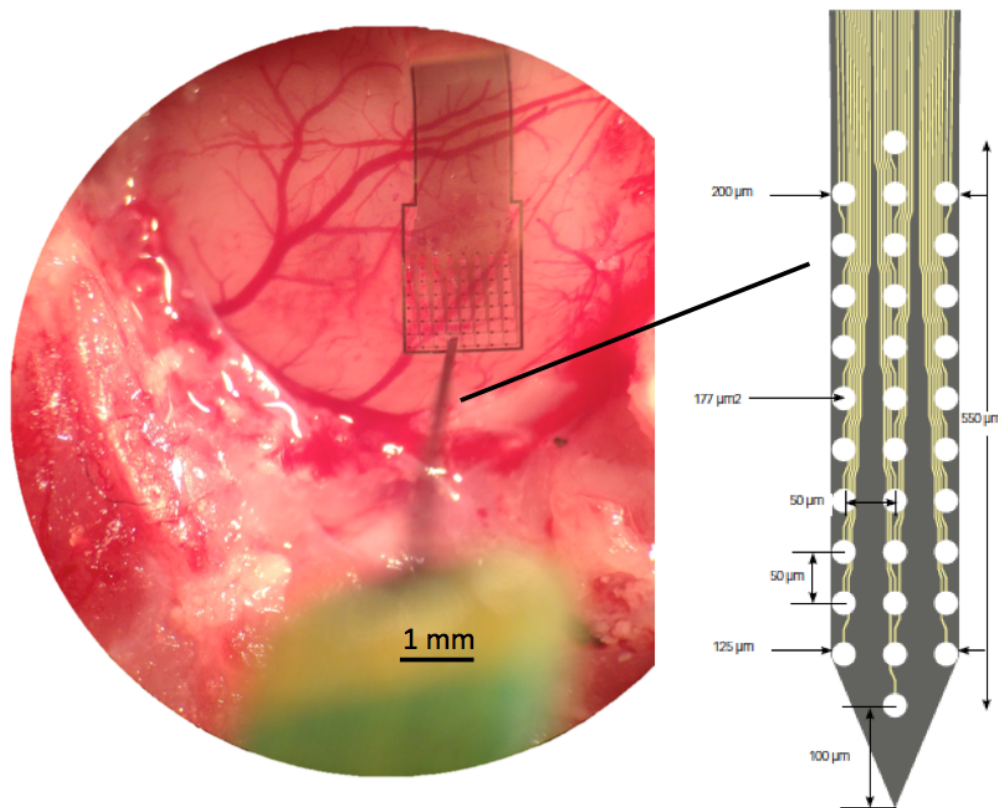


Figure 7.2: Left: micrograph of 64-channel μ ECoG with 32-channel laminar probe (NeuroNexus A1x32-Poly3-10mm-50-177) inserted through one of the etched perforations. Right: layout of the A1x32-Poly3-10mm-50-177 laminar probe. Image credit: NeuroNexus Technologies, Inc.

Common Average Referencing

All signal was initially recorded with respect to ground in the form of a silver or platinum-iridium wire inserted into moisturized muscle near the craniectomy. Before amplitude-frequency decomposition, the time-domain signal was common-average referenced in order to remove noise and artifacts introduced by electromagnetic interference or bioelectric phenomena not originating in the brain (e.g. muscle activity picked up by the reference) common to most electrodes. In order to ensure that only noise is subtracted from electrodes that is actually present, not the common average per se was subtracted but rather each electrode's projection onto the normalized common average. For the potential time series $|x_i\rangle$ on the

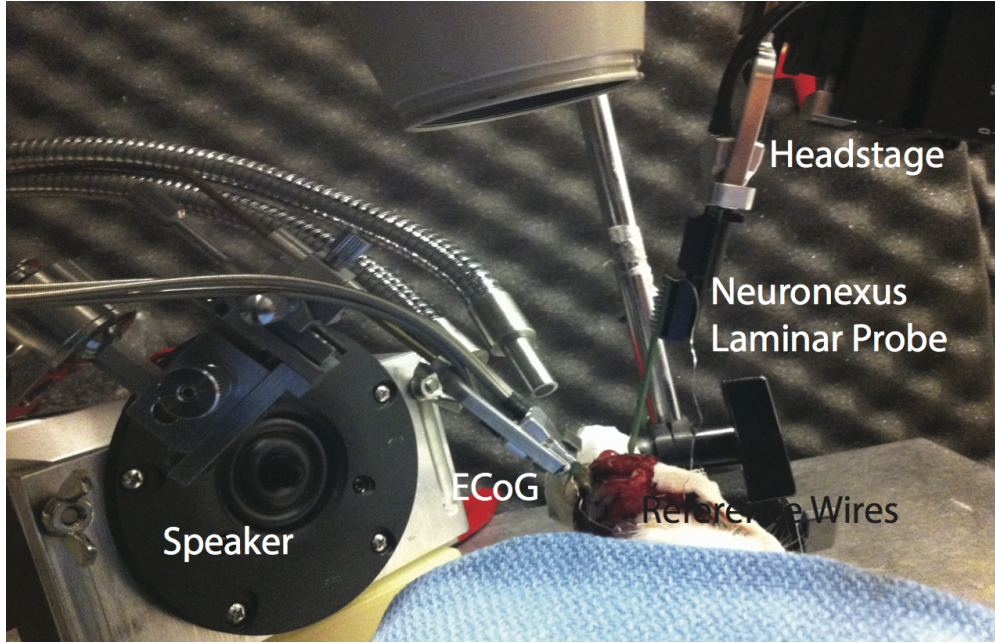


Figure 7.3: Representative photograph of the surgical setup. A 64-channel Parylene C μ ECoG array (200 μ m electrode pitch, 40 μ m electrode diameter) was placed over auditory cortex and a 32 channel Neuronexus laminar probe (A1x32-Poly3-10mm-50-177) was inserted into one of the perforations in the μ ECoG array to a depth of approximately 600 μ m using a micromanipulator. Image credit: Kris Bouchard.

i -th channel (out of N channels) the common average reference was computed according to

$$|CAR\rangle = \frac{1}{N} \sum_{i=1}^n |x_i\rangle \quad (7.1)$$

The re-referenced potential time series x_i^r was computed according to

$$|x_i^r\rangle = |x_i\rangle - \langle \frac{CAR}{|CAR|} |x_i\rangle | \frac{CAR}{|CAR|} \rangle. \quad (7.2)$$

Above we made use of the bra-ket notation where $|\rangle$ denotes a column vector, $\langle|$ is the transpose of $|\rangle$ and denotes a row vector, and $\langle| \rangle$ is the scalar product.

Constant Q Transform

Amplitude-frequency decomposition of neural data can be performed using a plethora of different techniques such as short-time First Fourier Transform (SFFT) [59], the Hilbert-Huang Transform [27, 43, 66] and an entire family of wavelet techniques [171]. In the work

described in this chapter we use a computationally efficient algorithm to perform a constant-Q transform (CQT) as described and implemented in the Matlab toolbox by Schörkhuber and Klapuri [150]. The term constant-Q refers to the fact that the CQT transform decomposes the time-domain signal into complex-valued time-frequency atoms in such a way that the Q-factor of each bin, defined as

$$Q \equiv \frac{f_k}{\Delta f_k}, \quad (7.3)$$

where f is the center-frequency of the bin and Δf_k is the -3 dB bandwidth of the time-frequency atom, remains constant. In essence, the CQT is a wavelet transform that transforms a signal from the time-domain into the time-frequency domain in such a way that the center frequencies of the frequency bins are geometrically spaced, i.e. the frequency resolution is better for low frequencies and the time-resolution is better for higher frequencies. The CQT transform was performed across the frequency range between 3 Hz and 1500 Hz, covering 9 octaves with 6 bins per octave.

7.3 Results

White noise stimuli

Since the location of the craniectomy was determined only approximately using anatomical landmarks, in order to ensure that the μ ECoG array was indeed located over an auditory area, we started each experiment by presenting a set of 60 white noise (WN) bursts (100 ms in duration, 1 Hz burst frequency- i.e. 900 ms inter-stimulus interval - see Fig. 7.4 top). Broadband white noise contains all frequencies audible to the rat, and thus is expected to excite all auditory areas. The silence between the bursts (300-600 ms after stimulus onset) was used to calculate a baseline to which all signal was z-scored. All signal presented in this chapter labeled *Z-Score* is thus given in units of standard deviation of the baseline. I.e. if μ_b and σ_b denote the mean and standard deviation of the baseline, respectively, and x_s is the recorded stimulus response, then the plotted signal is computed according to:

$$|Z\text{-score}\rangle = \frac{|x_s - \mu_b|}{\sigma_b}. \quad (7.4)$$

For spectrograms this Z-scoring is done by frequency bin, which whitens the signal and compensates for the $\frac{1}{f^n}$ power decay in the μ ECoG spectrum.

When positioned correctly, most μ ECoG electrodes recorded robust acoustic evoked potentials similar to the ones shown in 7.4 middle. Note that most of the high- γ (HG) power in the evoked spectrogram (Fig. 7.4 bottom) occurred between the first maximum and minimum of the time-domain evoked potential. Averaging the spectrogram across this time interval yielded Figure 7.5, which shows that on average power in the 70-170 Hz range responds most robustly to the WN stimuli. Fig. 7.5 shows several distinct response peaks:

- around 30 Hz (β , B)

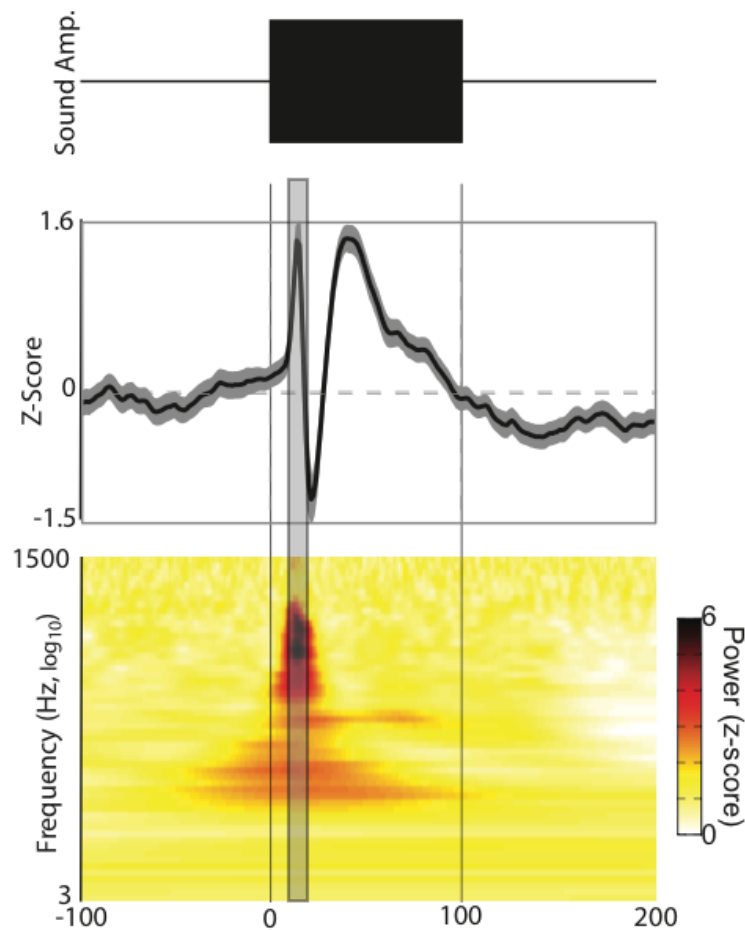


Figure 7.4: Evoked response to white noise bursts (average of 60 bursts, 100 ms in length, 900 ms inter-stimulus-interval). Top: White noise burst, Middle: Overlay of 60 time-domain auditory evoked potentials (AEPs), Bottom: Average of 60 frequency-domain AEPs. Note that most of the evoked power lies between the first maximum and the subsequent minimum of the time-domain AEP.

- 70-80 Hz (γ , G)
- 100-110 Hz (high- γ , HG)
- 400-600 Hz (ultra-high- γ , UHG)

Each of the peaks may arise via a separate mechanism. We hypothesize that the ultra-high frequency response is due to the presence of sparse neurons close to the recording electrode, i.e. in layers 2/3, and potentially even in layer 1, as proposed by Gaona et al [48]. Weliky et al. successfully recorded low-amplitude multiunit activity stemming from layer

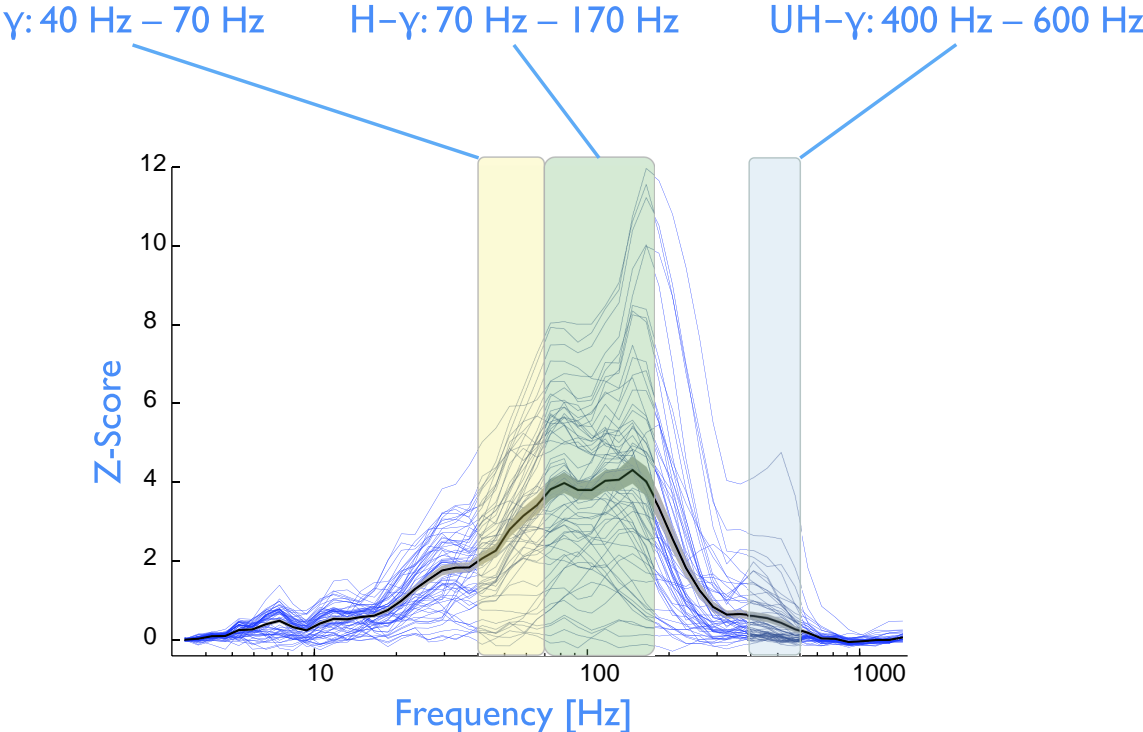


Figure 7.5: Overlay of spectra evoked by auditory stimulation with white noise bursts on 64 channels. Each spectrum is an average response across 60 WN bursts. The black trace corresponds to the mean spectrum bounded by the standard error of that mean (grey region). The predominant measure of neural response in this chapter is the high- γ power averaged between 70 Hz and 170 Hz, which captures the maximum of the mean spectrum. The local maximum between 400 Hz and 600 Hz is also worth noting as it appears quite prominently on some electrodes.

2/3 using surface electrodes with an electrode area of approximately $500 \mu m^2$ over the visual cortex of an anesthetized ferret [180]. In a theoretical study, Lempka et al. showed that increasing the electrode area from $500 \mu m^2$ to $1200 \mu m^2$ reduces the spike amplitude by a mere 8% and lowers the signal-to-noise ratio by only 6% assuming the spiking neuron is located only $50 \mu m$ away from the recording site [91]. Clearly, for larger electrode-neuron separation, both spike amplitude and SNR will be lower. However, in the limit that the electrode site diameter is much smaller than the electrode-neuron separation, the size of the electrode should become irrelevant. Thus, we hypothesized that our μ ECoG electrodes should be small enough ($40 \mu m$ diameter, i.e. $1256 \mu m^2$ in area) to record from such surface neurons $< 200 \mu m$ away [5]. To test this hypothesis, we have bandpass-filtered the μ ECoG data in the spike band (500 Hz - 5 kHz) and detected multi-unit activity by thresholding the absolute value of the filtered signal x at the threshold x_T developed by Quiroga et al. [137]:

$$x_T = 4\sigma_{noise} \quad \text{with} \quad \sigma_{noise} = \text{median} \left(\frac{|x|}{0.6745} \right) \quad (7.5)$$

where σ_{noise} is an estimate of the standard deviation of background noise according to Donoho and Johnstone [36]. We convolved this putative time-series of multi-unit firing with a 20 ms wide Hanning window to compute a temporally localised estimate of the multi unit firing rate (MUFR). Fig. 7.6 shows the average increase in firing rate evoked by the WN stimulus.

Fig. 7.7 shown 100 peak-aligned multi-unit waveforms recorded on an ECoG electrode. The waveforms are approximately 1 ms wide and the peak-amplitudes of range from $20 \mu V$ to $60 \mu V$, which is consistent with our expectations based on Weliky's work [180].

Not all but many of the 64 electrodes show a clearly stimulus-locked increase in average firing rate, which is consistent with the presence of a sparse but active population of neurons in close proximity to the cortical surface. Based on this success, we hypothesized that the same electrodes that showed multi-unit activity would also display a stronger stimulus-locked change in UHG power. However, we were unable to establish such a relationship, as shown in Fig. 7.8: There are many electrodes that show a pronounced UHG response while not showing an increase in MUFR and vice versa, thus indicating that UHG and active superficial neurons might both be real but distinct phenomena (e.g. UHG might represent mainly synaptic inputs while MUFR might represent primarily somatic firing).

The Neuronexus laminar probe (LP) similarly records AEPs in response to WN stimulation, which are variable in shape depending on the depth of the recording electrode. Interestingly, while most of the LP electrodes show a clear WN-triggered increase in multi-unit firing rate, the evoked spectrum is actually shifted to lower frequencies. This observation has at least two possible explanations: Either the observed UHG signal is not caused by the proximity of spiking cells to the electrode or the LP electrodes are simply too noisy to pick up the faint HG signature (i.e. the HG noise during silent periods is comparable to the HG signal during stimulus presentation, resulting in low z-scores for HG and UHG).

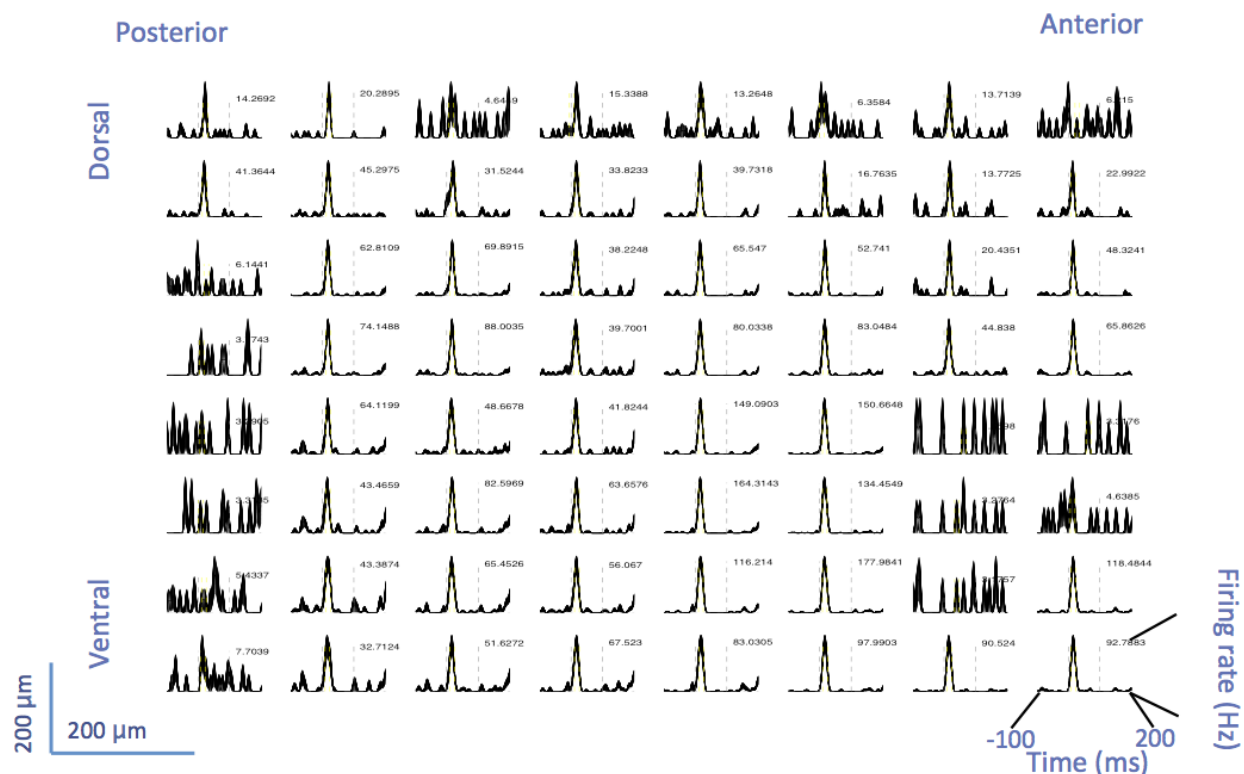


Figure 7.6: Most of the 64 electrodes show a considerable increase in multi-unit firing rate in response to white noise stimulation (mean plotted in response to 60 WN bursts). Time is shown on the x-axis and firing rate on the y-axis. Stimulus (WN burst) onset is indicated by the first grey line, stimulus end is indicated by the second grey line. The number next to each subplot indicates the trial-averaged peak MUF. Note that the firing rates detected on adjacent electrodes can be substantially different, which indicated that the electrodes, even though they are spaced by $< 200 \mu\text{m}$, carry independent information.

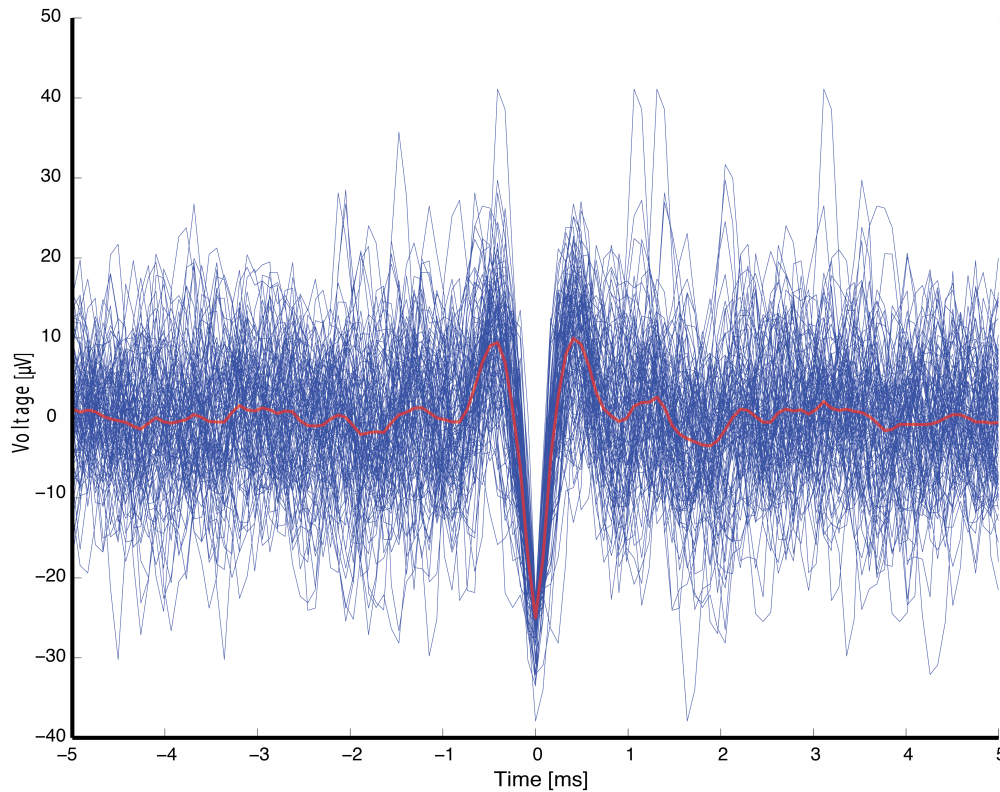


Figure 7.7: Overlay of 100 peak-aligned multi-unit waveforms as recorded on a representative μ ECoG electrode (blue). The red trace shows an average spike-triggered waveform of the 100 traces.

Responses to pure tone stimuli

Once the location of the auditory cortex was identified using WN stimuli, we proceeded to map auditory receptive fields using pure tone stimuli varying in amplitude from -70 dB to 0 dB, and from 0.5 kHz to 32 kHz in frequency, as graphically indicated in Fig. 7.9.

We found that the averaged power in the high gamma (HG) band (70-170 Hz) strongly depended on stimulus parameters and, when plotted as a function of the stimulus parameters, produced robust and highly localised tuning curves as shown in Fig. 7.10. As expected, the characteristic frequency (CF), i.e. the stimulus frequency associated with the maximum evoked gamma power, was roughly conserved across stimulus amplitudes. CFs showed a gradual progression from lower frequencies (2 kHz) to higher frequencies (20 kHz) that was clearly visible at the maximum spatial resolution of the μ ECoG array of 200 μ m.

We have investigated using the G, HG, UHG, and the multi-unit firing rate (instead of the single unit firing rate) as activity metrics for the computation of tuning curves and preferred frequencies for each electrode. Overall, we have determined that HG-power showed

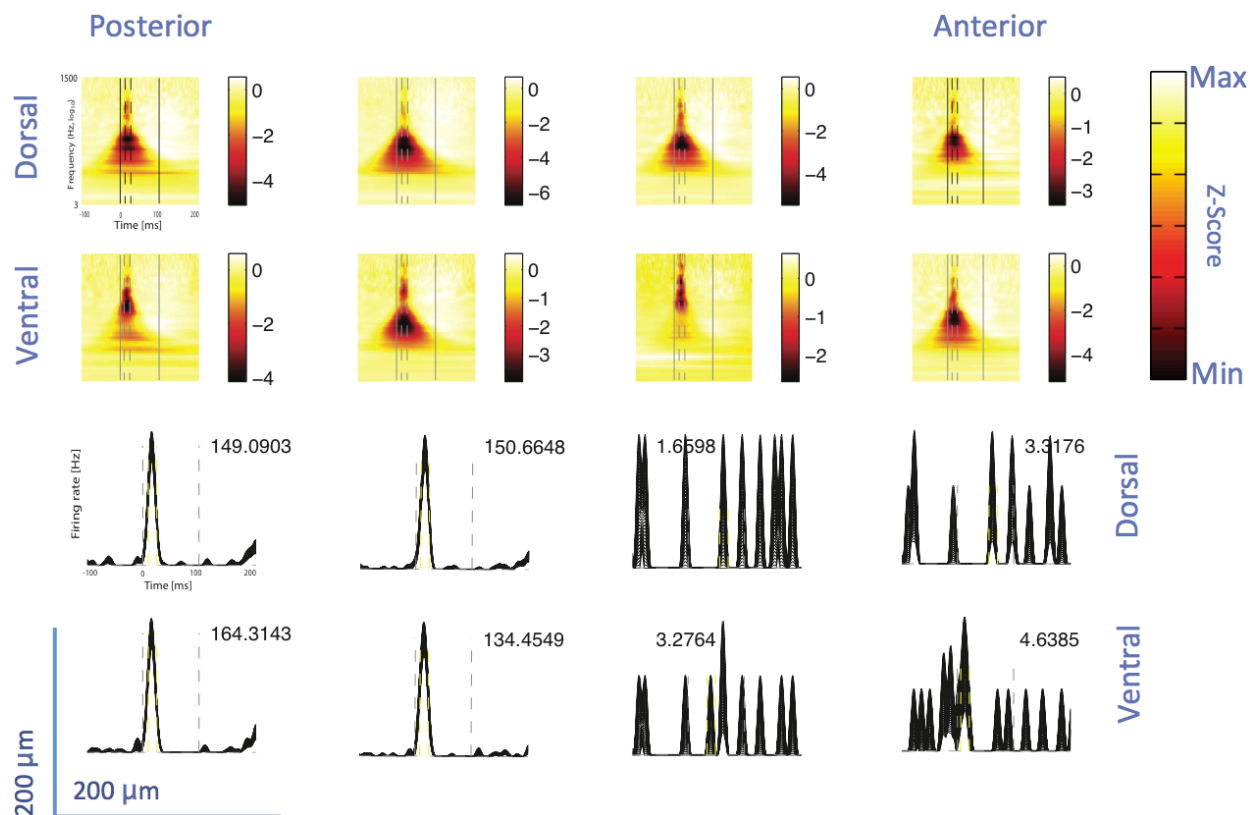


Figure 7.8: Top two rows: WN-evoked spectrograms on a group of 8 adjacent electrodes; bottom two rows: WN-evoked increase in firing rate on the same group of 8 spatially contiguous electrodes. There is no obvious relationship between the presence or absence of evoked G, HG, or UHG power and the presence (2 bottom rows: 4 plots on the left) or absence of firing rate modulation (2 bottom rows: 4 plots on the right).

the most robust tuning, which resulted in the largest number of tuned electrodes. Figure 7.11 shows a comparison between the tuning of G, HG, UHG, and MUFR.

Tuning permutation test

Tuning was determined based on a permutation test based on the assumptions that if an electrode has a characteristic frequency, then it should be roughly conserved across stimulus-amplitudes. First, the tuning curve was averaged along the sound amplitude dimension, and the standard deviation of the resulting vector was computed to determine a measure for the average modulation of the tuning curve. In a second step, the stimulus amplitude-frequency relationship was pseudo-randomly scrambled 100 times, which by analogous computation yielded a distribution of modulations. A tuning curve was considered ‘significantly tuned’

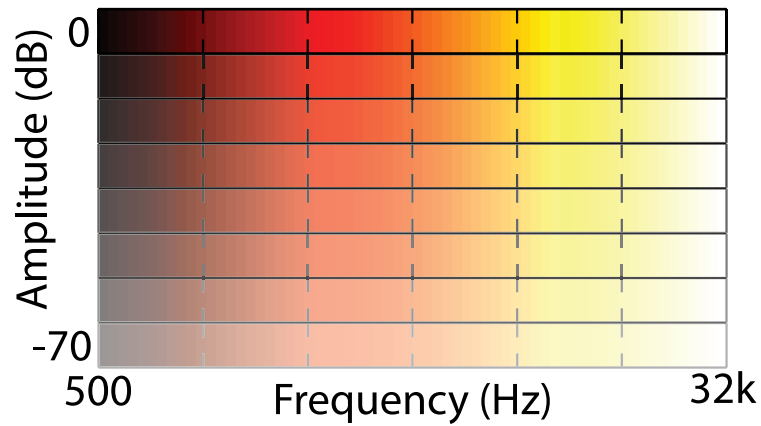


Figure 7.9: Two-dimensional pure tone stimulus set. Each frequency-amplitude pair was repeated 20 times. The tone duration was 50 ms and the inter-stimulus interval (ISI) was 250 ms. Image credit: Kris Bouchard, Chang Lab, UCSF.

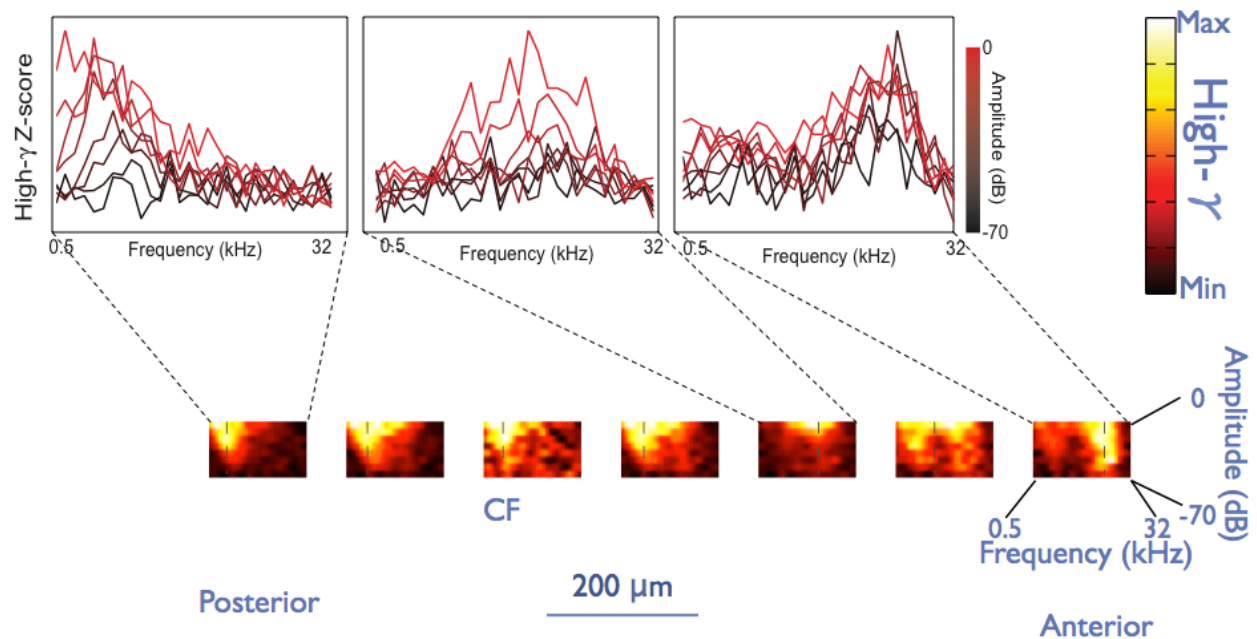


Figure 7.10: Fine-grained electrocorticographic mapping of auditory receptive fields. Tuning curve shape and characteristic frequency vary significantly even over distances as small as $200 \mu\text{m}$. The characteristic frequency is approximately conserved across stimulus amplitudes, color-coded from black (-70 dB) to red (0 dB).

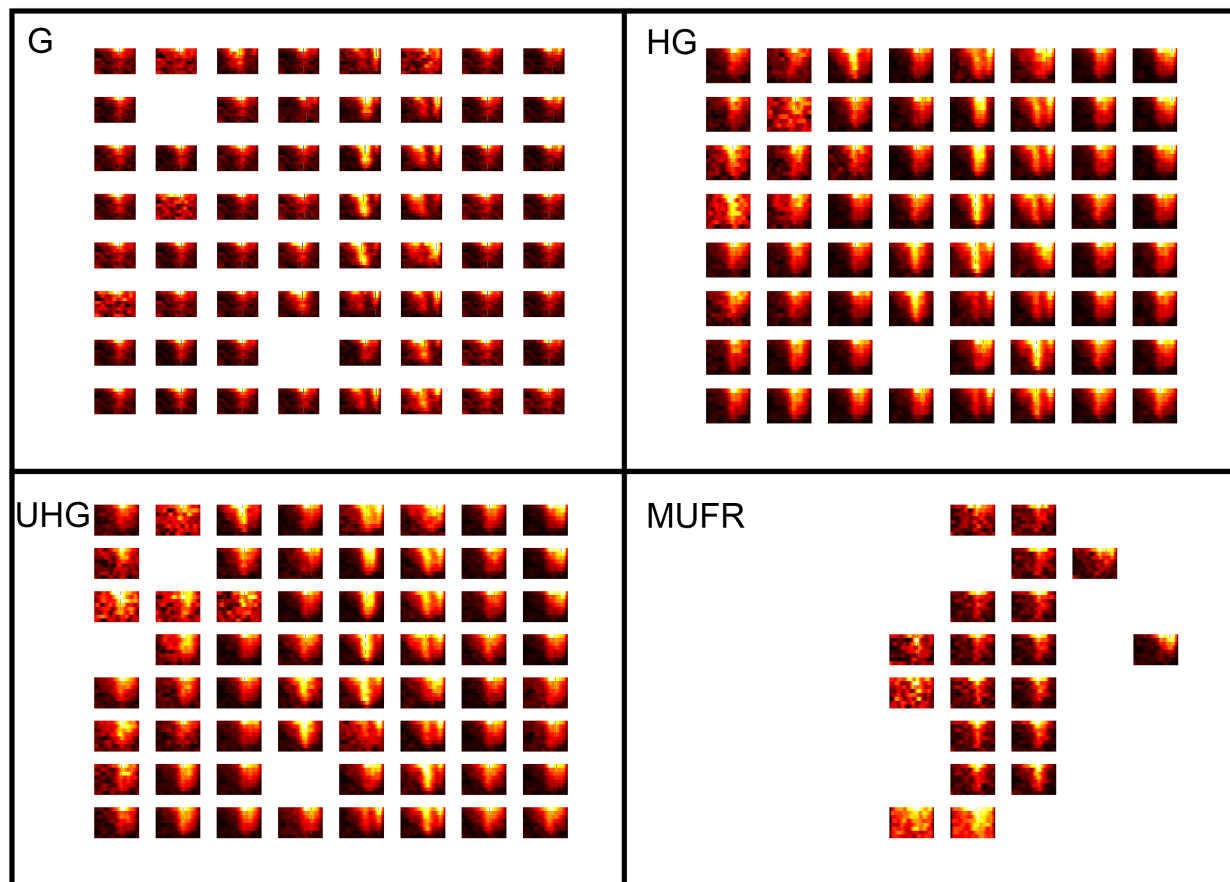


Figure 7.11: Using high-gamma (HG) power as a metric for neural activity yields the highest number of tuned electrodes and the most robust tuning curves, as compared with using gamma (G) power, ultra-high gamma power (UHG) or multi-unit firing rate (MUFR).

when its modulation was larger than that of 95/100 randomly scrambled tuning curves ($p < 0.05$). Response plots for electrodes that were not tuned according to this test were left blank in the figures of this chapter.

Mapping with high gamma on the surface is more robust than mapping with intracortical MUFR

As mentioned in the introduction to this chapter, the gold-standard for receptive field mapping requires measuring stimulus-associated changes in spike firing rate with intracortical electrodes. We have computed tuning curves from spike data recorded intracortically and from μ ECoG data recorded on the surface of the cortex (from the same volume of tissue) in order to verify that both approaches yield similar receptive fields, as shown in Fig. 7.12.

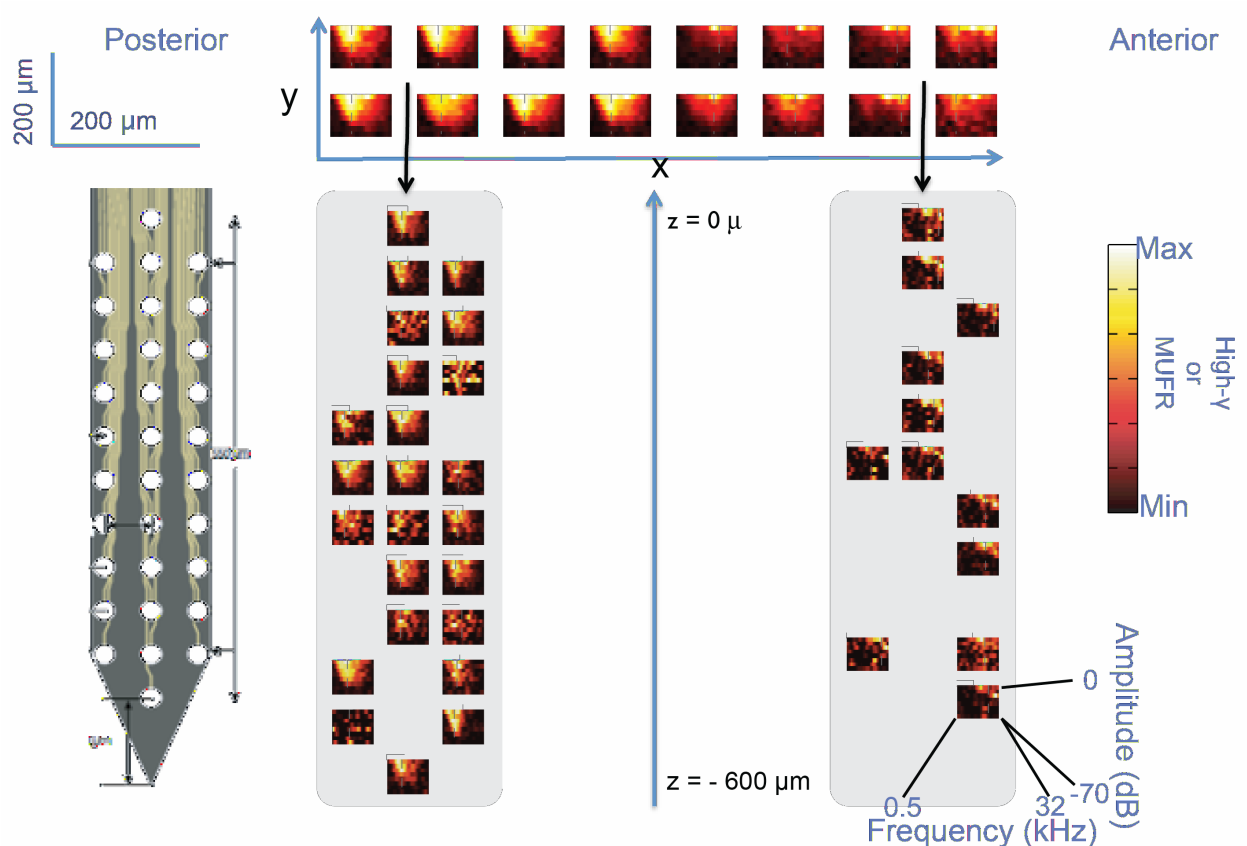


Figure 7.12: Comparison of μ ECoG-derived tuning curves (tuning curves on 16 plots in the xy plane are shown) with laminar-probe-derived tuning curves (gray boxes: only tuned channels of laminar probe are shown). The tuning curves derived from surface measurements of HG power are very similar to the tuning curves derived from intracortical spike firing measurements taken in the same xy-vicinity, albeit the intracortical tuning is a little sharper. As expected, the characteristic frequency remains roughly constant along the z-axis of the intracortical laminar probe introduced perpendicularly to the cortical surface.

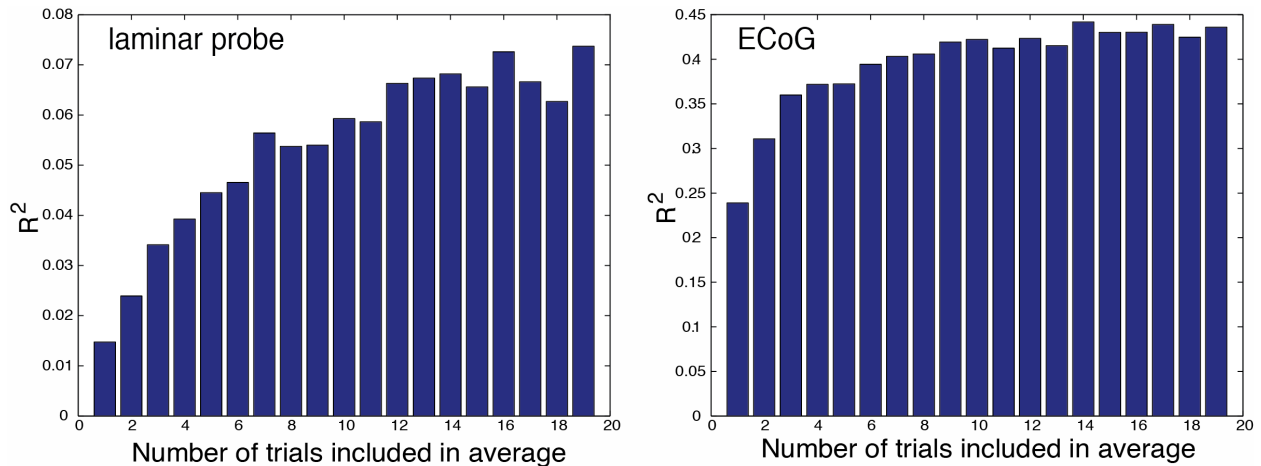


Figure 7.13: Saturation of the average’s predictive power occurs for a lower number of trials when the HG-portion of the μ ECoG LFP is used to compute the tuning curves Fig. 7.13 (right) as compared to MU signal recorded with penetrating electrodes Fig. 7.13 (left). Note that the coefficient of determination for the same number of averaged trials is much lower for firing rate tuning than it is for HG power tuning. This indicates that when compared point-wise, firing-rate derived tuning curves in single-trial are much noisier than HG-power derived tuning curves in single-trial.

Minimum number of stimuli to determine robust tuning

We employed a leave-one-out cross-validation scheme to test how many copies of the same stimulus we need to present before presenting additional stimuli ceased to significantly affect the shape of the tuning curve: For each $n \in \{1, 2, \dots, 20\}$ we drew 20 random combinations of n tuning curves, left one out, and compared the average of those $n - 1$ tuning curves $\bar{Z}(A, f)_{2..n}$ to the left-out tuning curve $Z(A, f)_1$ by computing the coefficient of determination R^2 point-wise:

$$R^2 = \frac{\langle \bar{Z}(A, f)_{2..n} | Z(A, f)_1 \rangle^2}{\langle Z(A, f)_1 | Z(A, f)_1 \rangle \langle \bar{Z}(A, f)_{2..n} | \bar{Z}(A, f)_{2..n} \rangle} \quad (7.6)$$

For increasing n , on average, the power of $\bar{Z}(A, f)_{2..n}$ to predict $Z(A, f)_1$ saturates as shown in Fig. 7.13. Notably, this saturation occurs for a lower number of trials when HG μ ECoG signal is used to compute the tuning curves Fig. 7.13 (left) as compared to MUF R signal recorded with penetrating electrodes Fig. 7.13 (right). This fact supports the idea that HG μ ECoG signal, which arises from a larger population of neurons and essentially provides an estimate of population activity, has higher statistical power [109, 110] than average firing rates derived from merely a few neurons.

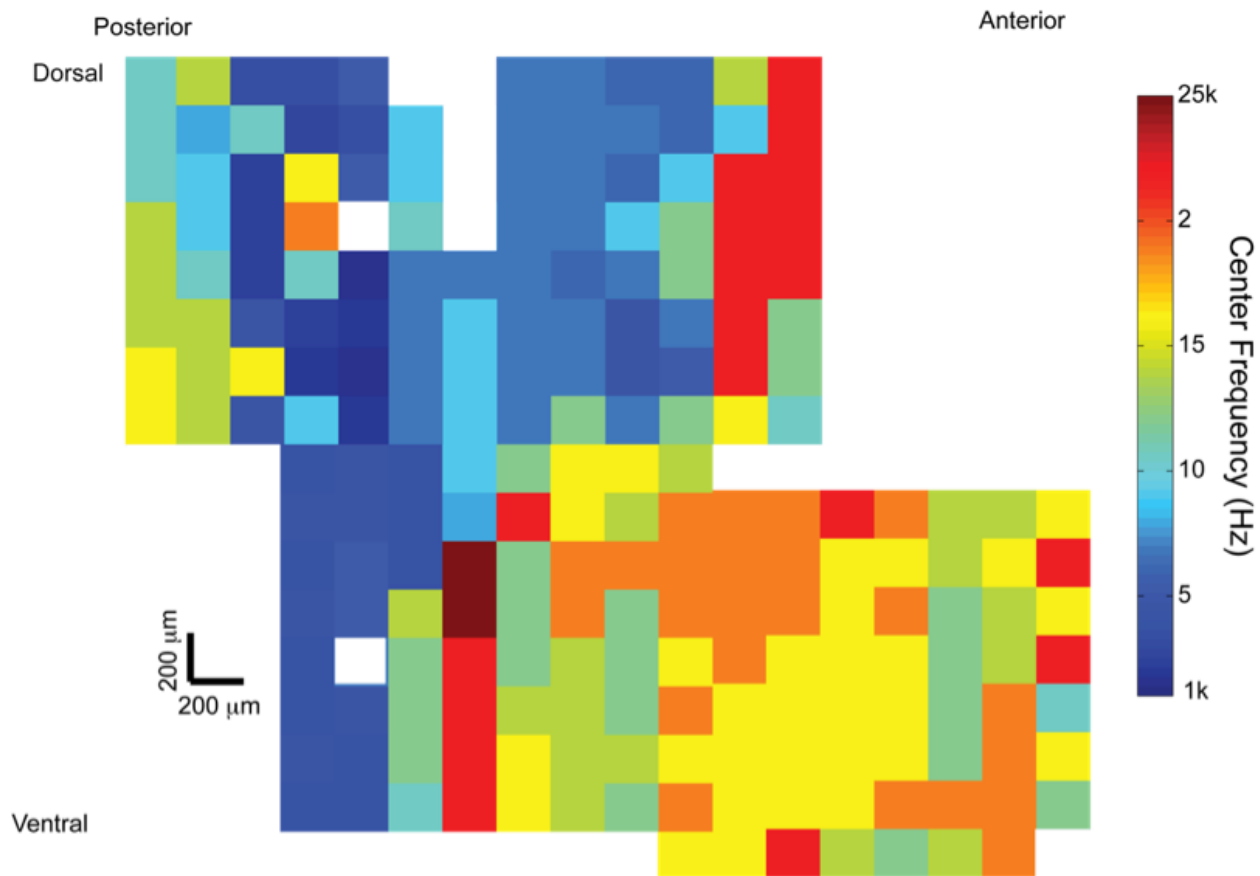


Figure 7.14: Stitched tonotopic map generated by moving the array to four different auditory areas (A1, VAF, SRAF, AAF) computed from data that was acquired in less than 2 hours total (30 minutes per location). This map is quite reminiscent of the one painstakingly compiled by Polley et al. in [135] (see Fig. 7.1 for comparison). Image credit: Kris Bouchard, Chang Lab, UCSF.

μ ECoG enables fast, non-destructive functional mapping

The WN block is slightly over a minute in duration, the pure tone block, i.e. 20 repetitions of each frequency-amplitude pair (4800 stimuli total, 300 ms per trial) takes 24 minutes. Thus a 1.6 mm \times 1.6 mm area of cortex can be mapped nondestructively, and in 64 locations in parallel, in under 30 minutes. In acute experiments, the μ ECoG array can be easily moved without causing damage to the cortex. Fig. 7.14 shows a stitched tonotopic map, courtesy of Kris Bouchard, generated by moving the array to four different locations of auditory cortex (A1, VAF, SRAF, AAF) in under 2 hours total, an order of magnitude improvement compared to serial mapping with penetrating electrodes [135].

7.4 Conclusion

In this chapter we have demonstrated that HG power is a robust measure of neural activity that can be used to create spatially very fine-grained ($200\ \mu\text{m}$) tonotopic maps of auditory cortex in a rapid and non-destructive fashion using μECoG . We have also verified that the obtained tuning curves as a function of spatial location are almost identical to tuning curves obtained from pain-staking intracortical spike recordings. In fact, deriving tuning curves from HG power recorded on the surface of the brain is statistically more robust in the sense that less copies of the same auditory stimulus need to be presented to obtain a stable tuning curve estimate.

According to our analysis, ≤ 10 repetitions of each frequency-amplitude pair are required to obtain robust tuning curves for HG responses. Thus, cortex below the μECoG array can be mapped in less than 15 minutes. Using a 256 channel array with $4\times$ the area and with the same electrode density would then allow to map all auditory areas simultaneously in under 15 minutes and without the need to move the array. This technology will allow to create functional maps routinely in chronically implanted animals, and to investigate the dynamic changes in these maps induced through learning and plasticity.

Moreover, often the small ($\approx 1250\ \mu\text{m}^2$) microelectrodes pick up multiunit activity with a derived firing rate that exhibits tuning. At least two hypotheses on the origin of these spike-like signal come to mind. Our main hypothesis, which is consistent with work by Weliky [180], is that we are indeed observing sparse somata located within $100\ \mu\text{m}$ of the μECoG electrode. However, it is also conceivable that we are seeing dendritic Ca^{2+} spikes propagating in the upper tufts of large layer 5 pyramidal cells, which are located in layer 1 [61]. Such spikes may be generated by either synaptic inputs from layer 1 cortico-cortical projections [63], or even by action potentials of layer 5 neurons backpropagating from the somata [86]. Most likely, all of the hypothetical mechanisms described above contribute to the multi-unit signal that we registered on the cortical surface, which intriguingly suggests that the μECoG signal may rather uniquely combine information about the output of upper with the input to deeper cortical layers. The relative contributions of these sources to the μECoG signal can be explored in future experiments by recording Ca^{2+} signals optically through transparent μECoG electrodes [89].

Dense μECoG blurs the line between multiunit and field potential recordings. Given that we have shown both stimulus-related MUF_R and HG power to be highly local, clearly, even at $200\ \mu\text{m}$ center-center spacing, adjacent electrodes often carry independent information. Thus, if the goal is to obtain additional information through higher spatial sampling, there is good reason to fabricate μECoG grids of such high (or even of higher) density. One interesting question remains: Is the presence of such spatially steep functional gradients, hard-wired into the anatomical nature of the auditory cortex? Or is it subject to plastic change through learning? If the latter is true, such high-density μECoG arrays may be useful to create minimally invasive, but nonetheless high-performance brain-machine interfaces. This intriguing possibility will be explored further in the next chapter.

Chapter 8

μ ECoG BMI in rat

8.1 Introduction

At cellular length scale, neurons constitute discrete functional units that are readily decoupled in a closed-loop Brain Machine Interface (BMI) setting [28]. Likewise, volitional activity control of large brain areas (e.g. motor cortex vs. visual cortex) has been established through EEG-based BMI [104]. However, volitional decoupling of mesoscale activity on the order of a single (or of a few) cortical column (100s to 1000s of microns), as well as the optimal size and nature of such hypothetically controllable functional domains, remains highly debated. Electrocorticography (ECoG), the measurement of electrical potentials on the surface of the cerebral cortex, is uniquely suited to investigate such mesoscopic cortical length scales. Rouse et al. recently demonstrated that monkeys can be trained to decouple gamma activity (power of ECoG signal between 65 and 115 Hz) on arbitrarily chosen electrodes to perform a 1-dimensional center-out BMI task with visual feedback [142], as opposed to functionally pre-selected electrodes commonly used in human ECoG-BMI experiments on patients who undergo pre-surgical mapping before surgical epilepsy intervention [14]. Rouse's output electrodes i.e. electrodes chosen for BMI control were separated by more than 3 mm and placed over anatomically distinct functional areas: one over primary motor cortex (M1), the other over dorsal premotor cortex (PMd) of a macaque monkey. In this chapter, we are using an experimental paradigm similar to Rouse's to investigate if gamma power decoupling can be learned for output electrodes that are separated by $<1mm$ and that are located over the *same* macroscopic functional area (M1). To this end, we have developed a custom microelectrode array (design shown in Fig. 3.9; micrograph shown in Fig. 5.5 (left)) with 200 μm electrode pitch and modified the electrode surface to lower impedance and reduce thermal noise as shown in Fig. 5.5 (right). We have chronically implanted the arrays over primary motor cortex (M1) of five male Long-Evans Rats and successfully trained the animals to adjust the pitch of an auditory cursor in a one-dimensional center-out task by differentially modulating high gamma (70-110 Hz) power on two surface microelectrodes. These output electrodes were merely preselected to exhibit a medium level of spontaneous

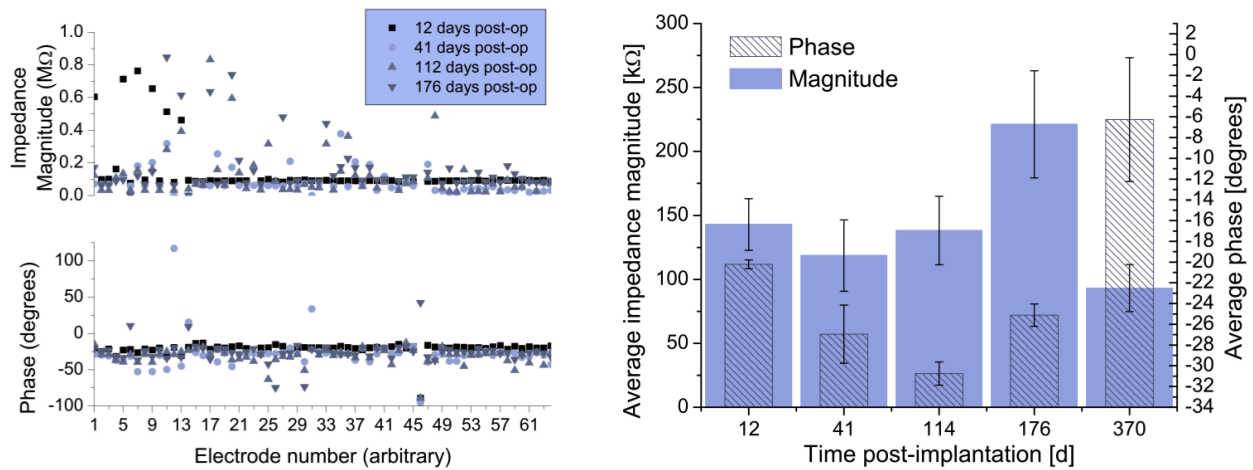


Figure 8.1: Time course of impedance magnitude and phase, post-implantation, averaged over the 64- μ ECoG electrodes. The error bars reflect the standard error of the mean. Most electrode impedance magnitudes were in the range acceptable for acquisition of surface local field potentials ($< 1M\Omega$ at 1 kHz). This caption and figure have been modified from [88] with permission; ©IEEE 2013.

activity and mutual correlation in the gamma band but otherwise chosen arbitrarily. This BMI task was a modification of the single-unit based control paradigm reported by Koralek et al. [80]. This chapter has been modified from [88] with permission; ©IEEE 2013.

8.2 Chronic impedance monitoring

Chronic implantation protocol

The following protocol for the chronic implantation of Parylene C μ ECoG devices over the motor cortex of rodents has been developed at UC Berkeley, in the laboratory of Jose M. Carmena, with the generous help of Aaron C. Koralek. All of the procedures outlined below were performed in compliance with the regulations of the Animal Care and Use Committees (ACUC) at the University of California, Berkeley. While the procedure has been specifically developed for chronic implantation in rats, it should be straightforward to translate it into mice, with only minor modifications. In fact, the author has prototyped a very similar surgery in a mouse, in the laboratory of Karl Deisseroth at Stanford with the help of Viviana Gradinaru, PhD (unpublished).

The surgery was developed on Long-Evans rats, weighing approximately 250 g. Anesthesia was induced with a brief high dose of isoflurane gas (3-3.5% in O_2) followed by Ketamine ($50 \frac{mg}{kg}$) and Xylazine ($5 \frac{mg}{kg}$). Anesthesia levels were tested by the absence of a toe-pinch re-

flex, and maintained with supplemental isoflurane gas (0.5%) throughout the surgery. Sterile technique (surgical gloves and autoclaved surgical tools) were used throughout all surgical procedures.

The animal's head was shaved and fixated using ear bars in a conventional Kopf stereotax, with the body positioned on a heating pad that has to be well temperature-controlled in order to avoid premature passing of the animal. It is imperative not to put undue pressure on the earbars¹. The shaved region was disinfected with Nolvasan and alcohol (70%) and an incision, approximately 2 cm in length along the longitudinal axis, was performed with a scalpel. The fascia was cut with scissors and the scalp spread by pulling on the fascia with forceps to reveal the skull. The skull was scraped using a curette, and dried in order to enhance adhesion of the dental acrylic cap at the end of the surgery.

4-5 holes for skull screws were drilled along the perimeter of the exposed skull. The skull screws provide additional stability and adhesion for the acrylic cap. Two of these skull screws, typically anchored in the thicker, posterior part of the skull, served as combined (i.e. shorted) ground and reference.

Stereotactic coordinates relative to bregma were used to identify the location of primary motor cortex (M1): anteroposterior 2 mm, mediolateral 2 mm. A small craniectomy (2 mm \times 3 mm) was performed centered on above coordinates by milling out a rectangular outline using a high-speed drill, and by hooking under the piece of skull using fine-tip tweezers. During the entire process, the craniectomy area was cooled and moistened by periodic application of isotonic saline. The dura was removed very carefully, in order to avoid bleeding, by hooking under it with a bent needle. The array was held in place by the TDT ZC64 ZIF-Clip headstage attached to an xyz-micromanipulator arm mounted to the stereotax. It is advisable to wrap the Pt/Ir ground wire of the electrode array around the two posterior skull screws while the array is in close proximity to the skull but before bringing it in contact with the cortex because manipulating the comparatively stiff wires is likely to move the array from its desired position. The array was lowered roughly perpendicularly to the skull and positioned in the xy-plane such that when lowered vertically, the edge of the μ ECoG would touch the lateral edge of the exposed cortex first. The array was progressively lowered and the adapter board moved medially (or towards the opposing hemisphere) so that the electrode array came to rest over M1, with the cable flat against the skull, until the adapter PCB came to rest against the skull between the skull screws. Thin slices (<1mm) of Gelfoam were placed over the craniotomy to protect it from the harsher chemicals used to create the hard cap in the following step. The Gelfoam was followed by a layer of superglue that secured the position of the Parylene relative to skull and adapter board. Superglue is used to carefully protect the craniectomy, the ground wire, and all Parylene (including the bond pad array, achieved by surrounding the entire bottom portion of the adapter board with superglue), while avoiding contact of superglue with the skin. The superglue was set instantly by adding a few drops of Zip Kicker. Once the μ ECoG was secured with set superglue, the ZIF-Clip

¹While the fixation needs to withstand forces applied during craniectomy drilling, overly tight earbars can result in pressure on the brainstem followed by respiratory arrest several hours into the surgery.

adapter holding it was removed, and a dental acrylic cap was built to secure the ZIF-Clip connector. To promote proper wound healing during post-surgical recovery, it is important to ensure that the acrylic cap be smooth. After the surgery, the wound edge was treated with topical antibiotic ointment and the animal received subcutaneous pain killers. Six-to eight hours after recovery, the animal received another dose of pain-killers *sc.*, and was placed in a clean cage with unlimited supply of food and water for recovery. According to protocol, the animal's recovery was monitored by daily weighing; scabs were removed daily from the wound edge and antibiotic ointment applied for 7-10 days post-surgery.

For the experiments described further below in this chapter, a total of five male Long-Evans Rats weighing roughly 250 grams were chronically implanted with subdural 64-channel μ ECoG arrays over primary motor cortex (M1) of the right hemisphere.

In vivo impedance monitoring

In order to assess device health after implantation, we measured the electrochemical impedance at 1kHz at five different time points: 12 days, 41 days, 114 days, 176 days, and 370 days post-operatively. The measurements were performed using the nanoZ (WhiteMatter, LLC); the counter electrode was attached to the rat's tail. On average, we observed a slight decrease in impedance magnitude as a function of time post-implantation (Fig. 8.1).

Variability in electrode impedance indicated the absence of inter-electrode shorts, and was interpreted as an absence of delamination. Most electrode impedance magnitudes were in the range acceptable for acquisition of cortical surface field potentials ($< 1M\Omega$ at 1 kHz).

8.3 Brain control of auditory cursor

Cortical field potentials were simultaneously recorded using a 64-channel Zif-Clip headstage (Tucker-Davis Technologies, ZC64) connected to a Multichannel Acquisition Processor (MAP; Plexxon Inc., Dallas, TX) through a commutator. Behavioral timestamps were sent to the MAP recording system through Matlab (Mathworks, Natick, MA) and synchronized to the neural data for later analyses. All continuous data was sampled at 1 kHz.

Behavioral task

The behavioral task was a variation of [80]. After the rodents recovered from surgery (typically 7-10 days), two low-noise microelectrodes over M1 were chosen at random given the constraint that they be between 200 μ m and 1 mm apart in space (center-to-center). The negative logarithm² of gamma power (70 Hz - 110 Hz) was averaged over non-overlapping 200 ms windows and entered into an online transform algorithm that translated gamma powers

²We have chosen to use the negative logarithm of the high-gamma power over high-gamma power directly as a control signal because high-gamma power appears to be log-normally distributed in time such that the negative logarithm of high gamma provides us with a more convenient, normally distributed, control signal.

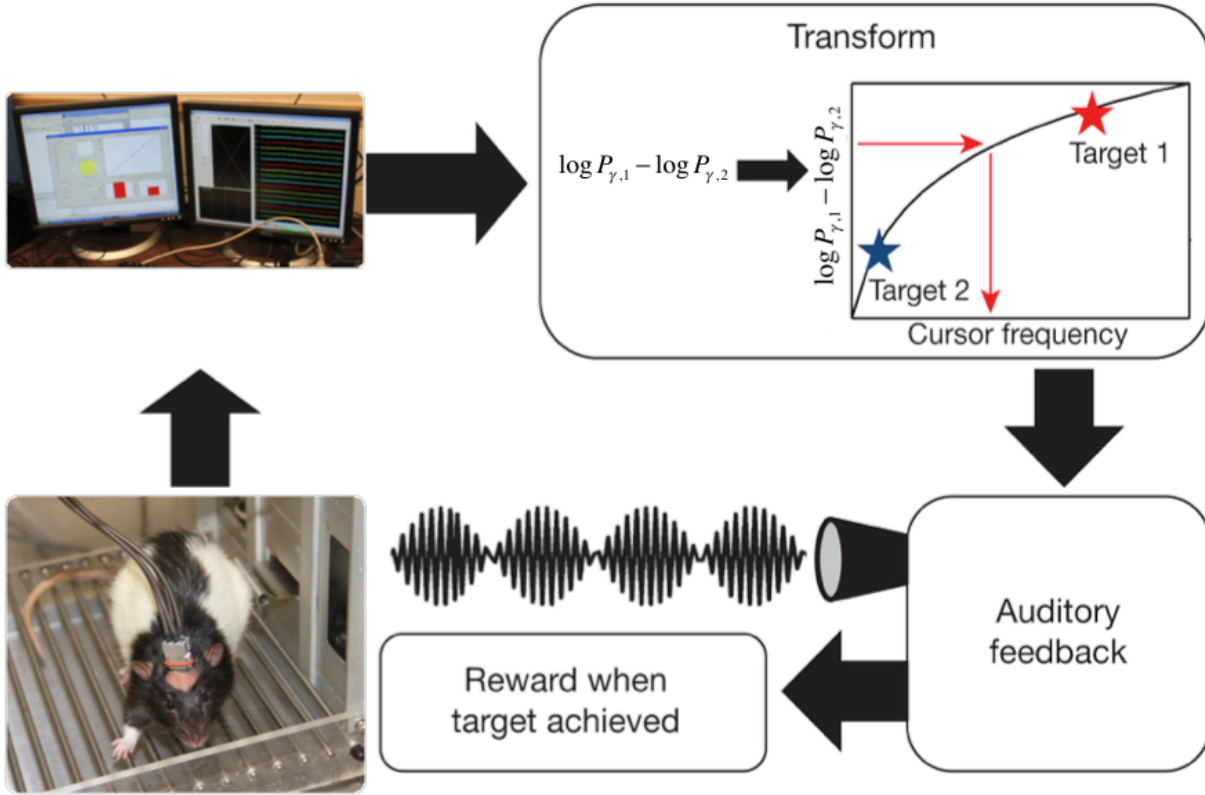


Figure 8.2: Experimental paradigm: an awake behaving rat modulates high γ power on two selected electrodes. The difference of the negative logarithm of the gamma power between the two electrodes is mapped onto the pitch of an auditory cursor (a tone that the rat can hear as a form of auditory feedback about the position of the cursor, updated every 200 ms). When the cursor reaches a target tone, the animal obtains a food or a sugar water reward. Modified from Fig. 1 of [80], reprinted by permission from Macmillan Publishers Ltd: Nature [80], ©2012.

$P_1^\gamma(t_i)$, $P_2^\gamma(t_i)$ averaged over the i -th time window into the pitch $f(t_i)$ of an auditory cursor that was updated every 200 ms. The specific transform used was:

$$f(t_i) = \alpha_1 \cdot P_1^\gamma(t_i) - \alpha_2 \cdot P_2^\gamma(t_i) + \beta \quad (8.1)$$

where the coefficients α_1 , α_2 , and β were dynamically recalculated based on baseline recordings in absence of auditory feedback. Under this transform, increased activity on the first electrode produced a heightening of the cursor pitch, while increased activity on the other electrode resulted in lowering of the cursor pitch. The BMI paradigm is illustrated in Fig. 8.2. A photograph of the practical implementation of that paradigm is shown in Fig. 8.3.

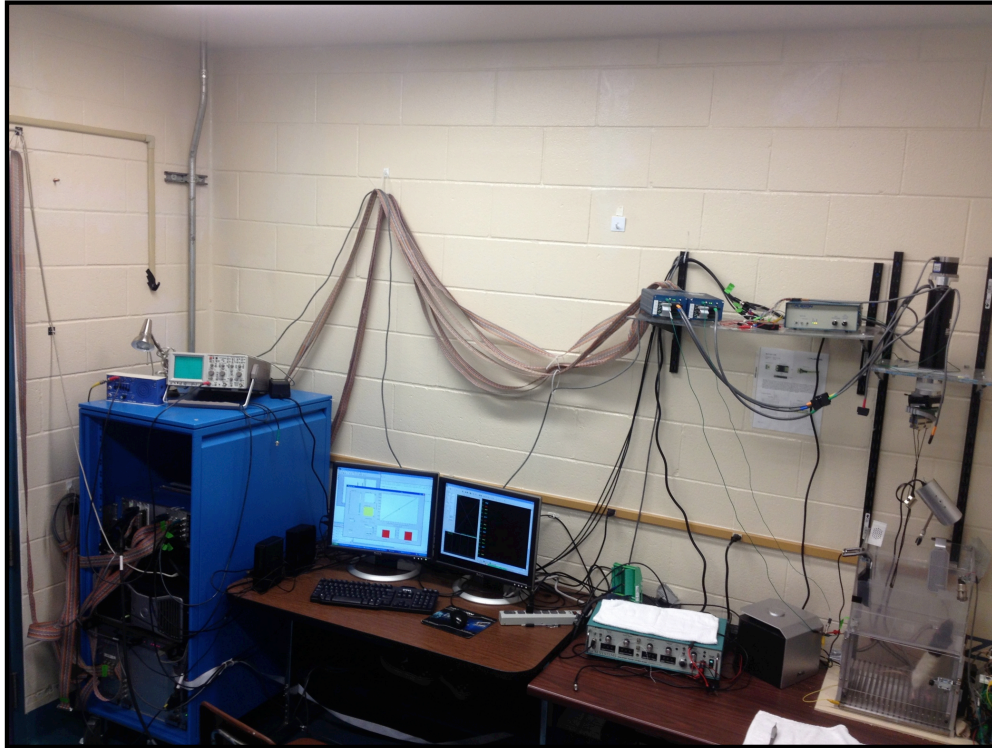


Figure 8.3: Experimental setup in the Carmena lab at UC Berkeley: The awake behaving rat is connected to the Plexxon system via a TDT ZC64 headstage, a series of adapters, a commutator and two pre-amplifiers.

Thus, in order to move the cursor in any one direction, the rodents had to learn to modulate high-gamma power on the two chosen electrodes differentially, as opposed to modulating bulk high-gamma activity in M1. The high-gamma power modulation had to be precise to move the cursor to one of two target pitches to obtain a target-specific reward, either in form of 20% sucrose solution or in form of a 45 mg food pellet. A trial was marked incorrect if neither of these targets were achieved within 30 seconds of trial initiation. Chance levels of target achievement were estimated from daily baseline recordings, 1000 cycles (200 s) long, in absence of auditory feedback.

Closed-loop learning performance

Even for electrode separations as small as 200 μm (center to center), the animals were able to perform the BMI task significantly above chance as shown in Fig. 8.4. Successful days were characterised by a rapid increase of target accuracy until saturation (Fig. 8.4, left) and by a continuous decrease in reach time, i.e. time from trial start to target, over the course of a session (Fig. 8.4, right). Overall, performance was above chance on most

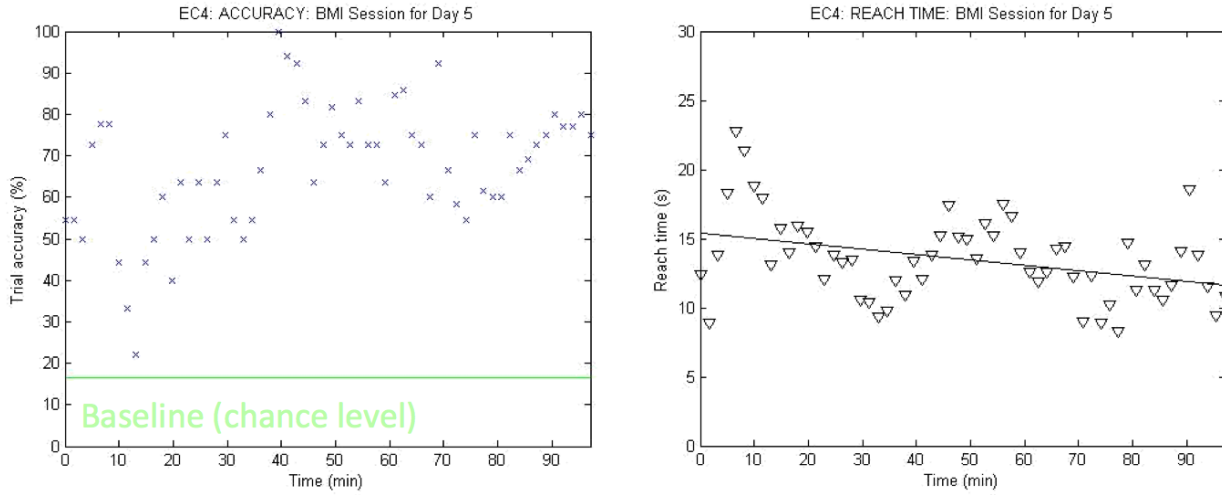


Figure 8.4: Example of a successful BMI session. Left: Target accuracy starts close to the baseline (chance level) and increases in the first 30 minutes of the session until saturation is reached. Right: The reach time (time-to-target) steadily decreases over the course of the session.) The output electrode separation in this particular session was $200\ \mu\text{m}$.

days; an average of target accuracy over all animals and sessions as a function of session time up to 1 h into the session, displayed in Fig. 8.5, reveals that, performance improves in the first 30 min of the session before saturation is reached. It is noteworthy, that this average ‘intrasession learning’ curve does not start out at 0% accuracy above baseline, but at around 8%. This implies that there is at least some improvement of the initial accuracy across days, which implies at least a small degree of skill-consolidation. However, we observed that improvement to be weak and non-monotonic as a function of session number.

Target accuracy as a function of electrode distance

We performed variations of the above experiment where we altered the electrode distance of the output electrodes (by choosing different electrodes on the grid for the control pair) for two days at a time to test if the rats could learn alternative decoders and to investigate whether their ability to modulate high-gamma power differentially would break down for electrodes that were too close together. We hypothesized that there might be a preferred length scale around $600\ \mu\text{m}$, based on a publication by Slutzky et al. [159], and based on the published scale of cortical columns proposed in literature [112] for which decoupling might be particularly easy to learn. We further suspected that the BMI task may not be learnable for certain arbitrary choices of electrode pairs, which happen to lie over cortical columns that belong to the same functional columnar network, as postulated on computational grounds in [158]. We used the average saturation accuracy between 30 and 60 min of each session to

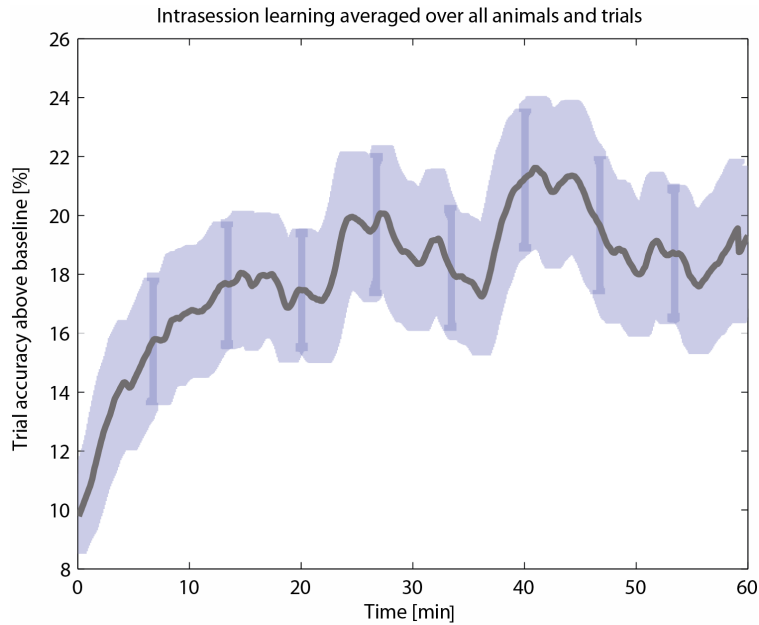


Figure 8.5: Average of target accuracy above baseline across all animals and sessions as a function of time in each session. The error bar envelope indicates the standard deviation (sample error) across animals and sessions. On average, accuracy increases to saturation in the first 30 minutes of a session.

compute a metric for the cumulative performance of any given session. In most cases, the animals were able to learn to use new pairs of output electrodes quickly (often in a single sessions) and significantly above chance but without the expected statistically significant dependence of the learning performance on the electrode separation between the output electrodes (Fig. 8.6). At the same time, we have indeed anecdotally observed that across all investigated length scales, the rats' ability to learn the BMI task may depend on the specific choice of control electrodes. The presence of columns in motor cortex is highly contested [20]. And the absence of a preferred length scale in our data that facilitates decoupling contradicts the hypothesis that decoupleability has anything to do with columnar organisation. Based on results described in the last chapter (Sec. 7.3), namely the potential presence of sparse superficial layer 2/3 neurons close to the μ ECoG electrodes that heavily contribute to the high-frequency activity observed on those electrodes, an alternative hypothesis is more probable: decoupleability of high- γ is likely dependent on the presence of sparse superficial multi-units close to the μ ECoG electrodes.

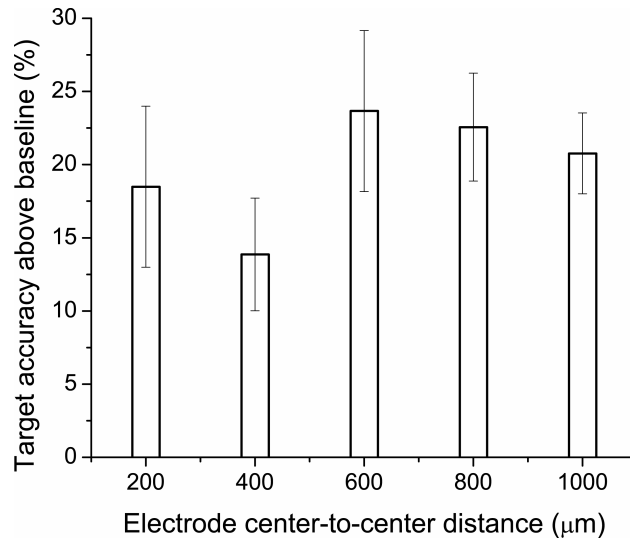


Figure 8.6: Target accuracy above chance as a function of distance between the output electrodes: The animals are able to learn controlling to control the auditory cursor even if the output electrodes were adjacent, (i.e. as close to each other as 200 μm center-to-center.). However, no statistically significant dependence of the cumulative target accuracy on the electrode separation was observed. The error bars indicate the standard error of the mean across animals and sessions.

8.4 Conclusion

This work carries implications for the development of practical μ ECoG-based BMI. It demonstrates the benefits of high-density electrode arrays in the sense that high-frequency components of the signal recorded by μ ECoG electrodes as close to each other as 200 μm can be volitionally decoupled by training, which could promote the development of clinically relevant, minimally invasive neural interfaces that do not break the blood-brain barrier and can be implanted through very small burr holes. However, the lack of a significant session-to-session improvement in performance is disconcerting as it may limit the utility and performance of such a neural interface.

The correlation between target accuracy and cortical microanatomy below the control electrodes merits further in-depth investigation in order to determine whether decoupling is truly linked to plastic changes in superficial multi-units in close proximity to the μ ECoG electrodes. If that hypothesis were indeed to be confirmed, it should be possible, provided the μ ECoG signal can be sampled adequately temporally (ideally at 40 kHz), to use a μ ECoG neural interface for high-performance multi-unit (thresholding) based BMI control [52] in humans. Since these superficial units are sparse, likely control electrodes would need to be preselected to indeed be close to the sparse populations of superficial neurons.

Chapter 9

Conclusions and future work

9.1 The limitations of the Parylene process

In the course of this thesis we have developed a custom microfabrication process based on lithographic patterning of Parylene C and conductor stacks that allows to manufacture very thin (6-15 μm) and flexible, single or multi-layer, μECoG arrays, flexcables for neural probes, and potentially other high-density microflex interconnects. In its current state, the process supports a minimum feature size of 5 μm trace/space. This feature size can likely be pushed to 3-4 μm trace/space but probably not much further, limited by the need for a T-shaped resist profile during conductor lift-off and by the quality of adhesion of photoresist to Parylene C. Device thickness can also be safely reduced if needed to 2 μm per Parylene C layer, which we have found to be the minimum thickness that guarantees well-insulating, pinhole-free Parylene C films using the SCS Parylene deposition tool available to us in the Marvell Nanolab. It is quite likely that a superior plasma-assisted or ultra-high-vacuum deposition tool, would yield thinner, high-quality Parylene layers. Higher quality thin Parylene C layers would be most valuable for 2+ conductor layer devices, as devices with a total thickness < 6 μm are quite fragile, difficult to handle, and thus of questionable practical utility. We have also demonstrated that not only traditional metallic conductors are compatible with this process but that transparent electrodes can be fabricated using indium tin oxide as the conductor material for the electrodes in conjunction with traditional ductile metal, such as gold, for long conductor traces.

Like most lithographic fabrication schemes, our process shines for the fabrication of a large number of identical devices, each of which should be small in area compared to the size of carrier wafer used (4" currently). For high-yield, large area devices, this process is less practical because it is very difficult to avoid particulate-related or other lithographic defects at least on some parts of the wafer. If low volumes of custom-designed larger area devices are desired, direct-laser patterning would be the superior method as both Parylene C, and platinum can be ablated with pulsed UV-laser [152].

Passive Parylene-conductor microflex devices seem to fare rather well in accelerated life-

time tests. Thermally annealed devices last for over a week in 95°C DPBS without significant changes to the electrode impedance, which translates to a lower bound of 75 years for the half-life to failure under physiological conditions. Even non-annealed devices seem to exhibit a mean half-life of 4 years. However, while useful to compare the impact of process variations on lifetime in a relative fashion, the absolute results of such lifetime tests needs to be taken with a hand-full of salt. It is simply not possible to thermally accelerate all of the degradation processes happening in brain tissue in vivo because we do not know all of the biological and biochemical factors involved, and most of them would likely neither obey first-order kinetics nor show Arrhenius temperature dependence. Moreover, it is unclear if encapsulation that seems to work well for passive electrodes where only very small voltages are applied across the barrier layers, would be effective for the encapsulation of active electronics such as the wireless data acquisition IC developed by Muller et al. for integration with our Parylene-platinum μ ECoG with integrated thin film antenna. This is because DC-bias voltages required for the operation of semiconductor devices create electric fields that tend to concentrate near defects in the insulator, leading to further local degradation. In addition, integrated circuits are intricately sensitive to ionic contamination such that even a small, highly localised ingress of contaminants can lead to total device failure. This problem can be approached from two directions. On the one hand, ICs can be developed to use lower supply voltage and power, indeed the IC developed in the Rabaey group features a supply voltage of merely 0.5 V, too low to electrolyse water, and a total power $< 300\mu$ W. In the limit that the present voltage and current levels decrease, the active devices may be expected to behave more like passive devices in terms of lifetime and durability. On the other hand, novel multilayer structures enabled by atomic layer deposition (ALD), such as stacks of aluminum oxide and alucone [182] and related methods [181], offer better water vapor barriers than pure polymers ever could. While such stacks may never offer a truly hermetic thin-film alternative for encapsulation, they may eventually yield near-hermetic performance that will protect an active neural implant for its intended life-time of several years or, potentially, even several decades. After talking to clinicians, we also realised that other than as an interface for chronic BMI, a fully implantable wireless μ ECoG system is of little utility for the practicing surgeon unless it enables large area coverage (ideally 8 cm \times 8 cm) and also offers electrical stimulation. Thus, the road ahead holds two major engineering challenges:

- scaling up the number of recording channels (either per wireless IC: likely on-chip data compression techniques such as spatiotemporal sub-sampling [78] will be required to enable low-power operation, or through lateral combination of smaller μ ECoG modules, which would require an anti-collision communication protocol that allows several external readers to power and communicate with several wireless μ ECoGs on the cortical surface)
- Integrating stimulation capability into the wireless IC, which poses challenges of temporary charge storage and long-term electrode stability.

The wireless μ ECoG collaboration between the Maharbiz and the Rabaey labs at UC Berkeley gave birth to a startup company, Cortera Neurotechnologies, Inc. which will explore both strategies to translate the current academic prototype of our wireless μ ECoG system into a minimally invasive and fully implantable form-factor.

9.2 Interconnect limitations

We successfully fabricated electrically functional, highly compliant flex cables for high density neural probes with nanoscale features. Electrically connecting the bond pad array on the cable to the bond pad array on the probe with high yield proved very challenging. There is no commercial company that would agree to bond two such delicate devices with small bond-pad arrays to each other. Wirebonding of metal pads on Parylene C is impractical because the forces during wirebonding are strong enough to overcome metal-Parylene adhesion. We have explored several thermocompression bonding schemes using solder, conductive epoxy, anisotropic conductive film, and a mixture of doped conductive polymer PEDOT:PSS and D-sorbitol. Irrespective of bonding technique, we found handling and aligning the thin and brittle neural probes very difficult, a process that even when optimised requires an inordinate amount of manual fine-motor skill, is serial, time-consuming and overall not scalable. Based on this experience we concluded that ultra-small neural polytrodes should be monolithically integrated with flex-cables on the wafer-level. Dr. Maysamreza Chamanzar, a post-doctoral fellow in the Maharbiz lab, is currently developing a microfabrication process that allows to integrate silicon polytrodes with nanoscale trace/space features defined by Deep-UV lithography with Parylene cables on wafer level. This integrated approach offers the additional advantage that Parylene-based waveguides can be incorporated into the cable and coupled into silicon-nitride waveguides on the polytrode for targeted, patterned optical stimulation of neural tissue.

9.3 A tool for fast, nondestructive functional mapping

We have demonstrated, in collaboration with Dr. Kris Bouchard, Tom Babcock, and Leah Muller (Chang lab, UCSF) using the generation of tonotopic maps for auditory cortex in rat as a case study, that μ ECoG is a viable alternative to penetrating microelectrodes for mapping receptive fields with high spatial resolution (200 μ m). The obtained receptive fields were very similar to receptive fields derived from multi-unit activity registered with intracortical 32-channel Neuronexus laminar probes but less noisy, requiring the presentation of less copies of any given stimulus parameter set. This feature, combined with the fact that receptive fields for all electrodes can be mapped in parallel, turns the creation of detailed topographic maps of cortical function from an all day (or even multi-day) affair to a procedure that could be performed in a chronically implanted animal routinely in under 30 minutes. With such a powerful tool at our disposal, there are several interesting research avenues

to pursue in the future. While we focussed on tonotopy, there is a number of other tuned parameters to explore and compare in auditory areas such as onset-latency or monotonicity of the evoked response. Extending the channel-count and the array area by a factor of 4 (to 256 channels) will allow us to record from all of auditory cortex simultaneously and to employ methods of directed correlation such as Granger causality to study information flow between lower and higher auditory areas in realtime. More importantly, as we have already successfully established a chronic implantation protocol for these devices in our BMI experiments, we are planning to implant these devices chronically and to study on a daily basis, the learning and plasticity-related reorganization of topographic maps in experiments similar to [58].

We simultaneously acquired data using μ ECoG and laminar Neuronexus probes with the intention to build a model of how signal features as a function of cortical depth give rise to the μ ECoG signal on the surface. Incidentally, we discovered that when the same thresholding criterion that has been developed for the estimation of intracortical multi-unit firing rates with polytrodes [137] is applied to the μ ECoG signal, we register threshold crossings, the rate (MUFR) of which is stimulus-dependent and tunes akin to high-gamma power. Based on existing literature [180] it is reasonable to assume that these multi-unit signals are generated by neurons in cortical layer 2, which are $< 100 \mu\text{m}$ below the pial surface. We started the μ ECoG project with the hypothesis that the optimal resolution may be determined by the spatial extent of cortical columns ($\approx 500\mu\text{m}$), hence we built a grid that spatially oversamples this length scale. However, the presence of cortical columns is a contested phenomenon with uncertain physiological function that certainly does not universally occur everywhere in cortex [65]. Given the presence of the aforementioned superficial units and the strong functional correlation between their average firing rate and high-gamma power (the spatially best-resolved signal measured in μ ECoG), the optimal resolution for μ ECoG, at least for applications in rat neurophysiology may in fact conveniently be $200 \mu\text{m}$, because that is roughly the reported diameter of a ball of tissue that contributes to MUFR measured on a point-electrode [102]. Our μ ECoG electrodes are small ($40 \mu\text{m}$ in diameter) but they are not point-electrodes. The precise relationship between ECoG electrode size and their ability to record superficial multiunit activity remains to be investigated. Especially if smaller (and even sparser) neurons are present in cortical layer 1, μ ECoG with an electrode pitch even denser than $200 \mu\text{m}$ may be useful.

9.4 μ ECoG - the future of BMI?

We have successfully implanted our μ ECoG devices chronically in rats and showed that electrode impedance does not change dramatically over the course of a year. Given the general notion that LFPs are very similar on close-by electrodes, we were wondering if we could use a BMI paradigm to train a rat to decouple aspects of the LFP signal recorded on arbitrary pairs of different electrodes. We successfully modified a 1D-center-out-task rat BMI paradigm that uses single unit firing rate as the control signal to use γ -power instead.

Indeed, the rats learned to perform this tasks above chance for all electrode separations between $200\mu\text{m}$ and 1 mm . However, we have also observed that for some combinations of specific electrodes, the animals were not successful at decoupling high-gamma power. Unfortunately, due to hardware limitations, we were unable to open up the filters and record wideband signals and were only able to acquire data that were low-pass filtered below 200 Hz and sampled at 1 kHz . Because of that, we cannot conclude from our data whether the selective presence or absence of the aforementioned sparse superficial units could explain that effect. Preliminary data from the Carmena & Feldman labs¹ indicate that it is possible to train transgenic mice, which express GCaMP, a genetically encoded fluorescent Ca^{2+} indicator, to use the Ca^{2+} -signals produced by selected pairs of sparse neurons in layer 2/3 for BMI control. In order to determine if that same class of neurons is responsible for μECoG BMI control, we propose to use a high-density transparent μECoG , chronically implanted in a Thy1-GCaMP6 transgenic mouse, beneath a cranial window. Neural activity can simultaneously be recorded optically (2-photon) and electrically, which would render the presence of decoupleable layer 2/3 units close to the μECoG electrode directly observable. This experiment would simultaneously test our alternative hypothesis, namely that the spike-like waveforms we are observing may in fact be Ca^{2+} spikes generated in dendritic tufts of large layer 5 pyramidal cells, which reach all the way into cortical layer 1.

Translation to (non) human primates

If indeed μECoG can record multiunit activity that can control a brain-machine interface, it immediately offers all of the advantages of penetrating neural interfaces for BMI (high performance, well-developed algorithms) without any of the drawbacks (scarring of neural tissue, eventual signal loss), putting clinical application in paralyzed human patients finally within reach. We argue that μECoG no longer needs to be perceived as a compromise solution to intracortical recordings that is less-invasive but also less-precise. While we remain cautiously optimistic, for cytoarchitectonic reasons mentioned in the introduction to this thesis, it is not a priori clear that such superficial units can be recorded in human patients even if we can observe them in rodents. As a next step, two groups at UCSF and NYU, respectively, are currently adopting our μECoG technology for use in non-human primates (NHP), *macaca mulatta*. If physiologically meaningful multi-unit activity can indeed be observed on the cortical surface of NHPs, chances are good that the same would hold true in humans.

From a research point of view, it may be advantageous to explore μECoG technology in lissencephalic monkeys such as the Common Marmoset (*callithrix jacchus*). The flat cortex of these animals allows to study almost all brain areas with surface electrodes and their short generation cycle allows to develop transgenic animals (models of disease, transgenically encoded opsins or calcium indicators) [145].

¹Aaron Koralek, personal communication

9.5 Intracellular recordings with extracellular electrodes *in vivo*?

Neural recordings tend to be richer and less ambiguous whenever the neurons are close to the electrode surface. Thus, strategies are worth exploring that bring proximal neurons even closer to the electrode, to the limit of direct contact, which would in essence allow intracellular recordings from extracellular electrodes *in vivo*. Intracellular waveforms offer insights into subthreshold neural events and are less ambiguous (with respect to cell identity and signal origin) than extracellularly recorded waveforms which oftentimes appear distorted due to volume conduction. As patch-clamping multiple cells is an extremely fickle process that is limited to paired recordings from only a very few cells simultaneously, several research groups have proposed to modify electrode surfaces with conductive nanoscale structures that are functionalized with bioactive peptides that promote endocytosis. Neurons, attracted by such chemical cues, attempt to endocytose the nanostructure, which creates a $G\Omega$ seal around it that allows to record near-intracellular waveforms. The use of this technique in *in vitro* microelectrode arrays was extensively reviewed in [160]. We propose to modify our μ ECoG electrodes with nanoscale bioactive protrusions that close-by neurons will seek to actively engulf. Note that such an approach may well yield stable high-quality recordings over time because perforated μ ECoG that is chronically implanted will stay pinned in place by vascularisation through the perforations [148].

Bibliography

- [1] Neuronexus Hx64 hybrid flex-cable.
- [2] SCS Parylene Properties.
- [3] Epilepsy and the Functional Anatomy of the Human Brain. *Journal of the American Medical Association*, 155(1):86, May 1954.
- [4] Y. Agid, G. Buzsáki, D. M. Diamond, R. Frackowiak, J. Giedd, J.-A. Girault, A. Grace, J. J. Lambert, H. Manji, H. Mayberg, M. Popoli, A. Prochiantz, G. Richter-Levin, P. Somogyi, M. Spedding, P. Svenningsson, and D. Weinberger. How can drug discovery for psychiatric disorders be improved? *Nature reviews. Drug discovery*, 6(3):189–201, Mar. 2007.
- [5] C. M. Aguirre, S. Auvray, S. Pigeon, R. Izquierdo, P. Desjardins, and R. Martel. Carbon nanotube sheets as electrodes in organic light-emitting diodes. *Applied Physics Letters*, 88(18):183104, May 2006.
- [6] H. Alhaj, G. Wisniewski, and R. H. McAllister-Williams. The use of the EEG in measuring therapeutic drug action: focus on depression and antidepressants. *Journal of psychopharmacology (Oxford, England)*, 25(9):1175–91, Sept. 2011.
- [7] S. Anand, J. Muthuswamy, C. Patel, and J. Sutanto. Novel First-Level Interconnect Techniques for Flip Chip on MEMS Devices, 2012.
- [8] B. C. Auman. Fluorinated, Low Thermal Expansion Coefficient Polyimides For Inter-layer Dielectric Application: Thermal Stability, Refractive Index And High Temperature Modulus Measurements. *MRS Proceedings*, 381:19, Jan. 1995.
- [9] M. S. Baker, J. Muthuswamy, S. Anand, M. Okandan, and J. Sutanto. Electrothermal Microactuators With Peg Drive Improve Performance for Brain Implant Applications, 2012.
- [10] M. S. Berger, J. Kincaid, G. A. Ojemann, and E. Lettich. Brain mapping techniques to maximize resection, safety, and seizure control in children with brain tumors. *Neurosurgery*, 25(5):786–92, Nov. 1989.

- [11] R. Biran, D. C. Martin, and P. A. Tresco. The brain tissue response to implanted silicon microelectrode arrays is increased when the device is tethered to the skull. *Journal of biomedical materials research. Part A*, 82(1):169–78, July 2007.
- [12] T. Bjorninen, R. Muller, P. Ledochowitsch, L. Sydanheimo, L. Ukkonen, M. M. Maharbiz, and J. M. Rabaey. Design of Wireless Links to Implanted BrainMachine Interface Microelectronic Systems. *IEEE Antennas and Wireless Propagation Letters*, 11:1663–1666, 2012.
- [13] T. Bjorninen, L. Sydanheimo, L. Ukkonen, R. Muller, P. Ledochowitsch, and J. Rabaey. Antenna design for wireless electrocorticography. In *Proceedings of the 2012 IEEE International Symposium on Antennas and Propagation*, pages 1–2. IEEE, July 2012.
- [14] T. Blakely, K. J. Miller, S. P. Zanos, R. P. N. Rao, and J. G. Ojemann. Robust, long-term control of an electrocorticographic brain-computer interface with fixed parameters. *Neurosurgical focus*, 27(1):E13, July 2009.
- [15] M. Boehme and C. Charton. Properties of ITO on PET film in dependence on the coating conditions and thermal processing. *Surface and Coatings Technology*, 200(1-4):932–935, Oct. 2005.
- [16] A. S. Bondarenko and G. A. Ragoisha. EIS Spectrum Analyser.
- [17] C. A. Bosman, J.-M. Schoffelen, N. Brunet, R. Oostenveld, A. M. Bastos, T. Womelsdorf, B. Rubehn, T. Stieglitz, P. De Weerd, and P. Fries. Attentional stimulus selection through selective synchronization between monkey visual areas. *Neuron*, 75(5):875–88, Sept. 2012.
- [18] E. S. Boyden, F. Zhang, E. Bamberg, G. Nagel, and K. Deisseroth. Millisecond-timescale, genetically targeted optical control of neural activity. *Nature neuroscience*, 8(9):1263–8, Sept. 2005.
- [19] G. S. Brindley and M. D. Craggs. The electrical activity in the motor cortex that accompanies voluntary movement. *The Journal of physiology*, 223(1):28P–29P, May 1972.
- [20] D. P. Buxhoeveden. The minicolumn hypothesis in neuroscience. *Brain*, 125(5):935–951, May 2002.
- [21] G. Buzsáki. Theta oscillations in the hippocampus. *Neuron*, 33(3):325–40, Jan. 2002.
- [22] G. Buzsáki. *Rhythms of the Brain*, volume 1. 2006.
- [23] G. Buzsáki, C. A. Anastassiou, and C. Koch. The origin of extracellular fields and currents—EEG, ECoG, LFP and spikes. *Nature reviews. Neuroscience*, 13(6):407–20, June 2012.

- [24] G. Buzsaki, R. G. Bickford, G. Ponomareff, L. J. Thal, R. Mandel, and F. H. Gage. Nucleus basalis and thalamic control of neocortical activity in the freely moving rat. *The Journal of neuroscience : the official journal of the Society for Neuroscience*, 8(11):4007–26, Nov. 1988.
- [25] G. Buzsaki and B. O. Watson. Brain rhythms and neural syntax: implications for efficient coding of cognitive content and neuropsychiatric disease. *Dialogues Clin Neurosci*, 14:345–367, 2012.
- [26] J. Cang and D. a. Feldheim. Developmental mechanisms of topographic map formation and alignment. *Annual review of neuroscience*, 36:51–77, 2013.
- [27] R. T. Canolty, M. Soltani, S. S. Dalal, E. Edwards, N. F. Dronkers, S. S. Nagarajan, H. E. Kirsch, N. M. Barbaro, and R. T. Knight. Spatiotemporal dynamics of word processing in the human brain. *Front Neurosci*, 1:185–196, 2007.
- [28] J. M. Carmena, M. A. Lebedev, R. E. Crist, J. E. O’Doherty, D. M. Santucci, D. F. Dimitrov, P. G. Patil, C. S. Henriquez, and M. A. L. Nicolelis. Learning to control a brain-machine interface for reaching and grasping by primates. *PLoS biology*, 1(2):E42, Nov. 2003.
- [29] C. Chang, Y. Chen, S. Hung, and J. Chiou. A wireless and batteryless microsystem with implantable grid electrode/3-dimensional probe array for ECoG and extracellular neural recording on rat. In *2011 16th International Solid-State Sensors, Actuators and Microsystems Conference*, pages 2176–2179. IEEE, June 2011.
- [30] J. K. Chapin. Neural prosthetic devices for quadriplegia. *Current opinion in neurology*, 13(6):671–5, Dec. 2000.
- [31] C. Cheung and E. F. Chang. Real-time, time-frequency mapping of event-related cortical activation. *Journal of neural engineering*, 9(4):046018, Aug. 2012.
- [32] S. F. Cogan. Neural stimulation and recording electrodes. *Annual review of biomedical engineering*, 10:275–309, Jan. 2008.
- [33] S. F. Cogan, A. A. Guzelian, W. F. Agnew, T. G. H. Yuen, and D. B. McCreery. Over-pulsing degrades activated iridium oxide films used for intracortical neural stimulation. *Journal of neuroscience methods*, 137(2):141–50, Aug. 2004.
- [34] S. De, T. M. Higgins, P. E. Lyons, E. M. Doherty, P. N. Nirmalraj, W. J. Blau, J. J. Boland, and J. N. Coleman. Silver Nanowire Networks as Flexible, Transparent, Conducting Films: Extremely High DC to Optical Conductivity Ratios. *ACS nano*, 3(7):1767–1774, June 2009.
- [35] J. P. Donoghue. Connecting cortex to machines: recent advances in brain interfaces. *Nature neuroscience*, 5 Suppl:1085–8, Nov. 2002.

- [36] D. Donoho and I. Johnstone. Threshold selection for wavelet shrinkage of noisy data. *Proceedings of 16th Annual International Conference of the IEEE Engineering in Medicine and Biology Society*, 1994.
- [37] J. Du, T. J. Blanche, R. R. Harrison, H. A. Lester, and S. C. Masmanidis. Multiplexed, high density electrophysiology with nanofabricated neural probes. *PloS one*, 6(10):e26204, Jan. 2011.
- [38] R. Elul. The genesis of the EEG. *International review of neurobiology*, 15:227–72, July 1971.
- [39] D. S. Faber and H. Korn. Electrical field effects: their relevance in central neural networks. *Physiological reviews*, 69(3):821–63, July 1989.
- [40] A. Farajidavar, P. McCorkle, T. Wiggins, S. Rao, C. Hagains, Y. Peng, J. Seifert, M. Romero, G. O’Grady, L. Cheng, S. Sparagana, M. Delgado, S.-J. Tang, T. Abell, and J.-C. Chiao. A miniature power-efficient bidirectional telemetric platform for in-vivo acquisition of electrophysiological signals. In *2011 IEEE MTT-S International Microwave Symposium*, pages 1–4. IEEE, June 2011.
- [41] E. Fiedler, J. S. Ordonez, and T. Stieglitz. Laser-structured ceramic adapters for reliable assembly of flexible thin-film electrodes. *Biomedizinische Technik. Biomedical engineering*, Sept. 2013.
- [42] J. B. Fortin and T.-M. Lu. *Chemical Vapor Deposition Polymerization: The Growth and Properties of Parylene Thin Films(Google eBook)*. Springer, 2004.
- [43] W. Freeman. Hilbert transform for brain waves, 2007.
- [44] W. J. Freeman and J. M. Barrie. Analysis of spatial patterns of phase in neocortical gamma EEGs in rabbit. *Journal of neurophysiology*, 84(3):1266–78, Sept. 2000.
- [45] W. J. Freeman, L. J. Rogers, M. D. Holmes, and D. L. Silbergeld. Spatial spectral analysis of human electrocorticograms including the alpha and gamma bands. *Journal of Neuroscience Methods*, 95(2):111–121, Feb. 2000.
- [46] P. Fries. Modulation of Oscillatory Neuronal Synchronization by Selective Visual Attention. *Science*, 291(5508):1560–1563, Feb. 2001.
- [47] E. Fuchs and G. Flügge. Experimental animal models for the simulation of depression and anxiety. *Dialogues in clinical neuroscience*, 8(3):323–33, Jan. 2006.
- [48] C. M. Gaona, M. Sharma, Z. V. Freudenburg, J. D. Breshears, D. T. Bundy, J. Roland, D. L. Barbour, G. Schalk, and E. C. Leuthardt. Nonuniform high-gamma (60-500 Hz) power changes dissociate cognitive task and anatomy in human cortex. *The Journal of neuroscience : the official journal of the Society for Neuroscience*, 31:2091–2100, 2011.

- [49] A. P. Georgopoulos, J. T. Lurito, M. Petrides, A. B. Schwartz, and J. T. Massey. Mental rotation of the neuronal population vector. *Science (New York, N.Y.)*, 243(4888):234–236, 1989.
- [50] J. M. Gere. *Mechanics of Materials*, volume 2. 2008.
- [51] M. Ghosh. *Polyimides: Fundamentals and Applications*. Taylor & Francis, 1996.
- [52] V. Gilja, P. Nuyujukian, C. A. Chestek, J. P. Cunningham, B. M. Yu, J. M. Fan, M. M. Churchland, M. T. Kaufman, J. C. Kao, S. I. Ryu, and K. V. Shenoy. A high-performance neural prosthesis enabled by control algorithm design. *Nature neuroscience*, 15(12):1752–7, Dec. 2012.
- [53] W. K. Goodman and R. L. Alterman. Deep Brain Stimulation for Intractable Psychiatric Disorders. *Annual review of medicine*, pages 1–14, 2011.
- [54] V. Gradinaru, M. Mogri, K. R. Thompson, J. M. Henderson, and K. Deisseroth. Optical deconstruction of parkinsonian neural circuitry. *Science (New York, N.Y.)*, 324(5925):354–9, Apr. 2009.
- [55] V. Gradinaru, K. R. Thompson, F. Zhang, M. Mogri, K. Kay, M. B. Schneider, and K. Deisseroth. Targeting and readout strategies for fast optical neural control in vitro and in vivo. *The Journal of neuroscience : the official journal of the Society for Neuroscience*, 27(52):14231–8, Dec. 2007.
- [56] E. S. Greenbaum, D. D. Zhou, and SpringerLink (Online service). Implantable neural prostheses 2 techniques and engineering approaches, 2010.
- [57] K. S. Guillory, R. E. Askin, C. F. Smith, D. McDonnall, S. Hiatt, and A. M. Wilder. Wireless electrocortigraph (ECoG) recording system. In *2011 5th International IEEE/EMBS Conference on Neural Engineering*, pages 196–197. IEEE, Apr. 2011.
- [58] Y. K. Han, H. Köver, M. N. Insanally, J. H. Semerdjian, and S. Bao. Early experience impairs perceptual discrimination. *Nature neuroscience*, 10(9):1191–7, Sept. 2007.
- [59] M. Hara, K. Tsuchiya, T. Nanke, N. Mori, F. Miyake, C. Sato, and M. Murayama. Development of a new analytical method for the electrocardiogram using short-time first Fourier transforms. *Japanese circulation journal*, 63:941–944, 1999.
- [60] C. Hassler, T. Boretius, and T. Stieglitz. Polymers for neural implants. *Journal of Polymer Science Part B: Polymer Physics*, 49(1):18–33, Jan. 2011.
- [61] B. J. Hefti and P. H. Smith. Anatomy, Physiology, and Synaptic Responses of Rat Layer V Auditory Cortical Cells and Effects of Intracellular GABAA Blockade. *J Neurophysiol*, 83(5):2626–2638, May 2000.

- [62] S. Herculano-Houzel. Not all brains are made the same: new views on brain scaling in evolution. *Brain, behavior and evolution*, 78(1):22–36, Jan. 2011.
- [63] D. N. Hill, Z. Varga, H. Jia, B. Sakmann, and A. Konnerth. Multibranch activity in basal and tuft dendrites during firing of layer 5 cortical neurons in vivo. *Proceedings of the National Academy of Sciences of the United States of America*, 110(33):13618–23, Aug. 2013.
- [64] L. R. Hochberg, D. Bacher, B. Jarosiewicz, N. Y. Masse, J. D. Simeral, J. Vogel, S. Haddadin, J. Liu, S. S. Cash, P. van der Smagt, and J. P. Donoghue. Reach and grasp by people with tetraplegia using a neurally controlled robotic arm. *Nature*, 485(7398):372–5, May 2012.
- [65] J. C. Horton and D. L. Adams. The cortical column: a structure without a function. *Philosophical transactions of the Royal Society of London. Series B, Biological sciences*, 360(1456):837–62, Apr. 2005.
- [66] N. E. Huang. Introduction to the Hilbert Huang Transform. *Transform*, 5:1–26, 2005.
- [67] W. Hubbert. AFML-TR-79-4199. Technical report, University of Utah, Salt Lake City, 1980.
- [68] J. Johnson. Thermal Agitation of Electricity in Conductors. *Physical Review*, 32(1):97–109, July 1928.
- [69] J. H. Kaas. Plasticity of sensory and motor maps in adult mammals. *Annual review of neuroscience*, 14:137–167, 1991.
- [70] Y. Kajikawa and C. E. Schroeder. How local is the local field potential? *Neuron*, 72(5):847–58, Dec. 2011.
- [71] V. A. Kalatsky, D. B. Polley, M. M. Merzenich, C. E. Schreiner, and M. P. Stryker. Fine functional organization of auditory cortex revealed by Fourier optical imaging. *Proceedings of the National Academy of Sciences of the United States of America*, 102:13325–13330, 2005.
- [72] D. Khodagholy, T. Doublet, M. Gurfinkel, P. Quilichini, E. Ismailova, P. Leleux, T. Herve, S. Sanaur, C. Bernard, and G. G. Malliaras. Highly conformable conducting polymer electrodes for in vivo recordings. *Advanced materials (Deerfield Beach, Fla.)*, 23(36):H268–72, Sept. 2011.
- [73] D. Khodagholy, T. Doublet, P. Quilichini, M. Gurfinkel, P. Leleux, A. Ghestem, E. Ismailova, T. Hervé, S. Sanaur, C. Bernard, and G. G. Malliaras. In vivo recordings of brain activity using organic transistors. *Nature communications*, 4:1575, 2013.

- [74] A. Khurram and J. P. Seymour. Investigation of the photoelectrochemical effect in optoelectrodes and potential uses for implantable electrode characterization. *Conference proceedings : ... Annual International Conference of the IEEE Engineering in Medicine and Biology Society. IEEE Engineering in Medicine and Biology Society. Conference*, 2013:3032–5, July 2013.
- [75] D.-H. Kim, J. Viventi, J. J. Amsden, J. Xiao, L. Vigeland, Y.-S. Kim, J. A. Blanco, B. Panilaitis, E. S. Frechette, D. Contreras, D. L. Kaplan, F. G. Omenetto, Y. Huang, K.-C. Hwang, M. R. Zakin, B. Litt, and J. A. Rogers. Dissolvable films of silk fibroin for ultrathin conformal bio-integrated electronics. *Nature materials*, 9(6):511–7, June 2010.
- [76] J. Kim, T. J. Richner, S. Thongpang, K. A. Sillay, D. B. Niemann, A. S. Ahmed, L. A. Krugner-Higby, and J. C. Williams. Flexible thin film electrode arrays for minimally-invasive neurological monitoring. *Conference proceedings : ... Annual International Conference of the IEEE Engineering in Medicine and Biology Society. IEEE Engineering in Medicine and Biology Society. Conference*, 2009:5506–9, Jan. 2009.
- [77] J. Kim, J. A. Wilson, and J. C. Williams. A cortical recording platform utilizing microECoG electrode arrays. *Conference proceedings : ... Annual International Conference of the IEEE Engineering in Medicine and Biology Society. IEEE Engineering in Medicine and Biology Society. Conference*, 2007:5353–7, Jan. 2007.
- [78] T. Kim, N. S. Artan, J. Viventi, and H. J. Chao. Spatiotemporal compression for efficient storage and transmission of high-resolution electrocorticography data. *Conference proceedings : ... Annual International Conference of the IEEE Engineering in Medicine and Biology Society. IEEE Engineering in Medicine and Biology Society. Conference*, 2012:1012–5, Jan. 2012.
- [79] R. T. Knight and H. Eichenbaum. Multiplexed memories: a view from human cortex. *Nature neuroscience*, 16(3):257–8, Mar. 2013.
- [80] A. C. Koralek, X. Jin, J. D. Long, R. M. Costa, and J. M. Carmena. Corticostriatal plasticity is necessary for learning intentional neuroprosthetic skills. *Nature*, 483(7389):331–5, Mar. 2012.
- [81] M. Koudelka-Hep, D. C. Rodger, A. J. Fong, W. Li, H. Ameri, A. K. Ahuja, C. Gutierrez, I. Lavrov, H. Zhong, P. R. Menon, E. Meng, J. W. Burdick, R. R. Roy, V. R. Edgerton, J. D. Weiland, M. S. Humayun, and Y.-C. Tai. Flexible parylene-based multielectrode array technology for high-density neural stimulation and recording. *Sensors and Actuators B: Chemical*, 132(2):449–460, 2008.
- [82] J. Kubánek, K. J. Miller, J. G. Ojemann, J. R. Wolpaw, and G. Schalk. Decoding flexion of individual fingers using electrocorticographic signals in humans. *Journal of neural engineering*, 6(6):066001, Dec. 2009.

- [83] A. Kuruvilla and R. Flink. Intraoperative electrocorticography in epilepsy surgery: useful or not? *Seizure*, 12(8):577–584, Dec. 2003.
- [84] K. Y. Kwon, B. Sirowatka, A. Weber, and W. Li. Opto- μ ECoG Array: A Hybrid Neural Interface With Transparent μ ECoG Electrode Array and Integrated LEDs for Optogenetics. *IEEE transactions on biomedical circuits and systems*, 7(5):593–600, Oct. 2013.
- [85] S. Lakhan and E. Callaway. Deep brain stimulation for obsessive compulsive disorder and treatment resistant depression: systematic review. *PubMed Central*, 3, 2010.
- [86] M. E. Larkum, K. M. M. Kaiser, and B. Sakmann. Calcium electrogenesis in distal apical dendrites of layer 5 pyramidal cells at a critical frequency of back-propagating action potentials. *Proceedings of the National Academy of Sciences*, 96(25):14600–14604, Dec. 1999.
- [87] P. Ledochowitsch, R. J. Félus, R. R. Gibboni, A. Miyakawa, A. Bao, and M. M. Maharbiz. Fabrication and Testing of a Large Area, High Density Parylene MEMS μ ECoG Array. In *MEMS '11*, 2011.
- [88] P. Ledochowitsch, A. C. Koralek, D. Moses, J. M. Carmena, and M. M. Maharbiz. Sub-mm functional decoupling of electrocortical signals through closed-loop BMI learning. *Conference proceedings : ... Annual International Conference of the IEEE Engineering in Medicine and Biology Society. IEEE Engineering in Medicine and Biology Society. Conference*, 2013:5622–5, Jan. 2013.
- [89] P. Ledochowitsch, E. Olivero, T. Blanche, and M. M. Maharbiz. A Transparent μ ECoG Array for Simultaneous Recording and Optogenetic Stimulation. *Packaging Boston Mass*, pages 2937–2940, 2011.
- [90] P. Ledochowitsch, R. F. Tiefenauer, B. Pepin, M. M. Maharbiz, and T. J. Blanche. Nanoflex for neural nanoprobes. In *2013 Transducers & Eurosensors XXVII: The 17th International Conference on Solid-State Sensors, Actuators and Microsystems (TRANSDUCERS & EUROSENSORS XXVII)*, pages 1278–1281. IEEE, June 2013.
- [91] S. F. Lempka, M. D. Johnson, M. A. Moffitt, K. J. Otto, D. R. Kipke, and C. C. McIntyre. Theoretical analysis of intracortical microelectrode recordings. *Journal of neural engineering*, 8(4):045006, Aug. 2011.
- [92] R. P. Lesser, H. Lüders, G. Klem, D. S. Dinner, H. H. Morris, and J. Hahn. Cortical Afterdischarge and Functional Response Thresholds: Results of Extraoperative Testing. *Epilepsia*, 25(5):615–621, Oct. 1984.
- [93] E. C. Leuthardt, G. Schalk, D. Moran, and J. G. Ojemann. The emerging world of motor neuroprosthetics: a neurosurgical perspective. *Neurosurgery*, 59(1):1–14; discussion 1–14, July 2006.

- [94] E. C. Leuthardt, G. Schalk, J. R. Wolpaw, J. G. Ojemann, and D. W. Moran. A brain-computer interface using electrocorticographic signals in humans. *Journal of neural engineering*, 1(2):63–71, June 2004.
- [95] W. Li, D. Rodger, P. Menon, and Y.-C. Tai. Corrosion Behavior of Parylene-Metal-Parylene Thin Films in Saline. *ECS Transactions*, 11:1–6, 2008.
- [96] W. L. W. Li, D. Rodger, E. Meng, J. Weiland, M. Humayun, and Y.-C. T. Y.-C. Tai. Wafer-Level Parylene Packaging With Integrated RF Electronics for Wireless Retinal Prostheses. *Journal of Microelectromechanical Systems*, 19, 2010.
- [97] H. Lindén, K. H. Pettersen, and G. T. Einevoll. Intrinsic dendritic filtering gives low-pass power spectra of local field potentials. *Journal of computational neuroscience*, 29(3):423–44, Dec. 2010.
- [98] H. Lindén, T. Tetzlaff, T. C. Potjans, K. H. Pettersen, S. Grün, M. Diesmann, and G. T. Einevoll. Modeling the spatial reach of the LFP. *Neuron*, 72(5):859–72, Dec. 2011.
- [99] R. R. Llinás. The intrinsic electrophysiological properties of mammalian neurons: insights into central nervous system function. *Science (New York, N.Y.)*, 242(4886):1654–64, Dec. 1988.
- [100] S. Löffler, Y. Xie, P. Klimach, A. Richter, P. Detemple, T. Stieglitz, A. Moser, and U. G. Hofmann. Long term in vivo stability and frequency response of polyimide based flexible array probes. *Biomedizinische Technik. Biomedical engineering*, Sept. 2012.
- [101] N. K. Logothetis. What we can do and what we cannot do with fMRI. *Nature*, 453:869–878, 2008.
- [102] N. K. Logothetis, C. Kayser, and A. Oeltermann. In vivo measurement of cortical impedance spectrum in monkeys: implications for signal propagation. *Neuron*, 55(5):809–23, Sept. 2007.
- [103] E. Magiorkinis, A. Diamantis, D.-D. Mitsikostas, and G. Androustos. Headaches in antiquity and during the early scientific era. *Journal of neurology*, 256(8):1215–20, Aug. 2009.
- [104] M. Mahmud, D. Hawellek, and A. Bertoldo. EEG based brain-machine interface for navigation of robotic device. In *2010 3rd IEEE RAS & EMBS International Conference on Biomedical Robotics and Biomechatronics*, pages 168–172. IEEE, Sept. 2010.
- [105] C. Marin and E. Fernández. Biocompatibility of intracortical microelectrodes: current status and future prospects. *Frontiers in neuroengineering*, 3:8, Jan. 2010.

- [106] A. Matsumoto, B. H. Brinkmann, S. Matthew Stead, J. Matsumoto, M. T. Kucewicz, W. R. Marsh, F. Meyer, and G. Worrell. Pathological and physiological high-frequency oscillations in focal human epilepsy. *Journal of neurophysiology*, 110(8):1958–64, Oct. 2013.
- [107] D. R. Merrill, M. Bikson, and J. G. Jefferys. Electrical stimulation of excitable tissue: design of efficacious and safe protocols. *Journal of Neuroscience Methods*, 141(2):171–198, 2005.
- [108] N. Mesgarani and E. F. Chang. Selective cortical representation of attended speaker in multi-talker speech perception. *Nature*, 485:1–5, 2012.
- [109] K. J. Miller. Broadband spectral change: evidence for a macroscale correlate of population firing rate? *The Journal of neuroscience : the official journal of the Society for Neuroscience*, 30(19):6477–9, May 2010.
- [110] K. J. Miller, M. DenNijs, P. Shenoy, J. W. Miller, R. P. N. Rao, and J. G. Ojemann. Real-time functional brain mapping using electrocorticography. *NeuroImage*, 37(2):504–7, Aug. 2007.
- [111] M. Mollazadeh, E. Greenwald, N. Thakor, M. Schieber, and G. Cauwenberghs. Wireless micro-ECoG recording in primates during reach-to-grasp movements. In *2011 IEEE Biomedical Circuits and Systems Conference (BioCAS)*, pages 237–240. IEEE, Nov. 2011.
- [112] V. B. Mountcastle. The columnar organization of the neocortex. *Brain : a journal of neurology*, 120 (Pt 4:701–22, Apr. 1997.
- [113] O. Mryasov and A. Freeman. Electronic band structure of indium tin oxide and criteria for transparent conducting behavior. *Physical Review B*, 64(23):233111, Dec. 2001.
- [114] W. Mulder, J. Sluyters, T. Pajkossy, and L. Nyikos. Tafel current at fractal electrodes. *Journal of Electroanalytical Chemistry and Interfacial Electrochemistry*, 285(1):103–115, 1990.
- [115] E. J. Nestler and S. E. Hyman. Animal models of neuropsychiatric disorders. *Nature neuroscience*, 13(10):1161–9, Oct. 2010.
- [116] M. A. L. Nicolelis, D. Dimitrov, J. M. Carmena, R. Crist, G. Lehew, J. D. Kralik, and S. P. Wise. Chronic, multisite, multielectrode recordings in macaque monkeys. *Proceedings of the National Academy of Sciences of the United States of America*, 100:11041–11046, 2003.
- [117] V. Nikolenko, B. O. Watson, R. Araya, A. Woodruff, D. S. Peterka, and R. Yuste. SLM Microscopy: Scanless Two-Photon Imaging and Photostimulation with Spatial Light Modulators. *Frontiers in neural circuits*, 2:5, Jan. 2008.

- [118] M. A. Nitsche, L. G. Cohen, E. M. Wassermann, A. Priori, N. Lang, A. Antal, W. Paulus, F. Hummel, P. S. Boggio, F. Fregni, and A. Pascual-Leone. Transcranial direct current stimulation: State of the art 2008. *Brain stimulation*, 1(3):206–23, July 2008.
- [119] C. T. Nordhausen, P. J. Rousche, and R. A. Normann. A method for acute cerebral cortex recordings using the Utah Intracortical Electrode Array. *1992 14th Annual International Conference of the IEEE Engineering in Medicine and Biology Society*, 6:2390–2391, 1992.
- [120] A. Norlin. Investigation of interfacial capacitance of Pt, Ti and TiN coated electrodes by electrochemical impedance spectroscopy. *Biomolecular Engineering*, 19(2-6):67–71, Aug. 2002.
- [121] P. L. Nunez and R. Srinivasan. *Electric Fields of the Brain: The Neurophysics of EEG*, volume 4. Oxford University Press, 2006.
- [122] H. Nyquist. Thermal Agitation of Electric Charge in Conductors. *Physical Review*, 32(1):110–113, July 1928.
- [123] J. O’Doherty, M. Lebedev, T. Hanson, N. Fitzsimmons, and M. Nicolelis. A brain-machine interface instructed by direct intracortical microstimulation. *Frontiers in Integrative Neuroscience*, 3(September):1–10, 2009.
- [124] B. F. O’Donnell, W. P. Hetrick, J. L. Vohs, G. P. Krishnan, C. A. Carroll, and A. Shekhar. Neural synchronization deficits to auditory stimulation in bipolar disorder. *Neuroreport*, 15(8):1369–72, June 2004.
- [125] A. Onorato, M. A. Invernale, I. D. Berghorn, C. Pavlik, G. A. Sotzing, and M. B. Smith. Enhanced conductivity in sorbitol-treated PEDOTPSS. Observation of an in situ cyclodehydration reaction. *Synthetic Metals*, 160(21):2284–2289, 2010.
- [126] E. V. Orekhova, T. A. Stroganova, G. Nygren, M. M. Tsetlin, I. N. Posikera, C. Gillberg, and M. Elam. Excess of high frequency electroencephalogram oscillations in boys with autism. *Biological psychiatry*, 62(9):1022–9, Nov. 2007.
- [127] J. Ouyang and Y. Yang. Conducting Polymer as Transparent Electric Glue. *Advanced Materials*, 18:2141–2144, 2006.
- [128] A. Palmini. The concept of the epileptogenic zone: a modern look at Penfield and Jasper’s views on the role of interictal spikes. *Epileptic disorders : international epilepsy journal with videotape*, 8 Suppl 2:S10–5, Aug. 2006.
- [129] C. Pang, J. Cham, Z. Nenadic, S. Musallam, Y.-C. Tai, J. Burdick, and R. Andersen. A new multi-site probe array with monolithically integrated parylene flexible cable for neural prostheses. *Conference proceedings : ... Annual International Conference of the*

- IEEE Engineering in Medicine and Biology Society. IEEE Engineering in Medicine and Biology Society. Conference*, 7:7114–7117, 2005.
- [130] A. Parent and L.-N. Hazrati. Functional anatomy of the basal ganglia. I. The cortico-basal ganglia-thalamo-cortical loop. *Brain Research Reviews*, 20(1):91–127, 1995.
- [131] B. N. Pasley, S. V. David, N. Mesgarani, A. Flinker, S. A. Shamma, N. E. Crone, R. T. Knight, and E. F. Chang. Reconstructing Speech from Human Auditory Cortex. *PLoS Biology*, 10:e1001251, 2012.
- [132] J. S. Perlmutter and J. W. Mink. Deep brain stimulation. *Annual review of neuroscience*, 29:229–57, Jan. 2006.
- [133] H. Petsche, H. Pockberger, and P. Rappelsberger. On the search for the sources of the electroencephalogram. *Neuroscience*, 11(1):1–27, Jan. 1984.
- [134] F. G. Pike, R. S. Goddard, J. M. Suckling, P. Ganter, N. Kasthuri, and O. Paulsen. Distinct frequency preferences of different types of rat hippocampal neurones in response to oscillatory input currents. *The Journal of physiology*, 529 Pt 1:205–13, Nov. 2000.
- [135] D. B. Polley, H. L. Read, D. A. Storace, and M. M. Merzenich. Multiparametric auditory receptive field organization across five cortical fields in the albino rat. *Journal of neurophysiology*, 97(5):3621–38, May 2007.
- [136] D. B. Polley, E. E. Steinberg, and M. M. Merzenich. Perceptual learning directs auditory cortical map reorganization through top-down influences. *The Journal of neuroscience : the official journal of the Society for Neuroscience*, 26:4970–4982, 2006.
- [137] R. Q. Quiroga, Z. Nadasdy, and Y. Ben-Shaul. Unsupervised spike detection and sorting with wavelets and superparamagnetic clustering. *Neural computation*, 16:1661–1687, 2004.
- [138] J. E. B. Randles. Kinetics of rapid electrode reactions. *Discussions of the Faraday Society*, 1:11, Jan. 1947.
- [139] C. Rao and D. Triverdi. Chemical and electrochemical depositions of platinum group metals and their applications. *Coordination Chemistry Reviews*, 249(5-6):613–631, Mar. 2005.
- [140] A. K. Rikky Muller, Hanh-Phuc Le, Wen Li, Peter Ledochowitsch, Simone Gambini, Toni Bjorninen and J. M. R. Jose M. Carmena, Michel M. Maharbiz, Elad Alon1. A miniaturized 64-channel, 225 μ W wireless electrocorticographic neural sensor. In *International Solid-State Circuits Conference*, page accepted for presentation, San Francisco, 2014.

- [141] L. S. Robblee, J. McHardy, W. F. Agnew, and L. A. Bullara. Electrical stimulation with Pt electrodes. VII. Dissolution of Pt electrodes during electrical stimulation of the cat cerebral cortex. *Journal of neuroscience methods*, 9(4):301–8, Dec. 1983.
- [142] A. G. Rouse, J. J. Williams, J. J. Wheeler, and D. W. Moran. Cortical adaptation to a chronic micro-electrocorticographic brain computer interface. *The Journal of neuroscience : the official journal of the Society for Neuroscience*, 33(4):1326–30, Jan. 2013.
- [143] B. Rubehn, C. Bosman, R. Oostenveld, P. Fries, and T. Stieglitz. A MEMS-based flexible multichannel ECoG-electrode array. *Journal of neural engineering*, 6(3):036003, June 2009.
- [144] O. Ruiz, B. R. Lustig, J. J. Nassi, A. Cetin, J. H. Reynolds, T. D. Albright, E. M. Callaway, G. R. Stoner, and A. W. Roe. Optogenetics through windows on the brain in the nonhuman primate. *Journal of neurophysiology*, 110(6):1455–67, Sept. 2013.
- [145] E. Sasaki, H. Suemizu, A. Shimada, K. Hanazawa, R. Oiwa, M. Kamioka, I. Tomioka, Y. Sotomaru, R. Hirakawa, T. Eto, S. Shiozawa, T. Maeda, M. Ito, R. Ito, C. Kito, C. Yagihashi, K. Kawai, H. Miyoshi, Y. Tanioka, N. Tamaoki, S. Habu, H. Okano, and T. Nomura. Generation of transgenic non-human primates with germline transmission. *Nature*, 459(7246):523–7, May 2009.
- [146] G. Schalk. Can ElectroCorticography (ECoG) Support Robust and Powerful Brain-Computer Interfaces? *Frontiers in neuroengineering*, 3:9, Jan. 2010.
- [147] G. Schalk and E. C. Leuthardt. Brain-computer interfaces using electrocorticographic signals. *IEEE reviews in biomedical engineering*, 4:140–54, Jan. 2011.
- [148] A. A. Schendel, S. Thongpang, S. K. Brodnick, T. J. Richner, B. D. B. Lindevig, L. Krugner-Higby, and J. C. Williams. A cranial window imaging method for monitoring vascular growth around chronically implanted micro-ECoG devices. *Journal of neuroscience methods*, 218(1):121–30, Aug. 2013.
- [149] T. E. Schläpfer and B. H. Bewernick. Deep brain stimulation for psychiatric disorders - state of the art. *Advances and technical standards in neurosurgery*, 34:37–57, 2009.
- [150] C. Schörkhuber and A. Klapuri. Constant-Q Transform Toolbox for Music Processing. In *Proc. of the 7th Sound and Music Computing Conference*, pages 56–64, 2010.
- [151] C. E. Schreiner and J. A. Winer. Auditory cortex mapmaking: principles, projections, and plasticity. *Neuron*, 56:356–365, 2007.
- [152] M. Schuettler, S. Schroer, J. S. Ordonez, and T. Stieglitz. Laser-fabrication of peripheral nerve cuff electrodes with integrated microfluidic channels. In *2011 5th International IEEE/EMBS Conference on Neural Engineering*, pages 245–248. IEEE, Apr. 2011.

- [153] A. B. Schwartz, X. T. Cui, D. J. Weber, and D. W. Moran. Brain-controlled interfaces: movement restoration with neural prosthetics. *Neuron*, 52(1):205–20, Oct. 2006.
- [154] J. Selvakumaran, M. Hughes, D. Ewins, and P. Richards. Biocompatibility studies of materials used for chronically implantable microelectrodes. In *1st Annual International IEEE-EMBS Special Topic Conference on Microtechnologies in Medicine and Biology. Proceedings (Cat. No.00EX451)*, pages 521–525. IEEE, 2002.
- [155] D. Seo, J. M. Carmena, J. M. Rabaey, E. Alon, and M. M. Maharbiz. Neural Dust: An Ultrasonic, Low Power Solution for Chronic Brain-Machine Interfaces. July 2013.
- [156] M. D. Serruya, N. G. Hatsopoulos, L. Paninski, M. R. Fellows, and J. P. Donoghue. Instant neural control of a movement signal. *Nature*, 416(6877):141–2, Mar. 2002.
- [157] S. Shamma-Donoghue, R. White, N. Cotter, F. Simmons, and G. May. Thin-film multielectrode arrays for a cochlear prosthesis, 1982.
- [158] P. Simen, T. Polk, R. Lewis, and E. Freedman. Universal computation by networks of model cortical columns. In *Proceedings of the International Joint Conference on Neural Networks, 2003.*, volume 1, pages 230–235. IEEE.
- [159] M. W. Slutzky, L. R. Jordan, T. Krieg, M. Chen, D. J. Mogul, and L. E. Miller. Optimal spacing of surface electrode arrays for brain-machine interface applications. *Journal of neural engineering*, 7(2):26004, Apr. 2010.
- [160] M. E. Spira and A. Hai. Multi-electrode array technologies for neuroscience and cardiology. *Nature nanotechnology*, 8(2):83–94, Feb. 2013.
- [161] W. C. Stacey, S. Kellis, B. Greger, C. R. Butson, P. R. Patel, T. Assaf, T. Mihaylova, and S. Glynn. Potential for unreliable interpretation of EEG recorded with microelectrodes. *Epilepsia*, 54(8):1391–401, Aug. 2013.
- [162] J. L. Stone and J. R. Hughes. Early history of electroencephalography and establishment of the American Clinical Neurophysiology Society. *Journal of clinical neurophysiology : official publication of the American Electroencephalographic Society*, 30:28–44, 2013.
- [163] D. M. Taylor, S. I. H. Tillery, and A. B. Schwartz. Direct cortical control of 3D neuroprosthetic devices. *Science (New York, N.Y.)*, 296(5574):1829–32, June 2002.
- [164] S. Thongpang, T. J. Richner, S. K. Brodnick, A. Schendel, J. Kim, J. A. Wilson, J. Hippensteel, L. Krugner-Higby, D. Moran, A. S. Ahmed, D. Neimann, K. Sillay, and J. C. Williams. A micro-electrocorticography platform and deployment strategies for chronic BCI applications. *Clinical EEG and neuroscience : official journal of the EEG and Clinical Neuroscience Society (ENCS)*, 42(4):259–65, Oct. 2011.

- [165] E. Tolstosheeva, J. Hoeffmann, J. Pistor, D. Rotermund, T. Schellenberg, D. Boll, T. Hertzberg, V. Gordillo-Gonzalez, S. Mandon, D. Peters-Drolshagen, M. Schneider, K. Pawelzik, A. Kreiter, S. Paul, and W. Lang. Towards a wireless and fully-implantable ECoG system. In *2013 Transducers & Euroensors XXVII: The 17th International Conference on Solid-State Sensors, Actuators and Microsystems (TRANSDUCERS & EUROSENSORS XXVII)*, pages 384–387. IEEE, June 2013.
- [166] Z. Tovar-Spinoza, D. Carter, D. Ferrone, Y. Eksioglu, and S. Huckins. The use of MRI-guided laser-induced thermal ablation for epilepsy. *Child's nervous system : ChNS : official journal of the International Society for Pediatric Neurosurgery*, 29(11):2089–94, Nov. 2013.
- [167] R. Traeger. Nonhermeticity of Polymeric Lid Sealants. *IEEE Transactions on Parts, Hybrids, and Packaging*, 13(2):147–152, June 1977.
- [168] O. Tuna, Y. Selamet, G. Aygun, and L. Ozyuzer. High quality ITO thin films grown by dc and RF sputtering without oxygen. *Journal of Physics D: Applied Physics*, 43(5):055402, Feb. 2010.
- [169] S. B. Udin and J. W. Fawcett. Formation of topographic maps. *Annual review of neuroscience*, 11:289–327, 1988.
- [170] P. J. Uhlhaas and W. Singer. Abnormal neural oscillations and synchrony in schizophrenia. *Nature reviews. Neuroscience*, 11(2):100–13, Feb. 2010.
- [171] M. Unser. Wavelets, statistics, and biomedical applications. *Proceedings of 8th Workshop on Statistical Signal and Array Processing*, 1996.
- [172] L. Ventura-Antunes, B. Mota, and S. Herculano-Houzel. Different scaling of white matter volume, cortical connectivity, and gyrification across rodent and primate brains. *Frontiers in neuroanatomy*, 7:3, Jan. 2013.
- [173] B. Vickrey, R. Rausch, J. Engel, C. Ary, B. Visscher, R. Hays, R. Brook, and W. Rogers. Outcomes in 248 patients who had diagnostic evaluations for epilepsy surgery. *The Lancet*, 346(8988):1445–1449, Dec. 1995.
- [174] J. Viventi, D.-H. Kim, L. Vigeland, E. S. Frechette, J. A. Blanco, Y.-S. Kim, A. E. Avrin, V. R. Tiruvadi, S.-W. Hwang, A. C. Vanleer, D. F. Wulsin, K. Davis, C. E. Gelber, L. Palmer, J. Van der Spiegel, J. Wu, J. Xiao, Y. Huang, D. Contreras, J. A. Rogers, and B. Litt. Flexible, foldable, actively multiplexed, high-density electrode array for mapping brain activity in vivo. *Nature neuroscience*, 14(12):1599–605, Dec. 2011.
- [175] P. N. Wahjudi, J. H. Oh, S. O. Salman, J. A. Seabold, D. C. Rodger, Y.-C. Tai, and M. E. Thompson. Improvement of metal and tissue adhesion on surface-modified parylene C. *Journal of biomedical materials research. Part A*, 89(1):206–14, Apr. 2009.

- [176] B. A. Wandell and S. M. Smirnakis. Plasticity and stability of visual field maps in adult primary visual cortex. *Nature reviews. Neuroscience*, 10:873–884, 2009.
- [177] X. Wang, L. Zhi, and K. Müllen. Transparent, conductive graphene electrodes for dye-sensitized solar cells. *Nano letters*, 8(1):323–7, Jan. 2008.
- [178] C. P. Warren, S. Hu, M. Stead, B. H. Brinkmann, M. R. Bower, and G. A. Worrell. Synchrony in normal and focal epileptic brain: the seizure onset zone is functionally disconnected. *Journal of neurophysiology*, 104(6):3530–9, Dec. 2010.
- [179] S. Watkins, D. Gandhi, and P. J. Rousche. Biocompatibility of polyimide-based neural interfaces for chronic implant applications. *Journal of Undergraduate Research*, 36, 2007.
- [180] M. Weliky, J. Fiser, R. H. Hunt, and D. N. Wagner. Coding of Natural Scenes in Primary Visual Cortex. *Neuron*, 37(4):703–718, 2003.
- [181] X. Xie, L. Rieth, S. Merugu, P. Tathireddy, and F. Solzbacher. Plasma-assisted atomic layer deposition of Al(2)O(3) and parylene C bi-layer encapsulation for chronic implantable electronics. *Applied physics letters*, 101(9):93702, Aug. 2012.
- [182] B. Yoon, D. Seghete, A. S. Cavanagh, and S. M. George. Molecular Layer Deposition of Hybrid Organic-Inorganic Alucone Polymer Films Using a Three-Step ABC Reaction Sequence. Nov. 2009.
- [183] J. Yordanova, T. Banaschewski, V. Kolev, W. Woerner, and A. Rothenberger. Abnormal early stages of task stimulus processing in children with attention-deficit hyperactivity disorder—evidence from event-related gamma oscillations. *Clinical neurophysiology : official journal of the International Federation of Clinical Neurophysiology*, 112(6):1096–108, June 2001.
- [184] W. C. Young and R. G. Budynas. *Roark's Formulas for Stress and Strain*, volume 7. McGraw-Hill, 2002.
- [185] T. P. Zanos, P. J. Mineault, and C. C. Pack. Removal of spurious correlations between spikes and local field potentials. *Journal of neurophysiology*, 105(1):474–86, Jan. 2011.